2018

Improving hydrothermal stability of carbon-supported metal catalysts for biomass conversions

Jiajie Huo
Iowa State University

Improving hydrothermal stability of carbon-supported metal catalysts for biomass conversions

by

Jiajie Huo

A dissertation submitted to the graduate faculty

in partial fulfillment of the requirements for the degree of

DOCTOR OF PHILOSOPHY

Major: Chemical Engineering

Program of Study Committee:
Brent H. Shanks, Major Professor
Jean-Philippe Tessonnier
Wenzhen Li
Wenyu Huang
Aaron D. Sadow

The student author, whose presentation of the scholarship herein was approved by the program of study committee, is solely responsible for the content of this dissertation. The Graduate College will ensure this dissertation is globally accessible and will not permit alterations after a degree is conferred.

Iowa State University

Ames, Iowa

2018

TABLE OF CONTENTS

ACKNOWLEDGEMENTS

Conducting research and getting a Ph.D degree takes a lot of efforts, including mine and many others that are involved in my study and life. Here I want to give my appreciation to all that have helped me in this hard but rewarding process.

I would like to thank my major professor- Prof. Brent Shanks first. The research would not be possible without his guidance and mentoring. I especially appreciate his encouragement to not only think about the research details, but also the big picture in the overall chemical engineering field. His curiosity towards research, even outside his research field always inspired me to keep curious and being amazed by research. He also gave me the freedom to pursue the research I am interested with sufficient guidance. I also thank him for his help in my career development.

I also thank my committee members for their evaluation, helpful discussions and suggestions in my research. The “floor meeting” we had with the group of Prof. Shanks, Prof. Tessonnier, Prof. Li and Prof. Roling always gave me new insights and knowledge from other perspective. I would like to thank Prof. Tessonnier, Prof. Li and Prof. Roling for their helpful discussions and advices. I also thank Prof. Tessonnier and Prof. Li for the fruitful collaboration during my PhD study. It has been a wonderful experience to step outside my own research area and get involved in different projects. It broadens my knowledge and horizon.

The research would not be possible without the collaborations from other research groups in the Center for Biorenewable Chemicals (CBIRC). The precious input from solid state NMR characterization on carbon material from Pu Duan and Prof. Klaus Schmidt-Rohr, and the Scanning Transmission Electron Microscopy (STEM) analysis from Dr. Hien N. Pham and Prof. Abhaya K. Datye makes my research complete. I also enjoyed the discussion and interaction

with Prof. Robert Davis, Prof. James Duemesic, and Prof. Matthew Neurok during the CBIRC meetings. It helped me get into catalysis field quickly. Deyny Mendivelso-Perez and Prof. Emily A. Smith helped with Raman analysis in the second chapter. Dr. Yuan Xue and Dr. Patrick Johnston helped with elemental analysis and ICP-OES. Russell Mahmood, Zhiqi Yao, and Prof. Andrew Hillier helped with ATR-FTIR analysis.

The folks on BRL 2nd floor are also acknowledged. I enjoyed the work with Dr. Jason Anderson, Dr. Tianfu Wang, Dr. Jing Zhang, Dr. Michael Nolte, Dr. Adam Okerlund, Dr. Jack Carraher, Dr. Robert Johnson, Dr. Toni Pfennig, Dr. Thomas Hoff, Dr. John Matthession, Dr. Ji Qi, Dr. David Chadderdon, Dr. Xiaotong Chadderdon, Dr. Yang Qiu, Dr. Neeva Benipal, Yan Cheng, Dr. Radhika Rao, and Sanaz Abdolmohammadi. I am also thankful for the undergraduates who participated in my research-Evie Goh, Wenjiao Chen, Yee Jher Chan, and Zhanyi Yao.

I would like to thank my family as well. My parents Zhiyong Huo and Zhengyan Wu provided a comfortable environment for me to grow up. I especially thank my mother for her continuous encouragement and support to excel in school work and research. Thank my sister Jiamin Huo for taking care of my mother during my absence of the last five years. My wife-Fang Fang fed me during the long hours of continuous flow reactions, gave me rides to lab, encouraged me when experiments were not going well. Meeting her and marrying her is the sweetest moment in the last 5 years.

Thank my friends in Chemical and Biological Engineering Department and Ames. Thank my friends in both China and United States. I will always remember the early mornings and late evenings in the lab during the stability test in continuous flow reactions, this is my favourite memory in my PhD study.

ABSTRACT

Human civilization and modern development relies on energy, fuels, and chemicals. Since the mid-late 1700s fossil carbons have been the major source of our energy and chemicals. This continues to pose environmental concerns such as greenhouse gas emission and concerns about its unsustainable nature. As a result, developing alternative clean and renewable energy and chemicals is one of the most urgent challenges facing humanity. Biomass have demonstrated the potential to be upgraded to fuels and chemicals with several challenges to be addressed. Hydrothermal stability of catalyst is one of the challenges as many biomass conversion reactions are happening in aqueous phase.

In the first chapter, general concerns about fossil fuels were discussed, followed by an overview of biomass conversion to both fuels and chemicals. The challenges facing biomass conversion were discussed including hydrothermal stability of the catalyst. Hydrothermal stability of common catalyst supports was summarized and compared. We also demonstrated different deactivation mechanisms of catalyst during hydrothermal conditions. Several strategies to improve the hydrothermal stability of catalyst were also raised.

In the second chapter, we used the different pyrolysis temperature to tune the surface chemistry of the carbon coated SBA-15 support. Hydrothermal treatments and reactions were performed on the supported Pd catalyst to investigate the hydrothermal stability of the Pd particles. Through detailed ^{13}C NMR, carbon surface chemistry was analyzed and compared in a systematic way. A better Pd stability was found on low-temperature synthesized carbon supports with more oxygen-functional groups. Leaching and sintering was the main reason for deactivation of the catalyst.

In the third chapter, a nitrogen-doped carbon coated SBA-15 supported Pd material was synthesized. The catalyst showed improved stability than the only carbon coated SBA-15 supported Pd catalyst with reduced sintering and leaching. ^{15}N and ^{13}C NMR revealed the nitrogen, oxygen and carbon surface chemistry of the catalyst. The mesoporous structure of SBA-15 was found collapsed during the hydrothermal treatment and reactions without diminishing the stability and activity of Pd particles. Further nitrogen-doped carbon coating on CMK-3 support showed the potential application to other materials. The improved stability of Pd nanoparticles on Pd 300NC materials was ascribed to the synergistic effect of oxygen and nitrogen heteroatoms as well as decorative carbon overlayer on Pd nanoparticles.

In the fourth chapter, carbon deposition and sintering was found to be a major deactivation mechanism on the carbon supported Pt catalyst. A new PANI XC72R was found to be able to stabilize Pt particles with minimum sintering. Besides, a simple regeneration method including low temperature air oxidation and H_2 reduction was effective to fully recover the catalytic activity without affecting the carbon support over long time on stream. The regeneration helped to remove the carbon deposits on the catalyst and redisperse Pt particles. The same regeneration method was found effective on Ru catalysts.

Future directions will be focused on further improving the hydrothermal stability of the catalyst including fundamental understanding the deactivation mechanisms and developing novel stable catalyst materials.

CHAPTER 1. INTRODUCTION

1.1 Concerns about Fossil Carbon

Beginning in the mid-18th century, the accelerated human civilization and modernization relies heavily on fossil carbons such as coal, petroleum, and natural gas. These three fossil carbons have remained as main sources for energy, fuels, and chemicals since 19th century until today. Fossil carbons have been used extensively to generate heat, electricity, and provide mechanical energy. The fuel and chemical products based on fossil carbons range from transportation fuels, special chemicals and commodity chemicals.

There are several problems regarding fossil carbons. First, they are not renewable and there are some arguments that they will not be accessible by certain year with continued use. Second, the emission of CO_2 from burning of fossil fuels is causing serious environmental problems including global warming, acidification of ocean, rising sea level, acid rain, and pollution. As the energy consumption continues to grow with increasing population worldwide, it is urgent to develop and utilize alternative ways for energy, fuels, and chemicals.

While improving the utilization efficiency of fossil carbon is an approach to reduce their use, developing alternative renewable energy, fuels, and chemicals are also crucial. Though renewable energy can be obtained from several forms including solar energy, wind energy, hydroelectrical, bio-oil, and geothermal energy, renewable chemicals and fuels may only be extracted from biomass. As a result, a lot of attention from both academia and industry is paid to biomass conversions for fuels or chemicals.

1.2 Biomass Overview

Biomass is defined as “organic materials of recent biological origin”.[1] According to the estimation of US Department of Agriculture and Oak Ridge National Laboratory, an annual amount of 1.3×10^9 metric tons of dry biomass can be produced sustainably.[2]

Biomass includes corn stover, blighted trees, and algae. Depending on different source, biomass are usually comprised of lignocellucose, starch, triglycerides. Lignocellucose is the most abundant source of carbon on earth and contains cellulose (40%), hemicellulose (25%), and lignin (20%). Cellulose and hemicellulose can be broken down to glucose or fructose via hydrolysis, while lignin structure is more rigid and complex. Animal fat, vegetable oil, and algae are mainly composed of triglyceride, which can be upgraded to bio diesel. As some biomass are edible as food, it seems more reasonable to focus on non-edible biomass conversion for fuels or chemicals.

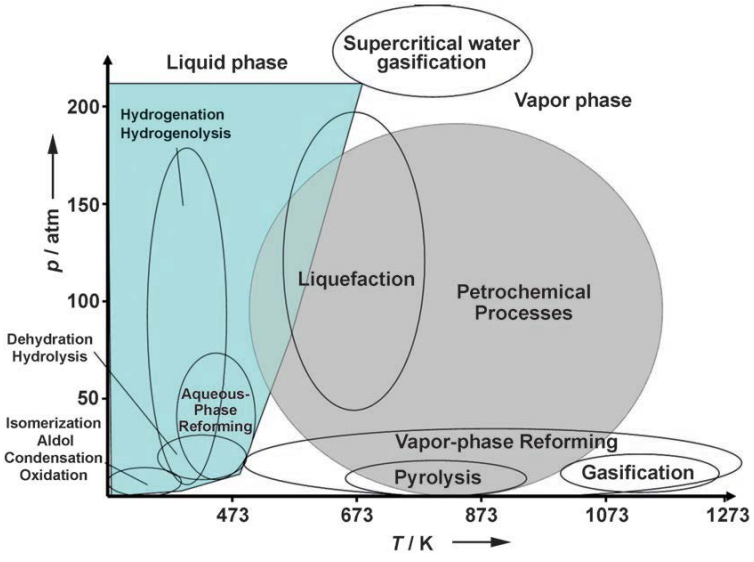

Figure 1.1 Comparison of approximate reaction conditions for biomass conversion and petroleum process. Reproduced with permission from [3]

Biomass contains a lot of oxygen functional groups, which requires deoxygenation in the process. Several reviews are available regarding the conversion of biomass to fuels or chemicals.[3-6] Catalyst is crucial in biomass conversion to speed up reaction. While molecular catalysts (metal complexes) and enzymes selectively catalyze biomass conversions, heterogeneous catalyst still remains to be an indispensable way to convert biomass due to easy separation of catalyst.[7] Besides, catalytic biomass conversion reactions also occur in condensed phase at a relatively lower temperature compared with petroleum processes (Figure 1.1).

1.2.1. Biomass to Fuel

Heat and electricity can be produced from biomass. However, as the only alternative for petroleum fuels, biomass conversion is mainly used to produce fuels and chemicals.[1,8] Fuels from biomass are considered as carbon neutral since the CO_2 emitted from biomass is the same amount converted by the biomass itself. Different routes of biofuel production are demonstrated in Figure 1.2 Overall, lignocellulose were mainly upgraded to biofuel by gasification, liquefaction, fast pyrolysis, pretreatment and hydrolysis.[6] Through pretreatment and hydrolysis, sugar monomer was obtained. From sugar, ethanol was produced by fermentation. Dumesic et al. also developed aqueous phase catalytic process to transform sugar to hydrogen and alkanes.[6,9] Triglycerides and terpenes routes were also described.[6] Triglycerides from vegetable oil and animal fat is used to produce biodiesel through transesterification catalysed by acid or base. Levulinic acid, furan derivatives, polyols, and fatty acids were the platform molecules most used in biofuels and fuel additives.[8] Gasification, pyrolysis and hydrolysis were still the main methods to produce fuels and chemicals from biomass.[6,8] For some fuel applications, biomass conversion to fuels doesn't require complete oxygen removal as the oxygenated compound can improve anti-knocking properties.[7] It is worth noting that the efficiency of biomass to fuel is usually low,

with a portion of energy lost during the process. Besides, competing with petroleum based fuels, the process of biomass conversion to fuels have to be economically cheaper or comparable with petroleum process. Coke formation, poor selectivity and stability are usually the challenges as well. More research needs to be done to make the technology more feasible and efficient.

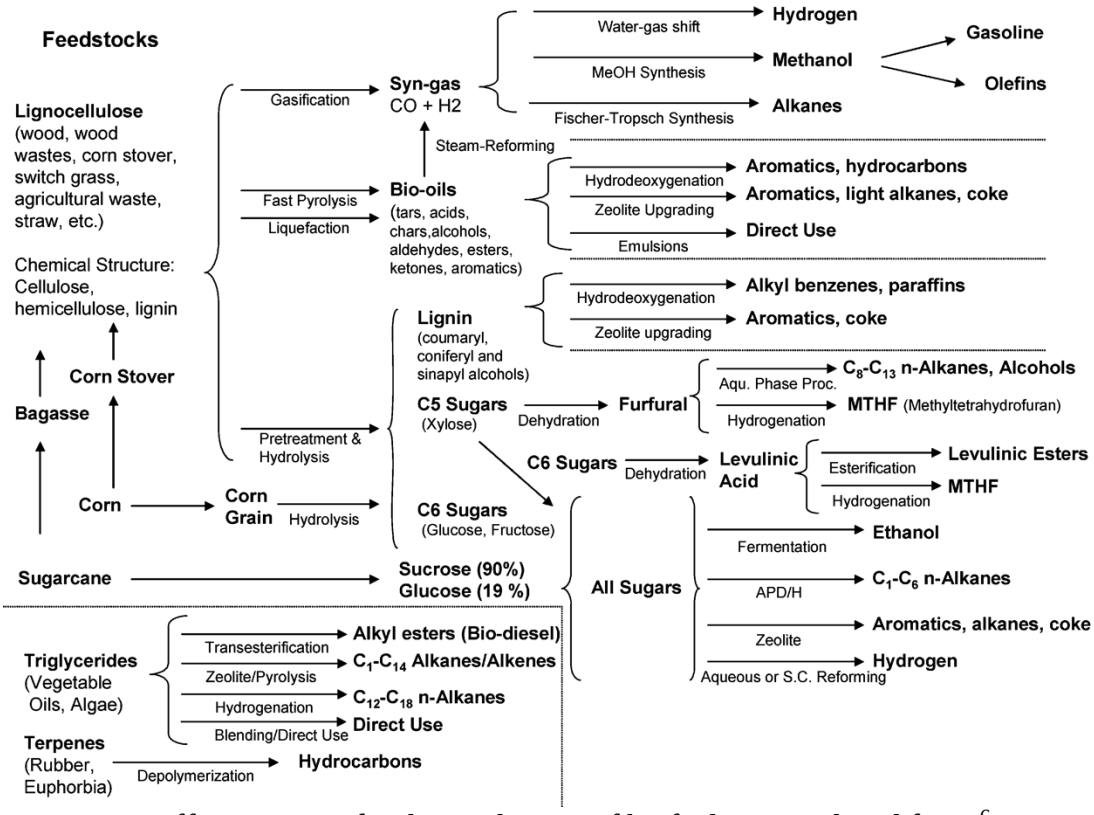

Figure 1.2 Different routes for the production of biofuels. Reproduced from [6]

1.2.2. Biomass to Chemicals

In petroleum industry, only 3.4% of the oil barrel was used to produce chemical, though the value produced is comparable to the value of fuels produced from 70.6% of the oil barrel.[10] In this light, producing high-value chemicals out of biomass is more attractive. Conversion to chemicals usually starts with carbohydrates via hydrolysis, isomerization, dehydration, reforming reactions, aldol condensation, hydrogenation, selective oxidation, and hydrogenolysis.[3,11]

In 2016, 12 platform chemicals for research and application in biomass conversion was demonstrated by USDOE with near-term potential including butadiene, butanediol, ethyl lactate, fatty alcohols, furfural, glycerol, isoprene, lactic acid, propanediol, propylene glycol, succinic acid, and xylene.[12] These chemicals were considered to have the potential to scale up from lab to market in a near future. From these chemicals, higher-value chemicals can be produced such as green solvents, and biopolymers.[12] The biomass-derived chemicals may have identical or even superior properties than the petroleum-based chemicals.

While the platform chemicals have been produced successfully from biomass, it may still be hard to compete with the cost-effective petroleum process. Conversions to biopolymers in a few steps had been developed, eliminating the separation and purification process.[13] These biopolymers were used to produce paper additives, paints, resins, foams, surfactants, lubricants, and plasticisers.[13] It is worth noting to carefully examine the green character of biomass conversion as the renewable feedstock doesn't necessarily guarantee green chemistry.[13,14] The integration of biomass-derived chemical and biofuels would further improve energy efficiency and resource utilization.[15]

1.3 Challenges Facing Biomass Conversion

While biomass offers an alternative way to produce fuels and chemicals, there are several challenges regarding biomass conversions. First, biomass contains a lot of oxygen functional groups and determining how to selectively remove the oxygen is crucial. To address this problem, the Center for Biorenewable Chemicals (CBiRC) developed the strategy to combine biocatalysis and chemical catalysis to transform biomass to chemicals.[16-18] Not only are some already-existing chemicals produced in a more sustainable and cleaner way, new chemical molecules can also be generated through this approach.[19] Besides, CBiRC focuses on identifying

and developing the platform chemicals, which has a much broader impact and applications than specific compounds.[19] Within the heterogeneous catalysis field, many efforts have been applied to improve the selectivity to remove oxygen including developing new catalysts and reactor optimizing the processes. Bimetallic catalysts have been used to improve the activity and selectivity for biomass conversion.[20,21] For example, Dumesic et al. studied the improved activity for aqueous phase reactions (APR) when Pt or Pd is alloyed with Ni, Co, or Fe.[22] Pd on Fe_2O_3 showed the highest activity. Huber et al. also observed increased performance for aqueous-phase hydrodeoxygenation with bimetallic catalyst.[23]

Second, as biomass conversion including the hydrolysis of cellulose, hemicellulose and lignin, and the later reactions of derived sugar to other chemicals are usually happening in aqueous phase at various temperature and pressure, it requires the catalyst to be hydrothermally stable.[16,24,25] First of all, when removing oxygen from biomass, water is usually formed as a product, which remains in the reactor. Besides, water offers a cheap and green solvent for biomass conversion process, but it also requires high stability on the catalyst.[26,27] This is in contrast with petroleum process, where usually only thermal stability is consider as little water is involved in the feedstock and process. Common metal oxides like alumina and silica, which are widely used in petroleum process, will undergo structural change and thus lose the structural integrity and surface area under these harsh conditions. As a result, the search and fundamental understanding of hydrothermally-stable catalyst is another challenge to be solved.

Third, catalyst has to withstand biogenic impurities from the fermentation media since biomass is usually first processed by fermentation to selectively remove oxygen and then handed to catalytic reaction.[16,28] While purification of fermentation media helps to alleviate catalyst poisoning, this process is expensive and energy intensive. There have already been some

strategies to improve the stability of catalyst against impurities without purification. Schwartz et al. used polyvinyl alcohol (PVA) coating on alumina supported PdAu bimetallic catalysts to suppress the deactivation of catalyst caused by methionine binding to Pd particles.[29] Tessonnier et al. combined electrocatalysis and metabolic engineering to deal with biogenic impurities.[30] High yield (94%) to 3-hexenedioic acid was obtained from muconic acid in the fermentation broth without purification.[30]

Fourth, as biomass conversion usually happening in liquid phase, opposed to gas phase reactions in petroleum, fundamental understanding about the interaction of reactants in solvent and solid catalyst is still lacking.[25] Unlike well-developed spectroscopic investigation for gas phase reactions, the in-situ characterization for solid-liquid reaction is hindered by the fact that the reactant molecules and solvent molecules are mixed together, thus blurring the signal of reactant in in-situ study.[25,31,32] Besides, the high functionality of biomass molecules also makes it difficult to study the reactant-catalyst interaction. New insights and techniques in both experiment and computation need to be developed to better investigate the catalyst interaction with reactant in liquid solvent.

1.4 Hydrothermal Stability of Common Catalyst Supports

While the hydrothermal conditions include superheated steam conditions, the majority of biomass conversion is happening at a temperature lower than 250 °C in aqueous phase.[33] In our research, we focus on the hydrothermal condition below 250 °C. Different reactions like hydrolysis, dehydration, isomerization, oxidation, hydrogenation, and aldol condensation occur at this hydrothermal condition. We will discuss hydrothermal stability of some common catalyst supports below first.

Metal oxide, is usually considered a good catalyst support with a high surface area, good structural integrity and mechanical strength. Widely applied in many petroleum process, zeolite, alumina, silica, zirconia, and titania have been investigated extensively, especially for gas-phase reactions. While showing a good stability for gas-phase reactions, most of these metal oxides are not stable under hydrothermal conditions because water at high temperature are more reactive and can easily hydrolyze the chemical bond or break the structure. It is worth noting that some mixed metal oxide are stable under hydrothermal conditions.[34,35] Discussed below are some common metal oxides including zeolite, silica, alumina, zirconia, and titania.

Zeolite is one of the most used catalyst in petroleum industry. It has shown good catalytic activity in the isomerization of glucose to fructose.[36,37] However, Sn was found leaching from Sn-Beta with a damaged framework under hydrothermal conditions at 100 °C for glucose isomerization.[38] Sievers et al. found that zeolite Y degraded to an amorphous material with Si/Al ratio of 14 or higher while ZSM-5 was stable in liquid water at 150°C and 200°C.[39] However, Tessonnier et al. investigated the leached Al and Si from ZSM-5 into the hydrothermal treatment solution and found that inorganic salt facilitate the hydrolysis of Si-O-Al and thus increase the leaching of Al^{3+} species.[40] The XRD of the treated ZSM-5 still showed crystalline structure.

Silica including amorphous silica and ordered mesoporous silica like MCM-41 and SBA-15 are not stable under hydrothermal conditions. MCM-41 and MCM-48 lost structural integrity in boiling water for 12 hours.[41] Mesoporous structure also disappeared in SBA-15 after hydrothermal treatment in water at 200 °C for 12 hours with a loss of more than 95% surface area.[42] Silica gel was also found to lose surface area from 280 m^2/g to 70 m^2/g after the same hydrothermal treatment.[42] The structural loss is caused by hydrolysis of Si-O-Si linkages.[41] Pollock et al. found that hydrolysis of siloxane bonds was not as significant in vapor water as in

liquid water at the same temperature.[43] Silica was found to dissolve from near the entrance of secondary pores and redeposit into the deeper pores.

Alumina, another widely used catalyst support, is not hydrothermally stable either. Structure of γ-Alumina was found to change to boehmite after 10 hours in water at 200°C as verified by X-ray diffraction.[42,44] Both surface area and Lewis acid sites concentration decreased after hydrothermal treatment as a result of phase change.

Titania and zirconia have better stability under hydrothermal conditions compared with other metal supports. TiO_2 and ZrO_2 found application in catalytic wet air oxidation reactions to treat wastewater streams.[45] No phase change was found on TiO_2 after 100h of hydrothermal reaction at 190 °C verified by XRD.[46] However, Huber et al found that TiO_2 was stable only with surface area less than 52 m^2/g, while ZrO_2 was not stable as accompanied with decreasing surface area and increasing crystallite size during hydrothermal treatment.[47]

Carbon is another material regarded as hydrothermally stable. As carbon material can be burnt away, it makes the recovery and recycling process of the metal much easier. Carbon materials including activated carbon, carbon black and graphite have been used a lot as support for precious metal catalysts in industry.[48] The hydrophobicity of carbon materials makes it stable under hydrothermal conditions. Sievers et al studied the hydrothermal stability of functionalized activated carbon.[49] The surface area of the functionalized activated carbon were found to increase by 1-6% after 24 hours hydrothermal treatment in water at 200 °C, which shows very good structural stability. Besides, carbon materials have high surface area, high resistance to acidic and basic condition, and also the potential to attach functionality, making it a good catalyst support material.[50] Mesoporous carbon material, with ordered pores and high surface

area, low impurities, has already found many applications in hydrothermal reactions.[51-53] Carbon nanotubes was also applied in biomass conversion reactions.[54-56]

Usually the higher carbon pyrolysis temperature results in better hydrothermal stability. The surface area of carbon coated silica gel synthesized at 400°C didn't decrease in water at 200°C for 12 hours.[42] Mesoporous carbon synthesized at 850°C was even stable in water at 500°C and 370 MPa verified by in situ small-angle X-ray scattering (SAXS).[57] Graphitic carbon coating by CVD onto Al_2O_3 also showed good hydrothermal stability with minimum change in surface area and pore structure after treated 12 hour in water at 200°C.[58]

1.5 Deactivation Mechanisms During Hydrothermal Conditions

While the paragraphs above discussed the hydrothermal stability of different catalyst support, this is only the first step towards a stable catalyst. There are several extensive review on the catalyst deactivation, which are useful for the deactivation under hydrothermal conditions.[59,60] The overall stability of the catalyst needs to be considered, including catalyst support and active sites. Below are some common deactivation mechanisms under hydrothermal conditions.

1.5.1 Support Collapse

Support collapse is usually because the structure changes of the support under hydrothermal conditions. As described above, alumina changes to boehmite, and silica undergoes hydrolysis.[42] As a result, the structure collapsed and surface area decreased. In many cases, this will lead to active metal particles sintering or buried inside the support structure, making the active sites inaccessible or reducing the amount of active sites.

1.5.2 Leaching

Leaching is the dissolution of active sites (metal or acid) or even catalyst support into the reaction solution. This process is affected by many parameters including temperature, pH, solvent, reactant, and product. Tessonnier et al. found that Al^{3+} and Si^{4+} leached from ZSM-5 during hydrothermal conditions at 170°C for 30 min.[40] Addition of a small amount of salt (NaCl) increased the leaching rate of Al^{3+}, which acts as a homogeneous catalyst for isomerization of glucose to fructose. The filtered solution from ZSM-5 was found active for the reaction as well. Carbon materials usually show better resistance towards acidic or corrosive solution than metal oxides.[61] Leaching has been found in other liquid phase organic reactions as well. Sheldon et al. observed the chromium leached into the solution was active for oxidation reaction.[62] It was suggested to filter catalyst at reaction temperature and test the filtrate in reaction for batch reactors. In flow reactors, analysis of the sample solution is enough as the catalyst is constantly flushed by solution. Besides, leached metal ions may cause pollution of the product and require purification in the later process.

1.5.3 Sintering

Sintering is usually referred to metal particles agglomerating to bigger particles due to thermodynamic instability. It is often observed in gas-phase reaction at high temperature. When it comes to aqueous-phase reaction, sintering happens even when the temperature is relatively low. Bond et al. reported sintering of Ru particles on TiO_2, carbon, SiO_2, and Al_2O_3 only at 50°C in aqueous-phase hydrogenation of levulinic acid.[63,64] Two sintering mechanisms has been proposed including Ostwald ripening and particle migration and coalescence.[65] As the aqueous-phase reactions are carried out below 250°C, particle migration and coalescence was unlikely to happen, while Ostwald ripening may be the cause.[61]

1.5.4 Carbonaceous Deposits

Carbonaceous deposits (Coke forming) are a common cause for deactivation in gas-phase reactions, especially at high temperature. However, it was also observed in biomass conversion reactions at low temperature as biomass-derived molecules contain significant oxygen functional groups, which are very reactive. Condensation, rearrangement reactions, and polymerization can occur, leading to carbonaceous deposition onto the catalyst. As a result, the active sites may be buried or the pores may be blocked. Usually the strong adsorption and low solubility of the carbonaceous deposition helped the deposition retains on the surface or inside the pores.[66] Since the biomass conversion is usually happening under 250°C, the carbonaceous deposition was likely non-polyaromatic.[66] Adsorption of glyceric acid was found to block the active site during glycerol oxidation on Pt-Bi catalyst.[67] This deactivation is reversible as the catalyst activity is usually recovered by treating the catalyst at high temperature in air or inert gas. While diluting the reactant is a possible way to reduce carbonaceous deposition, this may not be applicable for many industrial processes due to economic considerations.[68] Regeneration offers another way, but this may be limited in some applications. It is more attractive to tune the catalyst surface properties such as hydrophilicity or hydrophobicity and point of zero charge to prevent carbonaceous deposition in the first place.

1.5.5 Poisoning

As described in the challenges facing biomass conversion, the catalyst need to withstand biogenic impurities from fermentation besides normal poisons as chemical catalytic process is usually happening after biological process. These impurities include organic acid, amino acid, protein fragments, nutrients, inorganic salt, and fermentation byproducts.[69] Dumesic et al. showed that even low concentration of sulfur and nitrogen-containing impurities inhibited Pt, Pd,

and Ni catalyst.[28] The inhibition effects of thiamine HCl, systeine, methionine, biotin, tryptophan, niacin, threonine, and p-aminobenzoic acid were studied in cyclohexene hydrogenation. In Miller's research, organic acids, sugars, and inorganic salts were found not affect the catalytic reaction.[69] Alanine was found to competitively adsorb on the catalyst surface and the poisoning was reversible; while the cysteine and methionine resulted in irreversible poisoning of the catalyst in lactic acid hydrogenation to propylene glycol. Besides biogenic impurities from fermentation, poisoning species are likely to be generated during the reactions especially when dealing with sulfur and nitrogen containing reactants.[59] Recently, Davis et al. identified olefinic species as poisons for Pt on carbon during aqueous phase oxidations.[70] These poisoning species were generated during the reaction and could be removed by mild treatment in H_2.[70]

1.5.6 Restructuring of Active Sites

Restructuring of active sites such as changes in metal particle shape, structure, and composition occurs in monometallic, bimetallic, alloy, and mixed metal oxide catalyst. This restructuring may result in improved or decreased catalytic performance. Davis. et al observed that Sn would dealloy from bimetallic PtSn on carbon catalyst with increased activity in aqueous phase oxidation.[71] Albrecht. et al showed that $La_xZr_yO_z$ crystalized under hydrothermal conditions with enhanced activity and stability in aqueous phase ketonization.[35] Vardon et al. reported that Ru-Sn on activated carbon restructured with Ni from stainless steel reactor to form more favorable Ni-Sn sites with decreased activity during aqueous phase reduction of succinic acid.[72]

1.6 Strategies to Improve Hydrothermal Stability of Catalysts

While supported metal catalyst consist of catalyst support and supported metal as active sites, hydrothermal stability is required for catalyst support and active sites. Several reviews have discussed the methods to improve the hydrothermal stability of catalyst.[24,33,68] Though carbon, titania and zirconia showed better hydrothermal stability than other catalyst supports, the stability of active sites remains to be challenge. There are several reviews specifically on stabilizing metal particles against sintering, where some of the strategies can be applied to the design of hydrothermally stable catalyst.[73,74] It is worth noting that hydrothermal stability of catalyst may be affected by metal precursor and reaction conditions such as temperature, pH, reactant, and process conditions.[24,68] For example, using H_2PtCl_6 as precursor was found to decrease the point of zero charge of γ-Al_2O_3 and also the boehmite formation.[75] Sievers et al. observed different stability of Pt/γ-Al_2O_3 when treated in aqueous solution of biomass compounds with different chain lengths.[76] The formation of carbonaceous deposition reduced the boehmite formation and sintering of Pt particles.[76]Besides catalyst design strategies to improve the stability of catalyst, regeneration methods can also recover the catalytic activity. However, only a few papers tried to regenerate catalyst for hydrothermal conditions with limited recovery.[64] Discussed below are some catalyst design strategies regarding improving hydrothermal stability of catalysts.

1.6.1 Coating on Metal Oxide

Metal oxide supports generally have good mechanical strengths and high surface areas. These criterions are required not only in petroleum process, but also in biomass conversion. Thus much efforts was focused on improving the hydrothermal stability of metal oxide. Coating on metal oxide is one of the method to improve the stability of metal oxide. Datye et al. used carbon

coating over alumina and silica from the pyrolysis of sucrose.[42] Surface area and mesoporous structure were maintained after 12 hours of hydrothermal treatment in water at 200 °C. Chemical vapor deposition (CVD) of methane as the carbon source was also used to coat metal oxide by Datye et al. to coat γ-Al_2O_3 at 900 °C.[58] When coated with a graphitic carbon film, surface area, pore volume and pore size were well maintained after hydrothermal treatment in water at 220 °C for 12 hours. Aqueous-phase reforming of ethylene glycol at 250°C and hydrogenation of lactic acid to propylene glycol at 120 °C was used to test the stability of catalyst. Better stability was found on graphitic carbon coated γ-Al_2O_3 supported catalysts during both reactions with less sintering and almost no leaching. Recently, Medlin et al. found that organophosphonic acid coating improved the hydrothermal stability of γ-Al_2O_3, where surface area was maintained after the coating.[77] Silica coating on alumina was shown to improve the hydrothermal stability of alumina, but the silica coating eventually was hydrolysed and resulted in the destruction of the alumina phase.[78] Dumesic et al. used atomic layer deposition (ALD) of niobia to coat SBA-15.[79] Mesoporous structure and porosity were reserved after hydrothermal treatment at 200 °C when synthesized with above 10 cycles of ALD. A better stability was also observed on niobia coated SBA-15 supported Pd catalyst than commercial catalyst for aqueous-phase transformation of γ-valerolactone to pentanoic acid at 200 °C. Similarly, Huber et al. used ALD of TiO_2 coating on TiO_2 supported cobalt to improve the stability in aqueous-phase hydrogenation against leaching and sintering of cobalt.[80] During the calcination, pores were opened on the TiO_2 ALD coating and TiO_2 moved to defect sites, where sintering and leaching were likely to happen.

1.6.2 Carbon Overcoating on Metal Oxide Supported Metal Catalyst

While the method above describes coating the metal oxide first and then depositing active metal onto the support, Datye et al. developed a new method to coat the SiO_2 (or Al_2O_3)

supported metal catalysts with pyrolysis of sugar at 400°C.[81] The overcoated catalyst showed better stability in aqueous-phase hydrogenation of acetone and furfural. As verified by ^{13}C NMR, the carbon overlayer was moderately polycondensed aromatic structure with some oxygen-functional groups on the edge. Thus, the open structure of carbon layer made the active metal sites accessible to the reactant. However, this method may block some active sites inevitably.

1.6.3 Metal-Support Interaction

1.6.3.1 Strong Metal-Support Interactions

Strong metal-support interactions (SMSI) described changes in chemisorption behaviour when group VIII noble metals were supported on titanium oxide, niobium, manganese, and lanthanum.[82,83] For example, an overlayer of TiO_y was formed on top of the supported noble metals after treatment, thus the metal particles were covered and well-preserved. Huber et al. used high-temperature calcination and reduction to treat TiO_2 supported cobalt catalyst.[84] The TiO_y were found to cover the cobalt during high temperature calcination as a result of strong metal-support interaction followed by reduction of Co_3O_4 to metallic Co. The catalyst showed a good stability in aqueous-phase hydrogenation of furfural alcohol against leaching and sintering.

1.6.3.2 Heteroatom Doping

Heteroatom doping such as oxygen and nitrogen in carbon materials have been reported to improve the stability and activity of metal particles.[85,86] Graphitic carbon nitride have received much attention because of the unique structure and high nitrogen content.[87,88] We used oxygen and nitrogen doping in second and third chapter to study the improved stability of carbon supported Pd catalyst.

Heteroatom doping has also been applied on metal oxide to improve the stability as well. The addition of SiO_2 to and TiO_2 improved the stability of the metal oxide.[47] Datye et al. also

found the addition of silica helped to improve the stability of niobia and also suppressed the sintering of Pd particles in aqueous-phase conversion of GVL to pentanoic acid.[89]

1.6.3.3 Surface Modification

Compared with metal oxide, surface modification is more common applied on carbon materials. Beside, as metal oxide generally not stable under hydrothermal conditions, it may be difficult to improve the stability just by changing surface chemistry. Surface modification is often applied to the carbon surface after the carbon material is synthesized. Carbon surface modifications including treatment in nitric acid, hydrogen peroxide, sulfuric acid, ammonia hydroxide, ammonia gas, and oxidation in air, were usually applied to change the surface properties, thus increase the interaction with metal precursor.[90-96] Either basic or acidic functional groups can be attached to the carbon surface after the treatment. As a result, a higher dispersion and stability may be achieved. Few studies have been focused on the effect of carbon surface modification on hydrothermal stability. This method may produce some new stable catalyst, give insight into the stability of the specific surface functional groups and the interaction of the surface functional groups and anchored metal particles.

1.6.4 Bimetallic Catalyst

Besides increasing activity and selectivity, addition of a second metal into the monometallic catalyst may lead to better stability of the catalyst.[21] Sintering, leaching, and carbonaceous deposition on the catalyst may be reduced because of the tuned electronic and geometric structures. Solarino et al. observed an improved stability of Ni-Ru bimetallic catalyst compared with Ni catalyst for CO_2 reforming of methane.[97] Recently, Vardon et al. showed that Ru-Sn on carbon with a stable activity during continuous flow aqueous phase reduction of

succinic acid.[72] More research needs to be done to investigate the improved stability of bimetallic catalysts especially for biomass conversions.

1.6.5 Embedding Metal Particles into Support

Embedding metal particles into the support can help to further stabilize metal nanoparticles. The challenge is to find the right method and material to do so. Besides, it should be noted that embedding metal particles will inevitably bury some active sites depending on how deep the nanoparticles are embedded. However, it is an interplay between the stability and activity of the metal nanoparticles since the stabilizing effect might be diminished if the embedding is too shallow. Irvine et al. demonstrated that Ni particles with enhanced stability against sintering and coking when socketed on perovskite from exsolution.[98] Though this was for gas phase reactions, there is no reason why this embedding cannot be applied to catalyst design for hydrothermal conditions. In the fourth chapter, we tried to embed Pt nanoparticles by polymer coating on carbon material with a stable catalytic activity.

1.6.6 Other Novel Catalyst

New challenges usually need new methods and strategies to tackle. It is likely that there will be more novel catalyst designed for hydrothermal conditions. Datye et al. used deposition precipitation carbonization (DPC) method to synthesize small niobia particles embedded in the carbon.[99] The material showed better hydrothermal stability than amorphous niobia as a result of suppressed crystallization of niobia to bigger particles.

1.7 General Concerns about Hydrothermal Stability Studies

Here are some general concerns regarding developing catalysts for hydrothermal reactions.

1. Hydrothermal stability is directly related with the hydrothermal conditions. Different applications may require different strategy to improve the catalyst stability.

2. More than one type of deactivation is likely to occur under hydrothermal conditions. It is important to address each of the deactivation for catalyst stability test. A good catalyst synthesis and design strategy may mitigate several deactivations at the same time.

3. While in-situ characterizations may not be applicable to investigate the changes in catalyst under hydrothermal reactions contemporarily, characterization of the catalyst after reaction is especially important in catalyst stability studies to capture any changes in the catalyst structure and chemistry.

4. It is important to know that a stable catalytic performance under reaction conditions requires relevant reactor design and process control. Ni leached from stainless steel reactor was found to form Ni-Sn from Ru-Sn on carbon and deactivate the catalyst during aqueous phase reactions, which required special coating on the reactor to achieve a stable catalytic activity.[72] By carefully control the process conditions, the catalyst may deactivate more slowly as well. However, the process conditions are usually chosen with other factors such as separation cost and production rate.

5. When it comes to stability study, many research papers were using full conversion in repeated batch reactions or flow reactions. However, limited deactivation information can be obtained as the full conversion could be due to excess catalyst loading. Intermediate conversion in a continuous flow reactor would be ideal to study the catalyst deactivations.

1.8 Thesis Outline

Hydrothermal stability of catalyst emerges to be a challenge with increasing attention on biomass conversion to fuels and chemicals. More research needs to be done about investigating

the mechanism of deactivation as well as developing hydrothermally stable catalyst under these conditions. Here in the second chapter, we studied how the oxygen functional groups in carbon support is affecting the dispersion and stability of Pd catalysts. Detailed ^{13}C NMR also revealed the surface chemistry of the carbon materials pyrolyzed at different temperatures. Low-temperature synthesized carbon materials contained more oxygen-functional groups and better stabilized Pd particles. In third chapter, we further improved the hydrothermal stability of catalyst by introduction of nitrogen heteroatoms. ^{13}C and ^{15}N NMR was used to characterize the surface chemistry of carbon coating and investigate surface functional groups changes during hydrothermal conditions. Improved stability of Pd particles was observed with reduced sintering and leaching. A new PANI coated carbon supported Pt was synthesized in the fourth chapter and found to stabilize Pt nanoparticles. Besides, a simple regeneration including low temperature air oxidation and H_2 reduction was able to fully recover the catalytic activity. This regeneration was also effective for Ru catalysts. The fifth and sixth chapter summarizes the thesis and raises some further directions.

1.9 References

1. Brown, R. C.; Brown, T. R. *Biorenewable Resources: Engineering New Products from Agriculture, 2nd Edition* **2014**, 1-375.

2. Perlack, R. D.; Wright, L. L.; Turhollow, A. F.; Graham, R. L.; Stokes, B. J.; Erbach, D. C. *Biomass as Feedstock for A Bioenergy and Bioproducts Industry: The Technical Feasibility of a Billion-Ton Annual Supply*; Oak Ridge National Laboratory: APR 2005.

3. Chheda, J. N.; Huber, G. W.; Dumesic, J. A. *Angew. Chem. Int. Ed.* **2007,** *46* (38), 7164-7183.

4. Li, C. Z.; Zhao, X. C.; Wang, A. Q.; Huber, G. W.; Zhang, T. *Chem. Rev.* **2015,** *115* (21), 11559-11624.

5. Serrano-Ruiz, J. C.; Luque, R.; Sepulveda-Escribano, A. *Chem. Soc. Rev.* **2011,** *40* (11), 5266-5281.

6. Huber, G. W.; Iborra, S.; Corma, A. *Chem. Rev.* **2006,** *106* (9), 4044-4098.

7. Rinaldi, R.; Schuth, F. *Energy Environ. Sci.* **2009,** *2* (6), 610-626.

8. Climent, M. J.; Corma, A.; Iborra, S. *Green Chem.* **2014,** *16* (2), 516-547.

9. Huber, G. W.; Dumesic, J. A. *Catal. Today* **2006,** *111* (1-2), 119-132.

10. Marshall, J. *New Sci.* **2007,** *195* (2611), 28-31.

11. Climent, M. J.; Corma, A.; Iborra, S. *Green Chem.* **2011,** *13* (3), 520-540.

12. Biddy, M. J.; Scarlet, C.; Minchin, C. *Chemicals from Biomass: A Market Assessment of Bioproducts with Near-Term Potential*; March 2016.

13. Gallezot, P. *Chem. Soc. Rev.* **2012,** *41* (4), 1538-1558.

14. Anastas, P. T.; Zimmerman, J. B. *Environ. Sci. Technol.* **2003,** *37* (5), 94A-101A.

15. Bozell, J. J.; Astner, A.; Baker, D.; Biannic, B.; Cedeno, D.; Elder, T.; Hosseinaei, O.; Delbeck, L.; Kim, J. W.; O'Lenick, C. J.; Young, T. *Bioenergy Res.* **2014,** *7* (3), 856-866.

16. Schwartz, T. J.; O'Neill, B. J.; Shanks, B. H.; Dumesic, J. A. *ACS Catal.* **2014,** *4* (6), 2060-2069.

17. Schwartz, T. J.; Shanks, B. H.; Dumesic, J. A. *Curr. Opin. Biotechnol.* **2016,** *38*, 54-62.

18. Shanks, B. H. *ACS Chem. Biol.* **2007,** *2* (8), 533-535.

19. Shanks, B. H. *ChemSusChem* **2015,** *8* (6), 928-930.

20. Sankar, M.; Dimitratos, N.; Miedziak, P. J.; Wells, P. P.; Kiely, C. J.; Hutchings, G. J. *Chem. Soc. Rev.* **2012,** *41* (24), 8099-8139.

21. Alonso, D. M.; Wettstein, S. G.; Dumesic, J. A. *Chem. Soc. Rev.* **2012,** *41* (24), 8075-8098.

22. Huber, G. W.; Shabaker, J. W.; Evans, S. T.; Dumesic, J. A. *Appl. Catal., B* **2006,** *62* (3-4), 226-235.

23. Kim, Y. T.; Dumesic, J. A.; Huber, G. W. *J. Catal.* **2013,** *304*, 72-85.

24. Heroguel, F.; Rozmyslowicz, B.; Luterbacher, J. S. *Chimia* **2015,** *69* (10), 582-591.

25. Sievers, C.; Noda, Y.; Qi, L.; Albuquerque, E. M.; Rioux, R. M.; Scott, S. L. *ACS Catal.* **2016,** *6* (12), 8286-8307.

26. Sheldon, R. A. *Green Chem.* **2005,** *7* (5), 267-278.

27. Sheldon, R. A. *Chem. Soc. Rev.* **2012,** *41* (4), 1437-1451.

28. Schwartz, T. J.; Brentzel, Z. J.; Dumesic, J. A. *Catal. Lett.* **2015,** *145* (1), 15-22.

29. Schwartz, T. J.; Johnson, R. L.; Cardenas, J.; Okerlund, A.; Da Silva, N. A.; Schmidt-Rohr, K.; Dumesic, J. A. *Angew. Chem. Int. Ed.* **2014,** *53* (47), 12718-12722.

30. Suastegui, M.; Matthiesen, J. E.; Carraher, J. M.; Hernandez, N.; Quiroz, N. R.; Okerlund, A.; Cochran, E. W.; Shao, Z. Y.; Tessonnier, J. P. *Angew. Chem. Int. Ed.* **2016,** *55* (7), 2368-2373.

31. Andanson, J. M.; Baiker, A. *Chem. Soc. Rev.* **2010,** *39* (12), 4571-4584.

32. Somorjai, G. A.; York, R. L.; Butcher, D.; Park, J. Y. *Phys. Chem. Chem. Phys.* **2007,** *9* (27), 3500-3513.

33. Xiong, H.; Pham, H. N.; Datye, A. K. *Green Chem.* **2014,** *16* (11), 4627-4643.

34. Lucas, M.; Fabicovicova, K.; Claus, P. *ChemCatChem* **2018,** *10* (3), 612-618.

35. Lopez-Ruiz, J. A.; Cooper, A. R.; Li, G. S.; Albrecht, K. O. *ACS Catal.* **2017,** *7* (10), 6400-6412.

36. Pagan-Torres, Y. J.; Wang, T.; Gallo, J. M. R.; Shanks, B. H.; Dumesic, J. A. *ACS Catal.* **2012,** *2* (6), 930-934.

37. Wang, T.; Pagan-Torres, Y. J.; Combs, E. J.; Dumesic, J. A.; Shanks, B. H. *Top. Catal.* **2012,** *55* (7-10), 657-662.

38. van der Graaf, W. N. P.; Tempelman, C. H. L.; Hendriks, F. C.; Ruiz-Martinez, J.; Bals, S.; Weckhuysen, B. M.; Pidko, E. A.; Hensen, E. J. M. *Appl. Catal. A* **2018,** *564*, 113-122.

39. Ravenelle, R. M.; Schussler, F.; D'Amico, A.; Danilina, N.; van Bokhoven, J. A.; Lercher, J. A.; Jones, C. W.; Sievers, C. *J. Phys. Chem. C* **2010,** *114* (46), 19582-19595.

40. Gardner, D. W.; Huo, J.; Hoff, T. C.; Johnson, R. L.; Shanks, B. H.; Tessonnier, J.-P. *ACS Catal.* **2015,** *5* (7), 4418-4422.

41. Man, K. J.; Ryong, R. *Bull. Korean Chem. Soc.* **1996,** *17* (1), 66-68.

42. Pham, H. N.; Anderson, A. E.; Johnson, R. L.; Schmidt-Rohr, K.; Datye, A. K. *Angew. Chem. Int. Ed.* **2012,** *51* (52), 13163-13167.

43. Pollock, R. A.; Gor, G. Y.; Walsh, B. R.; Fry, J.; Ghampson, I. T.; Melnichenko, Y. B.; Kaiser, H.; DeSisto, W. J.; Wheeler, M. C.; Frederick, B. G. *J. Phys. Chem. C* **2012,** *116* (43), 22802-22814.

44. Ravenelle, R. M.; Copeland, J. R.; Kim, W. G.; Crittenden, J. C.; Sievers, C. *ACS Catal.* **2011,** *1* (5), 552-561.

45. Pintar, A.; Besson, M.; Gallezot, P. *Appl. Catal. B* **2001,** *30* (1-2), 123-139.

46. Pintar, A.; Besson, M.; Gallezot, P. *Appl. Catal. B* **2001,** *31* (4), 275-290.

47. Duan, J. Z.; Kim, Y. T.; Lou, H.; Huber, G. W. *Catal. Today* **2014,** *234*, 66-74.

48. Auer, E.; Freund, A.; Pietsch, J.; Tacke, T. *Appl. Catal. A* **1998,** *173* (2), 259-271.

49. Van Pelt, A. H.; Simakova, O. A.; Schimming, S. M.; Ewbank, J. L.; Foo, G. S.; Pidko, E. A.; Hensen, E. J. M.; Sievers, C. *Carbon* **2014,** *77*, 143-154.

50. De, S.; Duttab, S.; Saha, B. *Catal. Sci. Technol.* **2016,** *6* (20), 7364-7385.

51. Kim, T. W.; Park, I. S.; Ryoo, R. *Angew. Chem. Int. Ed.* **2003,** *42* (36), 4375-4379.

52. Xia, Y. D.; Mokaya, R. *Adv. Mater.* **2004,** *16* (17), 1553-1558.

53. Jun, S.; Joo, S. H.; Ryoo, R.; Kruk, M.; Jaroniec, M.; Liu, Z.; Ohsuna, T.; Terasaki, O. *JACS* **2000,** *122* (43), 10712-10713.

54. Crossley, S.; Faria, J.; Shen, M.; Resasco, D. E. *Science* **2010,** *327* (5961), 68-72.

55. Tessonnier, J. P.; Villa, A.; Majoulet, O.; Su, D. S.; Schlogl, R. *Angew. Chem. Int. Ed.* **2009,** *48* (35), 6543-6546.

56. Zhou, C. M.; Deng, W. P.; Wan, X. Y.; Zhang, Q. H.; Yang, Y. H.; Wang, Y. *ChemCatChem* **2015,** *7* (18), 2853-2863.

57. Mayanovic, R. A.; Yan, H.; Brandt, A. D.; Wang, Z.; Mandal, M.; Landskron, K.; Bassett, W. A. *Microporous Mesoporous Mater.* **2014,** *195*, 161-166.

58. Xiong, H.; Schwartz, T. J.; Andersen, N. I.; Dumesic, J. A.; Datye, A. K. *Angew. Chem. Int. Ed.* **2015,** *54* (27), 7939-7943.

59. Argyle, M. D.; Bartholomew, C. H. *Catalysts* **2015,** *5* (1), 145-269.

60. Bartholomew, C. H. *Appl. Catal. A.* **2001,** *212* (1-2), 17-60.

61. Besson, M.; Gallezot, P. *Catal. Today* **2003,** *81* (4), 547-559.

62. Sheldon, R. A.; Wallau, M.; Arends, I.; Schuchardt, U. *Acc. Chem. Res.* **1998,** *31* (8), 485-493.

63. Abdelrahman, O. A.; Heyden, A.; Bond, J. Q. *ACS Catal.* **2014,** *4* (4), 1171-1181.

64. Abdelrahman, O. A.; Luo, H. Y.; Heyden, A.; Roman-Leshkov, Y.; Bond, J. Q. *J. Catal.* **2015,** *329*, 10-21.

65. Hansen, T. W.; Delariva, A. T.; Challa, S. R.; Datye, A. K. *Acc. Chem. Res.* **2013,** *46* (8), 1720-1730.

66. Guisnet, M.; Magnoux, P. *Appl. Catal. A* **2001,** *212* (1-2), 83-96.

67. Worz, N.; Brandner, A.; Claus, P. *J. Phys. Chem. C* **2010,** *114* (2), 1164-1172.

68. Lange, J.-P. *Angew. Chem. Int. Ed.* **2015,** *54* (45), 13186-13197.

69. Zhang, Z. G.; Jackson, J. E.; Miller, D. J. *Bioresour. Technol.* **2008,** *99* (13), 5873-5880.

70. Xie, J. H.; Duan, P.; Kaylor, N.; Yin, K. H.; Huang, B.; Schmidt-Rohr, K.; Davis, R. J. *ACS Catal.* **2017,** *7* (10), 6745-6756.

71. Xie, J. H.; Falcone, D. D.; Davis, R. J. *J. Catal.* **2015,** *332*, 38-50.

72. Vardon, D. R.; Settle, A. E.; Vorotnikov, V.; Menart, M. J.; Eaton, T. R.; Unocic, K. A.; Steirer, K. X.; Wood, K. N.; Cleveland, N. S.; Moyer, K. E.; Michener, W. E.; Beckham, G. T. *ACS Catal.* **2017,** *7* (9), 6207-6219.

73. Cao, A.; Lu, R.; Veser, G. *Phys. Chem. Chem. Phys.* **2010,** *12* (41), 13499-13510.

74. Goodman, E. D.; Schwalbe, J. A.; Cargnello, M. *ACS Catal.* **2017,** *7* (10), 7156-7173.

75. Ravenelle, R. M.; Diallo, F. Z.; Crittenden, J. C.; Sievers, C. *ChemCatChem* **2012,** *4* (4), 492-494.

76. Ravenelle, R. M.; Copeland, J. R.; Van Pelt, A. H.; Crittenden, J. C.; Sievers, C. *Top. Catal.* **2012,** *55* (3-4), 162-174.

77. Van Cleve, T.; Underhill, D.; Rodrigues, M. V.; Sievers, C.; Medlin, J. W. *Langmuir* **2018,** *34* (12), 3619-3625.

78. Liu, F.; Okolie, C.; Ravenelle, R. M.; Crittenden, J. C.; Sievers, C.; Bruijnincx, P. C. A.; Weckhuysen, B. M. *Appl. Catal. A.* **2018,** *551*, 13-22.

79. Pagan-Torres, Y. J.; Gallo, J. M. R.; Wang, D.; Pham, H. N.; Libera, J. A.; Marshall, C. L.; Elam, J. W.; Datye, A. K.; Dumesic, J. A. *ACS Catal.* **2011,** *1* (10), 1234-1245.

80. Lee, J. C.; Jackson, D. H. K.; Li, T.; Winans, R. E.; Dumesic, J. A.; Kuech, T. F.; Huber, G. W. *Energy Environ. Sci.* **2014,** *7* (5), 1657-1660.

81. Pham, H. N.; Anderson, A. E.; Johnson, R. L.; Schwartz, T. J.; O'Neill, B. J.; Duan, P.; Schmidt-Rohr, K.; Dumesic, J. A.; Datye, A. K. *ACS Catal.* **2015,** *5* (8), 4546-4555.

82. Tauster, S. J.; Fung, S. C.; Garten, R. L. *JACS* **1978,** *100* (1), 170-175.

83. Tauster, S. J. *Acc. Chem. Res.* **1987,** *20* (11), 389-394.

84. Lee, J.; Burt, S. P.; Carrero, C. A.; Alba-Rubio, A. C.; Ro, I.; O'Neill, B. J.; Kim, H. J.; Jackson, D. H. K.; Kuech, T. F.; Hermans, I.; Dumesic, J. A.; Huber, G. W. *J. Catal.* **2015,** *330*, 19-27.

85. Zhang, P. F.; Gong, Y. T.; Li, H. R.; Chen, Z. R.; Wang, Y. *Nat. Commun.* **2013,** *4*.

86. Xu, X.; Li, Y.; Gong, Y. T.; Zhang, P. F.; Li, H. R.; Wang, Y. *JACS* **2012,** *134* (41), 16987-16990.

87. Wang, Y.; Wang, X. C.; Antonietti, M. *Angew. Chem. Int. Ed.* **2012,** *51* (1), 68-89.

88. Wang, Y.; Yao, J.; Li, H. R.; Su, D. S.; Antonietti, M. *JACS* **2011,** *133* (8), 2362-2365.

89. Pharn, H. N.; Pagan-Torres, Y. J.; Serrano-Ruiz, J. C.; Wang, D.; Dumesic, J. A.; Datye, A. K. *Appl. Catal. A* **2011,** *397* (1-2), 153-162.

90. Toebes, M. L.; Prinsloo, F. F.; Bitter, J. H.; van Dillen, A. J.; de Jong, K. P. *J. Catal.* **2003,** *214* (1), 78-87.

91. Pradoburguete, C.; Linaressolano, A.; Rodriguezreinoso, F.; Delecea, C. S. *J. Catal.* **1989,** *115* (1), 98-106.

92. Solhy, A.; Machado, B. F.; Beausoleil, J.; Kihn, Y.; Goncalves, F.; Pereira, M. F. R.; Orfao, J. J. M.; Figueiredo, J. L.; Faria, J. L.; Serp, P. *Carbon* **2008,** *46* (9), 1194-1207.

93. Wan, X.; Zhou, C.; Chen, J.; Deng, W.; Zhang, Q.; Yang, Y.; Wang, Y. *ACS Catal.* **2014,** *4* (7), 2175-2185.

94. Morenocastilla, C.; Ferrogarcia, M. A.; Joly, J. P.; Bautistatoledo, I.; Carrascomarin, F.; Riverautrilla, J. *Langmuir* **1995,** *11* (11), 4386-4392.

95. Datsyuk, V.; Kalyva, M.; Papagelis, K.; Parthenios, J.; Tasis, D.; Siokou, A.; Kallitsis, I.; Galiotis, C. *Carbon* **2008,** *46* (6), 833-840.

96. Shen, W. Z.; Fan, W. B. *J. Mater. Chem. A* **2013,** *1* (4), 999-1013.

97. Crisafulli, C.; Scire, S.; Minico, S.; Solarino, L. *Appl. Catal. A* **2002,** *225* (1-2), 1-9.

98. Neagu, D.; Oh, T. S.; Miller, D. N.; Menard, H.; Bukhari, S. M.; Gamble, S. R.; Gorte, R. J.; Vohs, J. M.; Irvine, J. T. S. *Nat. Commun.* **2015,** *6*.

99. Xiong, H. F.; Pham, H. N.; Datye, A. K. *J. Catal.* **2013,** *302*, 93-100.

CHAPTER 2. STABILITY OF PD NANOPARTICLES ON CARBON-COATED SUPPORTS UNDER HYDROTHERMAL CONDITIONS

A paper published on Catalysis Science & Technology

Jiajie Huo,[ab] Robert L. Johnson,[ab] Pu Duan,[bc] Hien N. Pham,[bd] Deyny Mendivelso-Perez,[e] Emily A. Smith,[e] Abhaya K. Datye,[bd] Klaus Schmidt-Rohr,[bc] Brent H. Shanks[ab,*]

[a]Department of Chemical and Biological Engineering, Iowa State University, Ames, Iowa 50011, United States

[b]Center for Biorenewable Chemicals, Iowa State University, Ames, Iowa 50011, United States

[c]Department of Chemistry, Brandeis University, Waltham, Massachusetts 02453, United States

[d]Department of Chemical and Biological Engineering and Center for Microengineered Materials, University of New Mexico, Albuquerque, New Mexico 87131, United States

[e]The Ames Laboratory, U.S. Department of Energy, and Department of Chemistry, Iowa State University, Ames, Iowa 50011, United States

*Corresponding Author

Abstract

Hydrothermal stability is one of the major challenges facing heterogeneous catalysis in biomass conversion to chemicals or fuels. Though carbon supports have shown better hydrothermal stability than common metal oxide supports like alumina and silica, improving the stability of metal nanoparticles supported on carbon still remains a challenge. In this work, carbon-coated SBA-15 (mesoporous silica) materials in which thin carbon overlayer were pyrolyzed at 300, 400, and 600 °C giving different surface chemistry, as quantitatively verified by ^{13}C NMR and XPS. As the pyrolysis temperature increased, the carbon overlayer had fewer oxygen functional groups and more aromatic groups. After depositing Pd nanoparticles on the

support, hydrothermal treatments and aqueous-phase furfural hydrogenation were used to test the catalyst stability. Better Pd dispersion and enhanced hydrothermal stability were observed when Pd was supported on the carbon-coated SBA-15 pyrolyzed at lower temperature.

2.1 Introduction

The transformation of biomass and biomass-derivatives into chemicals or biofuels is commonly performed in aqueous phase at elevated temperatures and pressures.[1-3] These conditions pose a major challenge for the heterogeneous catalysts needed for future biorefineries, compared with processing in the petroleum industry where very little water is present.[4-7] Unfortunately, common catalyst supports like alumina, silica, and zeolites are typically not stable under these conditions.[8-12] For example, the ordered ordered mesoporous structure of SBA-15 was destroyed with a drastic decrease in surface area from 740 $m^2 g^{-1}$ to only 30 $m^2 g^{-1}$ under hydrothermal conditions at 200 °C for 12 hours.[8] From previous studies, a thin carbon coating on oxide supports, via aqueous-phase deposition or chemical vapor deposition (CVD), has been shown to significantly improve their hydrothermal stability.[8,13,14] The atomic layer deposition (ALD) technique was also used to improve the stability of supported metal catalysts via oxide coating.[15] Compared to bulk carbon materials like carbon nanotubes, activated carbon, or mesoporous carbon that have been studied extensively, readily synthesized mesoporous carbon-coated metal oxide supports may have better mechanical properties.[13] While carbon supports show better hydrothermal stability than metal oxide supports, and carbon materials pyrolyzed at higher temperatures are more hydrothermally stable,[16] the stability of supported metal catalysts on carbon supports is another important consideration. Carbon-supported metal catalysts may deactivate due to sintering or leaching of the metal phase during the reaction, which may be

caused by weak interaction with the support or by loss of surface functional groups on the carbon, especially in the aqueous phase.[17-19]

The carbon–metal interaction is likely dependent on the carbon surface chemistry. As a result, post-synthesis methods are often used to modify the surface chemistry of the carbon, such as oxidation by nitric acid, hydrogen peroxide or other oxidizing chemicals to introduce defects or oxygen groups onto the carbon support, which can act as anchors for the metal precursor, thus helping to disperse and stabilize metal nanoparticles.[20-23] However, this step involves the reflux of harsh oxidative chemicals. Alternatively, different oxygen-containing functional groups are retained on the carbon surface after pyrolysis of carbohydrates to obtain the carbon material, depending on the synthesis temperature; these may act as anchors for metal nanoparticles, thus eliminating the need for a surface-modification step.

While the carbon surface chemistry is crucial for carbon-metal interaction, quantifying the carbon surface chemistry and tracking the changes in carbon surface chemistry during hydrothermal treatment have remained a challenge. Carbon surface functional groups are usually characterized by Boehm titration, FTIR, XPS and TPD-MS. However, with Boehm titration, only basic or acidic oxygen functional groups can be identified, while FTIR fails to give quantitative information about surface functional groups.[24,25] TPD-MS of CO and CO_2 can be used to identify and estimate the amount of surface functional groups only based on a carefully deconvoluted peak fitting.[26] A similar overlap problem arises with XPS, which becomes complicated when many different oxygen functional groups are present on a series of carbon materials.[25] Solid state ^{13}C nuclear magnetic resonance (NMR) opens a new approach for characterizing carbon surface oxygen functionalities.[27-29]

In this work, we show that SBA-15 materials coated with a thin carbon overlayer (C/SBA-15) and pyrolyzed at different temperatures yield different oxygen contents. Low-temperature carbon had more oxygen-containing groups like furans, carboxylic acids, phenols, or carbonyls, while high-temperature carbon had less oxygen and a higher aromatic content, as confirmed by ^{13}C NMR. Importantly, extensive characterization was performed on the carbon-coated supports by ^{13}C NMR, XPS, Raman spectroscopy, electron microscopy, elemental analysis, and TGA, which provided detailed compositional information beyond that previously reported. It was investigated whether carbon supports pyrolyzed at lower temperature having more oxygen-containing surface groups than carbon supports pyrolyzed at higher temperature could help disperse and stabilize the Pd nanoparticles.

2.2 Experiment Section

2.2.1 Catalyst Preparation

Mesoporous SBA-15 was prepared from tetraethyl orthosilicate (98%, Sigma Aldrich), Pluronic P123 (surfactant, BASF) and hydrochloric acid (36.5 wt%, Fisher Scientific) following the procedure described elsewhere.[30] SBA-15 (1 gram) was mixed with glucose (0.5 gram, D-glucose anhydrous, Fisher Scientific) in 20 mL of nanopure water. The mixture of glucose, SBA-15 and water was stirred under ambient pressure at room temperature until all the water had evaporated and then homogenized using a porcelain mortar and pestle. The powder mixture was transferred into a glass boat and put into a quartz tube within in a tube furnace. The powder was flushed with 200 mL min^{-1} argon (UHP, Airgas) for 30 min and then heated at a 5 °C min^{-1} ramp to 300, 400, or 600 °C, respectively, for 10 h. After washing with 1 M HCl in a sonicator for 30 min, the carbon-coated SBA-15 material was washed with deionized water, filtered under vacuum and dried in an oven overnight. The carbon materials obtained were denoted as

300C/SBA-15, 400C/SBA-15, and 600C/SBA-15, respectively. ^{13}C labeled D-glucose (U-^{13}C, 99%, Cambridge Isotope Laboratories) was used to synthesize carbon-coated SBA-15 materials in the same manner for ^{13}C NMR analysis. Incipient wetness impregnation was used to deposit 5 wt% Pd onto the carbon/SBA-15 supports from a palladium acetate (99.98%, Sigma Aldrich) solution in acetone. Palladium acetate was dissolved in the acetone solution by sonication for 30 min. After impregnation, the catalyst was dried at room temperature and reduced in a 200 mL min^{-1} hydrogen gas flow at 200 °C for 2 hr using a ramp rate of 2 °C min^{-1}.

2.2.2 Catalyst Characterization

The BET surface area was measured with a Micrometrics ASAP 2020 at -196 °C after degassing for 4 h. Pore volume was determined at a relative pressure of 0.973 and pore sizes from the adsorption isotherm were calculated by the BJH method. Pulse chemisorption of CO (10% CO in helium) was performed using a Micrometrics ASAP 2920 at 35 °C after *in situ* reduction in H_2 at 200 °C for 2 h and flushing with helium (UHP, Airgas) at 200 °C for 15 min to remove any adsorbed H_2. A stoichiometric Pd/CO factor of 2 was used for calculation as suggested in the literature.[31,32] Raman measurements were performed at ambient temperature using a lab-built microscope based on a DM IRBE platform (Leica, Wetzlar, Germany) equipped with a 532-nm laser excitation source (Sapphire SF 532 nm, Coherent, Santa Clara, CA, USA) operated at 25 mW. A 10× objective with a 0.9 numerical aperture was used to collect the Raman signal. The collected signal was focused with a lens onto a HoloSpec *f*/1.8i spectrograph (Kaiser Optical Systems, Ann Arbor MI, USA) equipped with a broad-range grating (HFG-650, Kaiser Optical Systems) and directed to a CCD detector (Newton 940, Andor Technology, Belfast, UK). A graphite standard (Sigma-Aldrich synthetic graphite, Lot# 08017EH) was used as a reference. Approximately 15 mg of sample was pressed onto a glass slide forming a dense layer about 1

mm thick, and placed on the microscope sample holder for analysis. Reported spectra were the average from 10 subsamples acquired in triplicate, for a total of 30 spectra, with a 0.1 s acquisition time for each spectrum. Spectra were then analyzed using Igor Pro 6.37 scientific analysis and graphing software (Wavemetrics, Lake Oswego, OR, USA). The spectra were fitted to a Gaussian model with a linear baseline using the multi-peak fit function. *Ex-situ* X-ray photoelectron spectroscopy (XPS) was applied using a Kratos Amicus/ESCA 3400 instrument with unmonochromated Mg Kα X-rays. CasaXPS was used to process the raw data. Elemental analysis was conducted on a CHNS elemental analyzer (Vario MICRO cube) with the experiments performed in triplicate. ICP-OES was performed using a PerkinElmer Optima 8000 ICP-OES Spectrometer. A known amount of catalyst was treated in freshly-made aqua regia for 24 h, diluted with water, and filtered using a 0.2- μm syringe filter before ICP analysis. TGA-MS-IR was performed using a Netzsch STA449 F1 with a mass spectrometer (Netzsch QMS 403 D Aeolos) and a FTIR detector (Bruker Tensor 37). The sample was first treated in argon (UHP, Airgas) at 150 °C for 20 min to remove adsorbed water and the analysis was performed in argon (UHP, Airgas) from 150 to 900 °C. For electron microscopy, samples were dispersed in ethanol and mounted on holey carbon grids for examination in a JEOL 2010F 200 kV transmission electron microscope and images were recorded in high angle annular dark field (HAADF) mode. At least 250 Pd particles were counted for particle size distribution analysis.

2.2.3 Hydrothermal Treatment

Hydrothermal treatment was performed in a 10-mL thick-wall glass vial. A known amount of catalyst was put in the tube with 6 mL nanopure water together with a triangular stirring bar. The vial containing the sample was treated in an oil bath at 170 °C for 24 h at 400 rpm stirring. The catalyst was filtered and dried after treatment. A portion of the catalyst was

collected for analysis. The remainder underwent a second hydrothermal treatment. BET surface area measurement, chemisorption and HAADF-STEM were used to characterize the catalyst after each hydrothermal treatment. ICP-OES was used to determine the composition of the hydrothermal treatment solution.

2.2.4 Reaction Testing

A furfural (99%, from Sigma-Aldrich) solution (60 mL of 10 g L^{-1} in water) was loaded in a Parr reactor (4590 Micro reactor with a 4871 process controller and a 4875 power controller) together with 10 mg of catalyst. After purging with N_2 three times, the reactor was heated to 80 °C under 200 rpm stirring. After the temperature reached 80 °C and the stirring speed was increased to 800 rpm, 760 psig hydrogen gas was introduced into the reactor. After 15 min of reaction, the heating jacket was removed and the reactor vessel was immediately immersed in an ice bath to cool it down. Within 5 min, the reactor cooled to room temperature. Pressure was released when the temperature was below 30 °C. The reactor was unloaded and the sample solution was collected and filtered using a 0.2 μm syringe filter for analysis in a gas chromatography (Agilent 7890A) with a flame ionization detector (FID) and an HP-5 ms column. The conversion was calculated from the amount of furfural before and after reaction. There were unidentified peaks from the gas chromatograph, which were likely attributable to degradation products. As a result, the carbon balances were all around 80% as quantified from total furfural, furfuryl alcohol and tetrahydrofurfuryl alcohol. Between reactions, a blank furfural solution without catalyst was used to verify that there was no catalyst residue inside the reactor. The effect of stirring speed was evaluated using the Pd 600C/SBA-15 catalyst. 800 rpm was required to ensure that there was no external mass transfer on the reaction condition used.

Duplicate runs were performed on the catalytic reaction before and after the first hydrothermal treatment on the catalysts.

2.2.5 Solid-State ^{13}C NMR

Solid-state ^{13}C NMR was performed on the carbon overlayers synthesized from ^{13}C-enriched glucose. Samples were packed into 4 mm outer-diameter zirconia rotors. 300C/SBA-15 was packed as received, while 400C/SBA-15 and 600C/SBA-15 were mixed (at 2 : 5 and 1 : 5 mass ratios, respectively) with a nonconductive inert filler, tricalcium phosphate, to reduce radio-frequency power absorption resulting from eddy currents in the sample. ^{13}C NMR spectra were recorded at 100 MHz on a Bruker DSX400 spectrometer. Quantitative ^{13}C spectra were measured under 14-kHz magic angle spinning (MAS) and high-power ^{1}H decoupling, using direct polarization (DP) with a 90° excitation pulse and a rotation-synchronized Hahn echo before detection, with recycling delays of 40 s; quantitative spectra of nonprotonated carbon or mobile segments were obtained by using 68 μs of recoupled dipolar dephasing before detection.[33] To detect the connectivities between protonated and nonprotonated carbons in 300C/SBA-15, two-dimensional exchange with protonated and nonprotonated spectral editing (EXPANSE) NMR spectra[28] were recorded with a mixing time of 10 ms. Since small residual diagonal peaks of arenes do not interfere with detection of most of the cross peaks, the dipolar dephasing difference[28] was not recorded, which maximized the signal-to-noise ratio. To identify bonding between nonprotonated carbons in 300C/SBA-15, dipolar-dephased double-quantum/single-quantum (DQ/SQ) spectra[28] were recorded. A ^{13}C-^{13}C 2D exchange spectrum with a long, 1 s mixing time was recorded to check the homogeneity of 300C/SBA-15. ^{13}C chemical shifts were predicted from structural models using the empirical ACD/NMR Predictors and converted into simulated spectra as described in the supporting information. Representative

structural models produce spectra with minimal differences from the quantitative experimental data, without and with dipolar dephasing.

2.3 Results and Discussion

2.3.1 Characterization of Carbon-Coated Supports

Table 2.1 shows the BET surface areas, pore volumes, and average pore diameters of the three different carbon materials before and after two separate hydrothermal treatments. The nitrogen physisorption isotherms are shown in Figures S2.1, S2.2, and S2.3 (see supporting information). Type IV isotherms were found for all of the carbon-coated SBA-15 materials, which indicated a mesoporous structure for all the materials. Nitrogen desorption occurred at higher P/P^0 after hydrothermal treatments as a result of some pore enlargement. The higher temperature carbon/SBA-15 materials lost some surface area after hydrothermal treatments, but not nearly as significantly as the carbon-free SBA-15, where the surface area of SBA-15 decreased from 740 $m^2\ g^{-1}$ to only 30 $m^2\ g^{-1}$ after hydrothermal treatment in water at 200 °C for 12 hours.[8] The hydrothermal treatment in our research at 170 °C is likely to have a similar detrimental effect for SBA-15. Besides, the hydrothermal treatment in this research was performed for 24 hours and repeated twice, which is a much harsher condition. As described below, ^{13}C NMR shows that 300C/SBA-15 and 400C/SBA-15 contained some unpyrolyzed glucose. 300C/SBA-15 had a small increase in surface area after the first hydrothermal treatment, possibly due to the surface roughness of the pore walls after treatment, which was likely caused by the dissolution of unpyrolyzed glucose. The partial loss of surface area in 400C/SBA-15 after the first hydrothermal treatment may have been caused both by the dissolution of a small amount of unpyrolyzed glucose and also partial leaching of the carbon overlayer, which could leave a portion of the surface pore walls of silica SBA-15 unprotected

and susceptible to hydrolytic attack, and by the loss of micropores (Table 2.1). 600C/SBA-15, pyrolyzed at 600 °C, had a more rigid carbon structure and thus showed relatively small changes in the micropore volume. The pore diameter increased and the pore size distribution broadened after hydrothermal treatment due to partial leaching of the carbon overlayer (Figure S2.4). However, if the carbon loading was increased such that the carbon overlayer thickness was increased, it might be possible to further improve the hydrothermal stability of the C/SBA-15 supports. Nevertheless, the focus of the current work was the interaction of the carbon overlayer with the Pd particles.

Table 2.1 Physical properties of 300C/SBA-15, 400C/SBA-15, and 600C/SBA-15 supports before and after hydrothermal treatments.

Sample name	Hydrothermal treatment	BET surface area (m^2/g)	Total pore volume (cm^3/g)	t-Plot micropore volume (cm^3/g)	Mesopore volume (cm^3/g)	BJH adsorption average pore diameter (nm)
300 C/SBA-15	fresh	361	0.492	0.032	0.460	6.27
	1st treatment	380	0.675	0.021	0.654	7.41
	2nd treatment	357	0.818	0.023	0.795	9.46
400 C/SBA-15	fresh	412	0.519	0.041	0.478	5.98
	1st treatment	362	0.651	0.020	0.631	7.63
	2nd treatment	319	0.751	0.022	0.729	9.44
600 C/SBA-15	fresh	305	0.388	0.024	0.364	5.72
	1st treatment	279	0.364	0.023	0.341	5.82
	2nd treatment	260	0.408	0.020	0.388	7.11

Elemental analysis was performed on carbon/SBA-15 (Figure 2.1). As the pyrolysis temperature increased, the weight percentage of both carbon and hydrogen decreased. For comparison, when hydrophilic SBA-15 was exposed to the atmosphere there were surface hydroxyl groups formed on the pore walls, leading to hydrogen release as water during the

analysis. Hence, the hydrogen content was higher for uncoated SBA-15 than that of the carbon overlayer on silica.

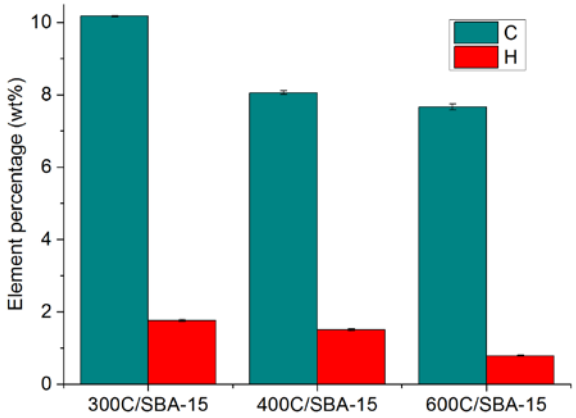

Figure 2.1 Elemental weight percentage of carbon and hydrogen for the 300C/SBA-15, 400C/SBA-15 and 600C/SBA-15.

Thermogravimetric analysis (TGA) in flowing UHP argon was used to study the mass loss of the carbon/SBA-15 materials as a function of temperature (Figure 2.2). During the 20 min of sample treatment in UHP argon at 150 °C to remove water, 300C/SBA-15 and 400C/SBA-15 lost up to 3% weight, which could be ascribed to water. For 600C/SBA-15 very little change in mass was observed during treatment at 150 °C, which confirmed the higher extent of hydrophobicity for 600C/SBA-15. Subsequently, during heating to 900 °C, 300C/SBA-15 lost 10.6% weight, while 400C/SBA-15 lost 6.2% and 600C/SBA-15 lost 2.8%. These results were consistent with the lower hydrogen and carbon content for the latter samples and were suggestive of the carbohydrate-derived carbon overlayer further condensing.

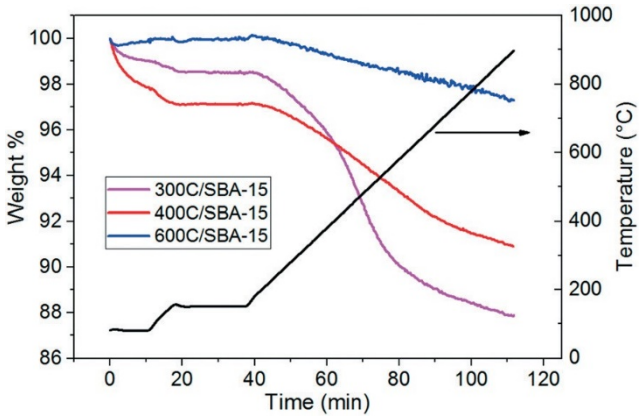

Figure 2.2 TGA results for the 300C/SBA-15, 400C/SBA-15 and 600C/SBA-15 from 80 to 900 °C.

X-ray photoelectron spectroscopy (XPS) was performed to analyze C1s and O1s on the surface of the carbon/SBA-15 supports. The spectra were calibrated using silicon at 103.4 eV. The O1s spectra are shown in the supporting information (Figure S2.5). The three spectra were similar, suggesting that the XPS determined oxygen content was the same for all of the carbon/SBA-15 materials. Unfortunately, XPS might not provide information about the oxygen functional groups in the carbon overlayer as XPS analysis will penetrate several nm and the carbon overlayer on SBA-15 would be expected to be closer to a monolayer (~ 0.22 nm). As such O1s signals were likely a convolution of the carbon overlayer with the underlying silica. Analyzing the oxygen content in the carbon overlayer by energy dispersive spectroscopy (EDS) would not be useful since the oxygen content would be similar for all the carbon/SBA-15 materials given that EDS is a bulk technique that would include the oxygen in SBA-15.

Table 2.2 Atom concentration of functional groups from XPS C1s spectra.

	sp^3 carbon	sp^2 carbon	C=**C**-O	C=O	COOH
300C/SBA-15	47.8%	18.3%	11.5%	14.3%	3.7%
400C/SBA-15	9.1%	65.3%	18.2%	0.0%	2.3%
600C/SBA-15	3.4%	73.5%	14.5%	0.0%	5.4%

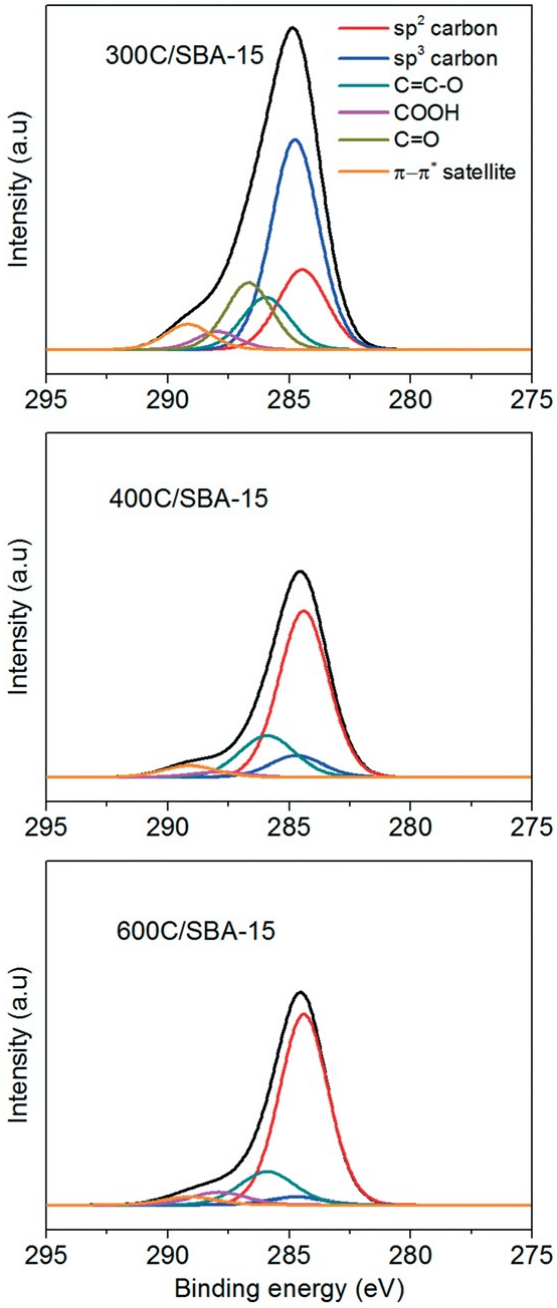

Figure 2.3 XPS C1s spectra of 300C/SBA-15, 400C/SBA-15 and 600C/SBA-15.

The C1s spectra were obtained and processed using the CasaXPS software. Aromatic carbon (sp^2 carbon) was assigned at 284.5 eV, aliphatic carbon (sp^3 carbon) at 284.8 eV, furanic (C=C-O) at 286.0 eV, carbonyl (C=O) at 286.7 eV, and carboxylic (COOH) at 288.0 eV, and the

π–π* satellite peak at 289.1 eV.[34] When analyzing just a single sample, the peaks could be fairly straightforwardly fit according to literature. However, when considering several samples having different oxygen contents, the deconvolution of the XPS C1s peaks became more difficult while keeping the same oxygen functional groups at the same positions. Moreover, the peak fitting will also depends on the resolution of the XPS instrument. Figure 2.3 is the XPS C1s spectra of carbon/SBA-15. As seen, the 300C/SBA-15 contained more oxygen functional groups, while the 400C/SBA-15 and 600C/SBA-15 spectra were similiar and contained relatively fewer oxygen groups. It has been shown that adventitious carbon contaminants from the atmosphere can also deposit on the sample surface, thus more carboxylic groups could be observed on the three carbon materials by XPS than by NMR.[35] The results from the deconvolution and quantification of the XPS spectra are given in Table 2.2. After depositing 5 wt% Pd on carbon/SBA-15, the Pd 3d spectrum of Pd 300C/SBA-15 showed that Pd was in the metallic state (Figure S2.6), with Pd $3d_{3/2}$ and Pd $3d_{5/2}$ peaks at 335.3 eV and 340.5 eV, respectively.

Raman spectroscopy measurements were performed on the carbon/SBA-15 samples to characterize the graphitic character of the carbon after pyrolysis. The Raman spectra of graphitic materials exhibited two characteristic bands: the G band (E_{2g}) at 1580 cm^{-1} and the D band (A_{1g}) at 1360 cm^{-1}. The intensity ratio I_D/I_G between the D and G bands has been used as a measure of defects in graphite-based materials with higher ratios characteristic of more defects.[36,37]

The Raman spectra are shown in Figure S2.7. The 600C/SBA-15 spectrum revealed a graphitic carbon content. The I_D/I_G ratio for 600C/SBA-15 was 0.67 ± 0.02, which revealed greater disorder than the graphite standard (0.19 ± 0.01). The Raman spectra in this research were less conclusive regarding the nature of the carbon in the 300C/SBA-15 and 400C/SBA-15 samples due to a high luminescence background that was at least an order of magnitude higher

than the background measured for the 600C/SBA-15 sample. The spectra of the starting material prior to pyrolysis, SBA-15 and glucose/SBA-15, showed a high luminescence signal intensity with the addition of glucose. The glucose/SBA-15 spectrum had low intensity peaks corresponding to glucose (1074, 1125 and 1358 cm^{-1}). While a small amount of unpyrolyzed glucose was found on 300 and 400C/SBA-15 by NMR (as discussed below), no glucose peaks were detected by Raman spectroscopy for any of the C/SBA-15 samples, possibly due to the high backgrounds.

2.3.2 NMR Spectra and Structural Models

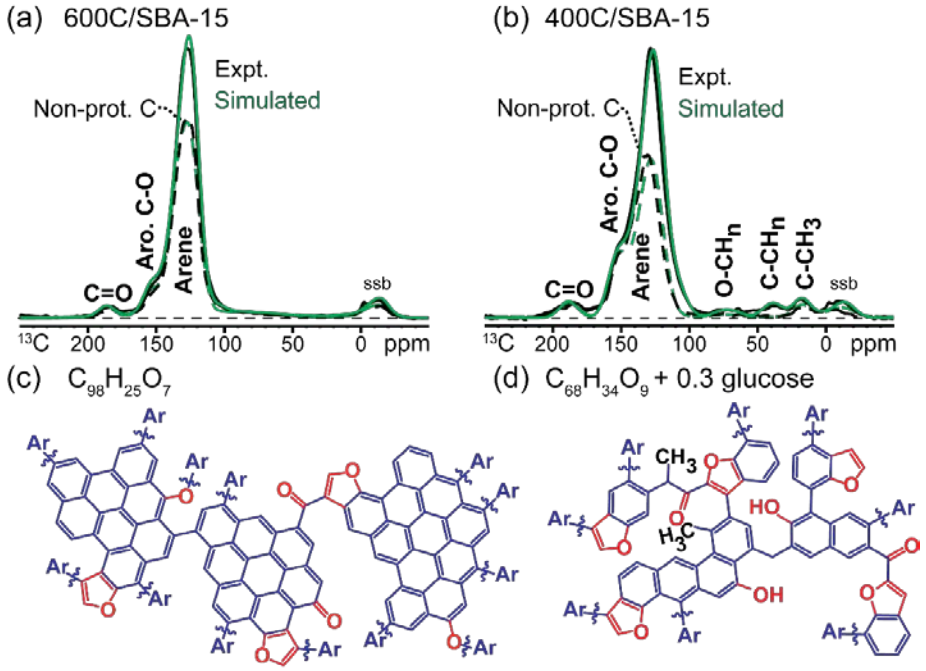

Figure 2.4. ^{13}C NMR spectra and structural models of 600C/SBA-15 and 400C/SBA-15. (a), (b) Quantitative spectra of all carbons (black solid lines) and of non-protonated and mobile groups (black dashed lines). (c), (d) Corresponding structural models that yield the simulated spectra shown by green lines in (a) and (b) (green solid lines: all carbons; green dashed lines: nonprotonated C and mobile groups). “ssb”: spinning side band. The small peak at -1 ppm is from the reference compound poly(dimethylsilane) in the nonconductive filler.

The compositions and molecular structures of the carbon overlayers on 600C/SBA-15, 400C/SBA-15, and 300C/SBA-15, and on 300C/SBA-15 hydrothermally treated with Pd were

studied by solid-state NMR. First, quantitative ^{13}C NMR spectra of all carbons and of nonprotonated (or mobile) C were recorded from each sample, which provided information on the carbon composition of each sample. The simplest spectrum was observed for 600C/SBA-15 (Figure 2.4a). It was dominated by the relatively narrow peak of aromatic carbons not substituted by heteroatoms, near 130 ppm. Integration showed that this material consisted of ~90% arene carbons, ~10% aromatic ketone and C-O, and no detectable alcoholic or aliphatic carbons (at < 90 ppm). The spectrum of nonprotonated carbons (dashed line) revealed that 73% of the arene carbons were not protonated, which indicated fused aromatic ring systems of moderate size. The spectrum of 400C/SBA-15 (Figure 2.4b) contained more alcoholic and aromatic C-O, resonating near 75 and 150 ppm, respectively; this material must have less extensive condensation of aromatic rings since only 60% of the arene carbons were not protonated. Based on these data and previous studies of moderate and high temperature char,[27,28] structural models were generated for the 600 and 400 °C samples from the quantitative 1D spectra. Figures 2.4c and d show these average structure models, with oxygen-containing groups highlighted in red and arenes in blue. The spectra simulated based on these model structures (green lines in Figures 2.4a and b) provided a good match to the experimental results.

The spectrum of 300C/SBA-15 showed strong signals of many different oxygen-containing functional groups. These included C=O, COO, aromatic C-O, and O-CH groups; their amounts are quantified in Table 2.3. Two-dimensional ^{13}C-^{13}C NMR with spectral editing, such as EXPANSE NMR (Figure 2.5b) and DQ/SQ NMR with dipolar dephasing (Figure S2.10a), helped for identifying the linkages between functional groups through cross peaks between the chemical shifts of neighboring carbons. Based on these data and knowledge from previous NMR studies of pyrolyzed ^{13}C-enriched glucose,[38] the structural model shown in Figure 2.5c was

generated, which produced simulated spectra in good agreement with the experimental ones (Figure 2.5a). The NMR analysis demonstrated that the carbon overlayer in 300C/SBA-15 had more oxygen-containing functional groups than the higher-temperature carbon overlayers, and consisted of more protonated and less fused rings, in agreement with previous analyses of pyrolyzed glucose[27,38]. The presence of small molecules such as glucose and acetic acid was attributed to strong adsorption by the mesoporous support and low pyrolysis temperature. The C–OH functionalities are not shown incorporated into the structural model of the carbon overlayer in Figure 2.5c because the 1 s ^{13}C–^{13}C exchange spectrum (Figure S2.8) demonstrates that the alcohol signal is mostly associated with spatially separated, only slightly oxidized glucose, which was also included in the simulation (see the supporting information for details).

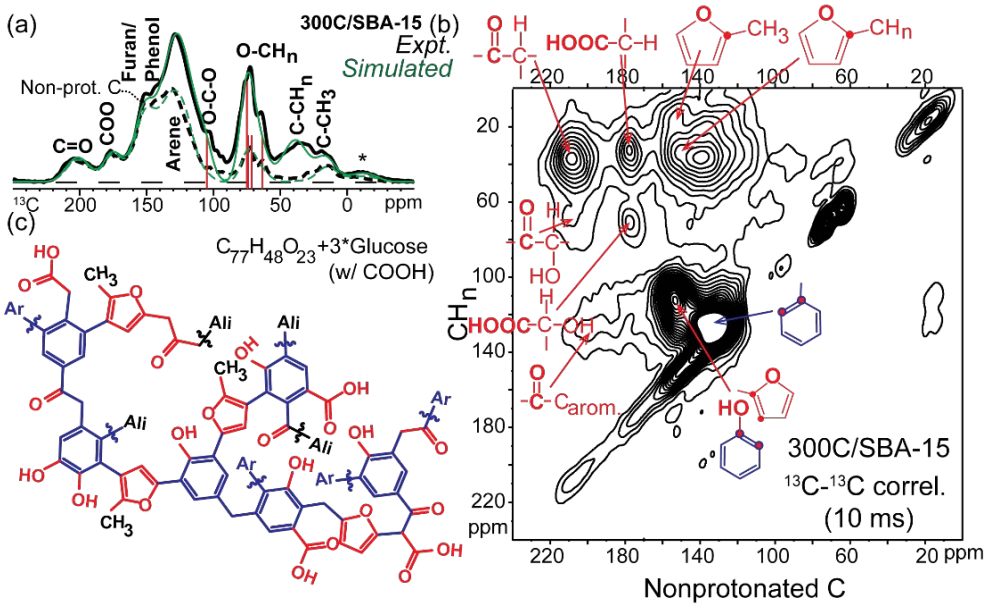

Figure 2.5. ^{13}C NMR spectra and structural model of 300C/SBA-15. (a) Quantitative spectra of all carbons (black solid lines) and of non-protonated and mobile groups (black dashed lines). (b) Two-dimensional EXPANSE spectrum with 10-ms spin exchange between protonated and nonprotonated carbons; structural assignments of major peaks are indicated in red and blue. (c) Corresponding structural model that gives the simulated spectra shown by green lines in (a) (green solid line: all carbons; green dashed line: nonprotonated C and mobile groups). “ssb”: spinning side band.

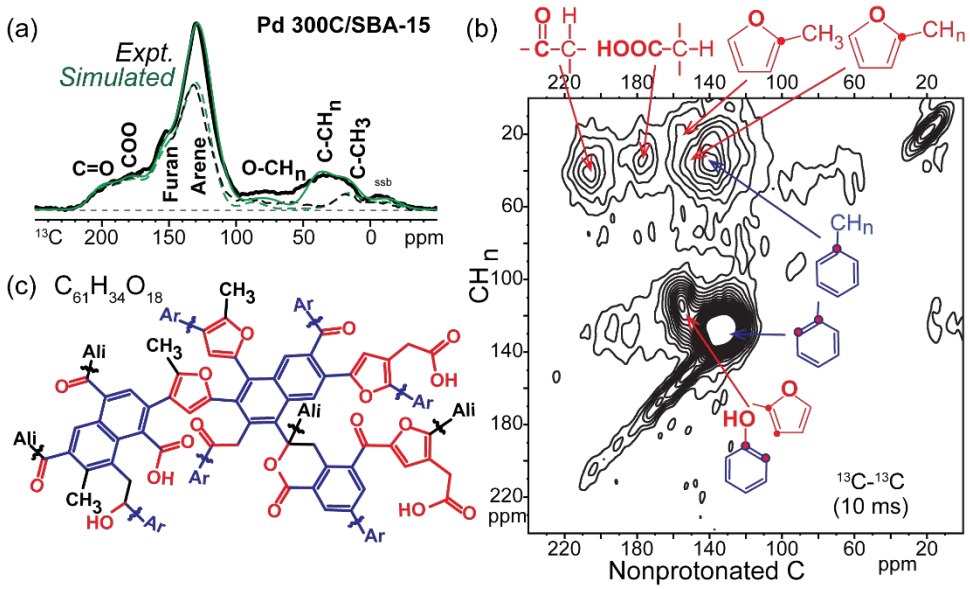

Figure 2.6. ^{13}C NMR spectra and structural models of Pd 300C/SBA-15 after two hydrothermal treatments. (a) Quantitative spectra of all carbons (black solid lines) and of non-protonated and mobile groups (black dashed lines). (b) EXPANSE spectrum with 10-ms spin exchange between protonated and nonprotonated carbons; assignments of major peaks are shown in red and blue. (c) Corresponding structural model that gives the simulated spectra shown by green lines in a) (green solid line: all carbons; green dashed line: nonprotonated C and mobile groups). "ssb": spinning side band.

The NMR structure in Figure 2.5c and the data in Tables 2.2 and 2.3 showed that 300C/SBA-15 was not highly graphitic, which explained the lack of detectable graphite peaks in the Raman spectrum of this sample. The XPS and NMR data in Tables 2.2 and 2.3 agreed in terms of their trends, such as the gradual loss of aliphatic and oxygen-containing functional groups with increasing pyrolysis temperature. However, the actual percentages in the two tables differed significantly. For example, the carbonyl group (C=O) was not observed on 400 and 600C/SBA-15 from XPS, while 4.2% and 3.4% C=O were quantified from NMR. Additionally, the amount of nonprotonated aromatic carbon can be calculated from NMR, which also served as an indicator of the graphitic extent of the carbon materials. Since the peaks in the NMR spectrum

were much better resolved than in XPS and could often be directly integrated, NMR characterization was used to compare the carbon surface chemistry.

Table 2.3. Atom concentration of functional groups from NMR peak integrals and structural models.

Sample	Aliphatic C[a]	C=**C**H[b]	C=**C**-C[c]	C=**C**-O[d]	C=O[e]	COOH[f]
300C/SBA-15	37.6±1.4%	14.7±0.5%	25.3±0.5%	14.9±0.4%	5.4±0.3%	4.3±0.3%
400C/SBA-15	8.2±0.3%	25.8±1.0%	44.4±2.0%	16.2±1.0%	4.2±0.3%	0.9±0.4%
600C/SBA-15	1.4±0.3%	21.4±1.0%	68.3±4.0%	7.9±0.4%	3.4±0.3%	0.7±0.4%
Pd 300C/SBA-15[h]	20.9±1.0%	15.6±0.8%	38.6±0.7%	14.1±1.0%	7.0±1.2%	7.2±0.6%

[a]: 5-100 ppm; [b]: ca. 100-143 ppm, full spectrum minus dipolar-dephased; [c]: ca. 100-143 ppm after dipolar dephasing; [d]: ca. 143-165 ppm; [e]: 185-220 ppm; [f]: 165-185 ppm; [h]: Pd 300C/SBA-15 was measured by NMR after two hydrothermal treatments.

2.3.3 Hydrothermal Stability

The Pd particle size was measured by CO chemisorption and by HAADF-STEM analysis. As shown in Table 2.4, the Pd particle sizes increased concomitantly with the pyrolysis temperature of the carbon/SBA-15. This trend could be seen both before and after two separate hydrothermal treatments. The better dispersion of Pd nanoparticles and reduction of Pd sintering for the Pd 300C/SBA-15 was consistent with the material containing more oxygen functional groups.[21,23] HAADF-STEM images (Figure 2.7) also showed that Pd sintering increased and dispersion decreased with an increase in pyrolysis temperature. There was some loss in the structural integrity of the carbon/SBA-15 support for all three Pd catalysts after hydrothermal treatment, but its extent was significantly less than for bare SBA-15 under hydrothermal conditions as the mesoporous structure of bare SBA-15 was destroyed with more than 96% decrease in surface area as shown in previous work.[8] Aqueous-phase furfural hydrogenation (Figure 2.8 and Table 2.4) was used as a probe reaction to test the activity of the catalyst since the catalyst has known efficacy in the reaction.[39] Furfural hydrogenation batch reactions were

performed to test the catalyst activity before and after hydrothermal treatments. ICP-OES analysis of the hydrothermal treatment solution showed negligible Pd leaching (less than 0.1%) into the solution for the fresh catalyst or after the first hydrothermal treatment. After the first hydrothermal treatment, modest increases in activity were seen for the Pd 300C/SBA-15 and Pd 400C/SBA-15 catalysts whereas a slight decrease was observed for Pd 600C/SBA-15. While the activity of Pd on silica was found to deactivate very rapidly with serious Pd particle sintering at 170 °C during aqueous-phase acetone hydrogenation for less than 10 hours,[13] Pd C/SBA-15 showed improved stability after two separate hydrothermal treatments at 170 °C for 24 hours as the SBA-15 structure was preserved and Pd sintering was reduced. The conversion increase for Pd 300C/SBA-15 and Pd 400C/SBA-15 might have been due to more accessible Pd active sites caused by enlarged pores through dissolution of unpyrolyzed glucose and partial leaching of the carbon overlayer in the lower temperature-synthesized carbon supported Pd catalysts during the first hydrothermal treatment. Weisz-Prater criterion analysis for the reaction system suggested that the fresh catalyst could have internal mass transfer limitations (see the supporting information for calculation).

Since the catalysts were stable after the first hydrothermal treatment, a second treatment was performed for another 24 h, followed by another furfural hydrogenation testing. In this case, the activity decreased for all the three Pd carbon/SBA-15 catalysts, although most extensively for the Pd 600C/SBA-15 catalyst. The Pd particles in the three catalysts sintered further after the second hydrothermal treatment and to a larger extent in Pd 600C/SBA-15. Using ICP-OES, 12.11% and 9.05% of the total Pd leached into the solution during the second hydrothermal treatment for Pd 300C/SBA-15 and Pd 400C/SBA-15, respectively. In contrast, only 0.55% leached for Pd 600C/SBA-15.

Table 2.4. Summary of characterization and conversion results for the fresh and hydrothermally treated Pd on C/SBA-15 catalysts.

Name		Average diameter[a] /nm	Dispersion[b] %	Particle diameter[c] /nm	Dispersion[c] %	Conversion %	Leached Pd percentage[d] %
5%Pd 300C/ SBA-15	Fresh	3.09	36.25	2.94	38.17	50.9±0.5	NA
	1st HT[e]	3.19	35.11	4.73	23.70	63.6±2.4	0.02
	2nd HT	3.93	28.50	6.51	17.20	44.4	12.11
5%Pd 400C/ SBA-15	Fresh	3.42	32.75	3.51	31.96	56.4±0.4	NA
	1st HT	3.51	31.91	5.22	21.46	60.8±1.6	0.01
	2nd HT	4.54	24.67	7.32	15.30	37.4	9.05
5%Pd 600C/ SBA-15	Fresh	3.76	29.79	4.07	27.52	59.4±1.6	NA
	1st HT	4.64	24.14	5.53	20.26	55.3±2.3	0.00
	2nd HT	6.95	16.12	12.00	9.34	24.1	0.55

[a]: Surface-weighted average diameter is obtained from STEM by using $\sum d^3/\sum d^2$. [b]: Dispersion of Pd particle is calculated from 1.12/d from STEM, calculation can be found in Suporting Information. [c]:Obtained from CO chemisorption [d]: Leached Pd is measured by ICP-OES in the solutions after hydrothermal treatments. [e]: HT stands for hydrothermal treatment at 170 °C for 24 h.

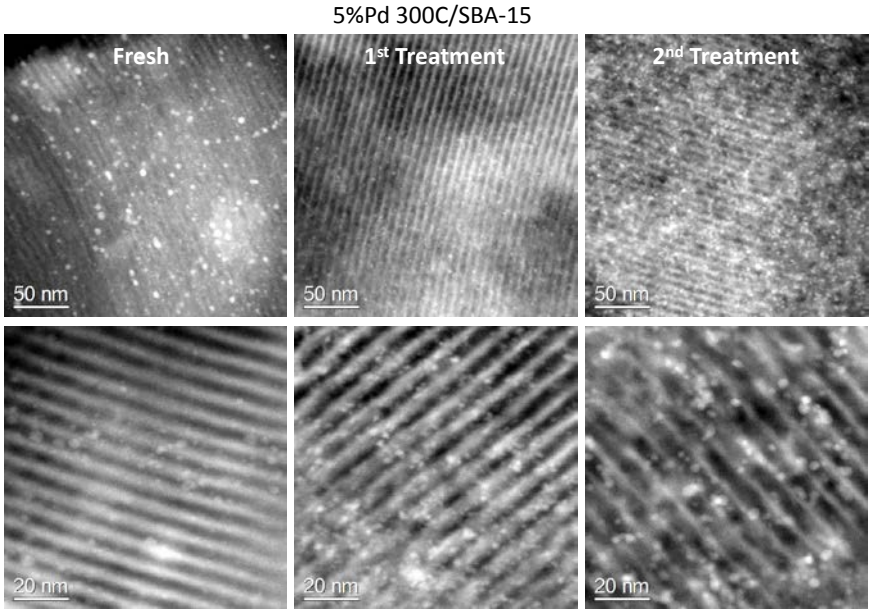

Figure 2.7. HAADF-STEM images at low magnification (top) and high magnification (bottom) of the three Pd on C/SBA-15 catalysts before and after hydrothermal treatments.

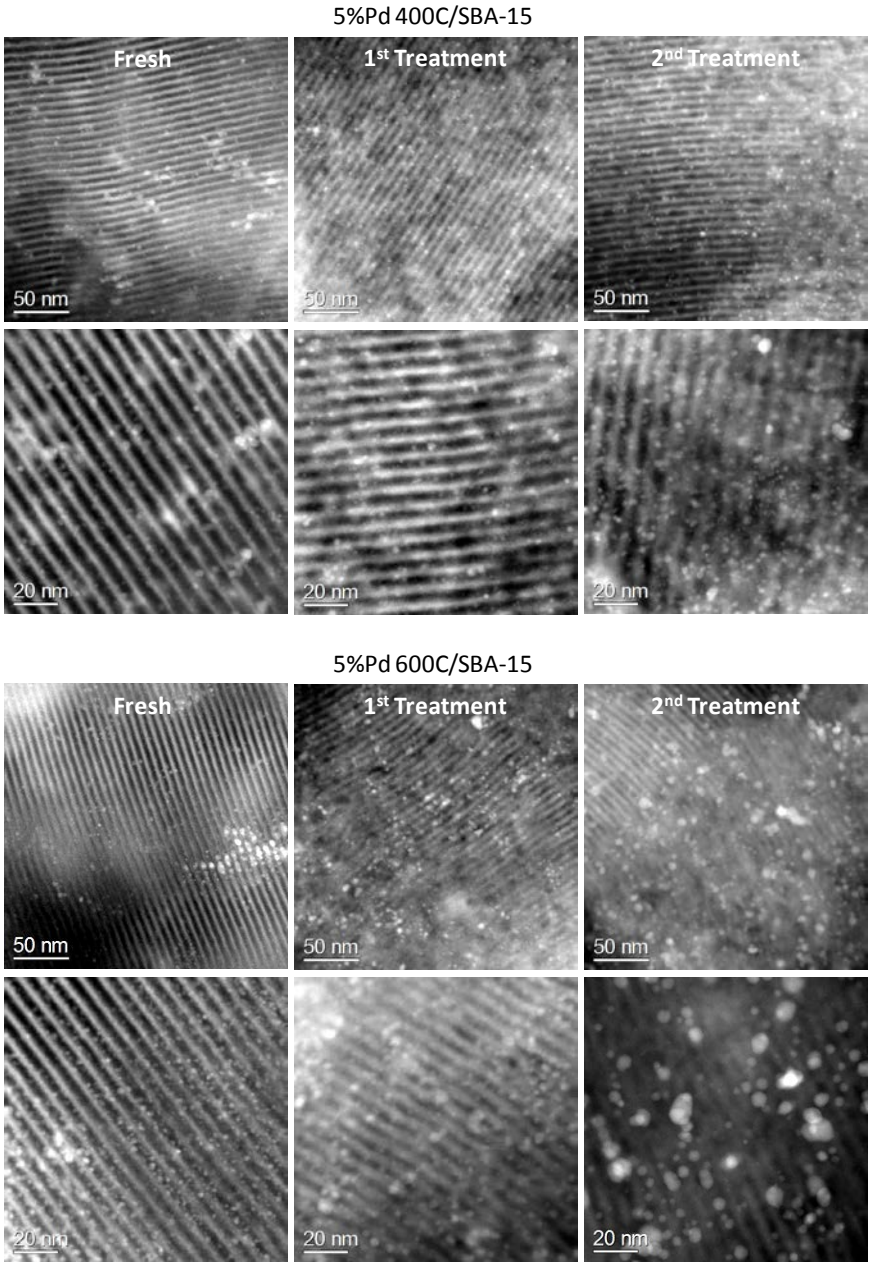

Figure 2.7. continued

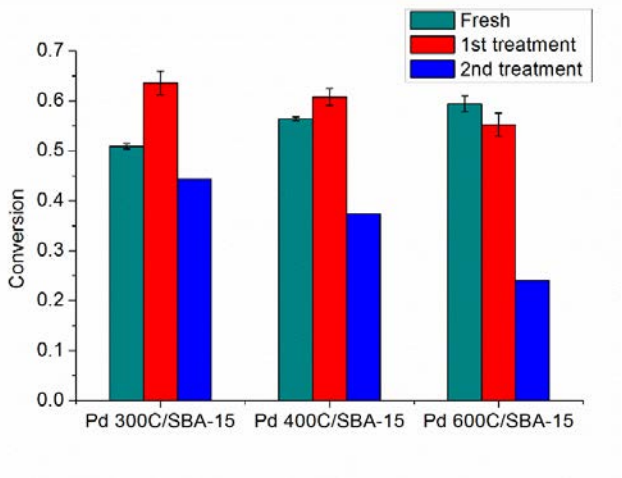

Figure 2.8. Furfural conversion by the Pd on C/SBA-15 catalysts before and after hydrothermal treatment. The reaction was performed at 80 °C and 760 psig H_2. Hydrothermal treatment was performed in aqueous solution at 170 °C for 24 h.

The surface average Pd particle diameters measured by CO chemisorption and by HAADF-STEM were similar for all of the fresh catalysts (Pd particle size distributions shown in Figure S2.11). After hydrothermal treatments, there was a discrepancy in that the Pd particle sizes derived from chemisorption were larger than the surface average particle sizes observed by STEM, which was due to decorative carbon from dissolved carbon species covering some Pd particles, as verified by HRTEM on Pd 300C/SBA-15 before and after hydrothermal treatments (Figures S2.12-S2.14). Decorative carbon was not observed on the fresh sample, resulting in similar particle sizes from CO chemisorption and STEM (Table 2.4). After the first and second hydrothermal treatments, some Pd particles were covered with decorative carbon (Figure S2.13c and d and S2.14d). The decorative carbon led to larger Pd particle sizes from CO chemisorption analysis. It is worth noting that as Pd particles sinter to bigger particles, the Pd particles may block the cylindrical pores of C/SBA-15, resulting in even less CO chemisorption. The biggest discrepancy was found in Pd 600C/SBA-15 after hydrothermal treatments as the Pd sintering was the most extreme among the materials.

To monitor carbon surface chemistry changes after hydrothermal treatments, a detailed NMR investigation was performed on Pd 300C/SBA-15 after two hydrothermal treatments. A comparison of the atom concentration of the functional groups before and after two hydrothermal treatments is presented in Table 2.3. The sharp carbohydrate peaks at 60-80 ppm observed for 300C/SBA-15 were lost (see Figure 2.6a), while the sample was still homogeneous on the 2-nm scale, as proven by the absence of a self-correlation diagonal ridge in the 2D exchange spectrum with 1-s spin diffusion time (Figure S2.9). The carbohydrate peaks appeared to result from unpyrolyzed glucose, which was then dissolved during the hydrothermal treatments. The reduction of peaks at around 105 ppm and 155 ppm indicated less furan and phenol groups after hydrothermal treatment. The decrease of oxygen-containing functional groups on the carbon surface was consistent with previous observations of structural changes in functionalized activated carbon under hydrothermal conditions.[40] The increase in the signal intensity around 190 ppm and signal loss at around 210 ppm for the sample indicated more extensive bonding of ketones to aromatic rings instead of aliphatic groups. The higher nonprotonated arene carbon fraction compared to the fresh material (66% vs. 59%) confirmed more fused rings being formed. The spectrum calculated from the average structural model shown in Figure 2.6a (green lines) reproduced most features in the experimental spectrum in Figure 2.6a (black lines). Compared with the model in Figure 2.5c of the structure before the addition of Pd and the following reduction in H_2 at 200 °C, the formation of bicyclic aromatic structures in Pd 300C/SBA-15 was noteworthy.

With decreasing oxygen functional groups including dissolution of unpyrolyzed glucose and decrease of furan and phenol groups, the Pd that was anchored to the oxygen-containing groups of the carbon overlayer leached into the solution, such as the case for Pd 300C/SBA-15

where a larger fraction of Pd was leached after the second hydrothermal treatment. Nonetheless, most of the oxygen-containing carbon overlayer was retained after hydrothermal treatments (with the molecular formula changing from $C_{77}H_{48}O_{23}$ to $C_{61}H_{34}O_{18}$, corresponding to C, H, and O ratios changing from 1:0.62:0.30 to 1:0.56:0.30, as determined by ^{13}C NMR), and, therefore, helped to retain the anchored Pd nanoparticles, thereby mitigating Pd sintering. For Pd 600C/SBA-15, the carbon overlayer was more hydrophobic after higher-temperature pyrolysis as it contained much fewer oxygen functional groups. Hence, only a small fraction of Pd was anchored to the functional groups, while the rest was less strongly bound to the carbon overlayer, making the Pd nanoparticles more prone to sintering under hydrothermal conditions. Even with higher Pd leaching, better stability was still maintained on lower-temperature pyrolyzed carbon after the second hydrothermal treatment due to suppressed Pd sintering. While negligible leaching occurred on Pd 600C/ SBA-15, serious sintering of Pd particles is more prominent, leading to less activity after the second hydrothermal treatment. Thus, how to create and maintain favorable surface functional groups to improve the dispersion and stability of Pd particles is the key to improving the hydrothermal stability of a catalyst for biomass conversions. Surface modification of carbon materials has been used including nitric acid and hydrogen peroxide treatment to create oxygen functional groups.[21,23,26] While activity and selectivity improvements were usually reported, few focused on how the surface oxygen functional groups affected the catalyst stability in water. Hydrogen peroxide treatment of carbon black was found to increase the dispersion of Pt particles.[21] The research showed that carbon black with more oxygen functional groups better stabilized Pt particles against sintering at 350 to 500 °C in a hydrogen atmosphere for a prolonged time.[21] In aqueous phase oxidation, hydrogen peroxide treated carbon nanotubes were found to increase the activity and selectivity of Au–Pd alloys.[23]

The stability of the catalyst was also studied during 6 repeated runs, but the reaction was performed with complete conversion and more characterization was needed to evaluate the changes in the catalyst.

2.4 Conclusions

Catalyst materials consisting of Pd supported on mesoporous carbon-coated SBA-15 (300, 400, and 600C/SBA-15) were synthesized and characterized systematically, in particular by ^{13}C NMR. A low-temperature pyrolyzed carbon overlayer, which had more oxygen-containing functional groups, helped to better disperse and stabilize the Pd nanoparticles compared to the high-temperature pyrolyzed carbon overlayer. The Pd nanoparticles in all three catalysts were found to sinter under hydrothermal conditions, but the Pd nanoparticles in Pd 600C/SBA-15 sintered to a much larger extent than those in the lower temperature carbon supported Pd catalysts. Furthermore, there is some decrease in oxygen functional groups including unpyrolyzed glucose, furan and phenol groups during the second hydrothermal treatment, as verified by ^{13}C NMR, causing more pronounced leaching of anchored Pd on lower temperature carbon supported Pd catalysts. However, the majority of oxygen functional groups were maintained on the lower-temperature pyrolyzed carbon, anchoring Pd particles against sintering. Overall, Pd on low temperature carbon with more oxygen functional groups showed better hydrothermal stability during hydrothermal treatments. Importantly, the utilization of NMR analysis provided for unprecedented characterization of the carbon layers. This detailed carbon surface analysis can help to guide future carbon material synthesis. More research is still needed to further improve the stability provided by functional groups in the carbon overlayer. For example, doping carbon with heteroatoms may further enhance the hydrothermal stability against leaching and sintering of Pd catalysts, and is part of future work.

2.5 Acknowledgement

This work is supported by the NSF Center for Biorenewable Chemicals (grant EEC-0813570). We would like to thank undergraduate Evie Goh for her help in running experiments, Dr. Dapeng Jing for XPS analysis, Mr. Stephen Veysey for TGA analysis, Dr. Yuan Xue for elemental analysis, and Dr. Patrick Johnston for ICP analysis. We would also like to thank Professor Jean-Philippe Tessonnier for helpful discussions.

2.6 References

1. Luterbacher, J. S.; Alonso, D. M.; Dumesic, J. A. *Green Chem* **2014,** *16*, 4816-4838.
2. Alonso, D. M.; Bond, J. Q.; Dumesic, J. A. *Green Chem* **2010,** *12*, 1493-1513.
3. Huber, G. W.; Iborra, S.; Corma, A. *Chem. Rev.* **2006,** *106*, 4044-4098.
4. Schwartz, T. J.; O'Neill, B. J.; Shanks, B. H.; Dumesic, J. A. *ACS Catal.* **2014,** *4*, 2060-2069.
5. Xiong, H.; Pham, H. N.; Datye, A. K. *Green Chem.* **2014,** *16*, 4627-4643.
6. Lange, J.-P. *Angew. Chem. Int. Ed.* **2015,** *54*, 13186-13197.
7. Sievers, C.; Noda, Y.; Qi, L.; Albuquerque, E. M.; Rioux, R. M.; Scott, S. L. *ACS Catal.* **2016,** *6*, 8286-8307.
8. Pham, H. N.; Anderson, A. E.; Johnson, R. L.; Schmidt-Rohr, K.; Datye, A. K. *Angew. Chem. Int. Ed.* **2012,** *51*, 13163-13167.
9. Gardner, D. W.; Huo, J.; Hoff, T. C.; Johnson, R. L.; Shanks, B. H.; Tessonnier, J.-P. *ACS Catal.* **2015,** *5*, 4418-4422.

10. Ravenelle, R. M.; Schussler, F.; D'Amico, A.; Danilina, N.; van Bokhoven, J. A.; Lercher, J. A.; Jones, C. W.; Sievers, C. *J. Phys. Chem. C* **2010,** *114*, 19582-19595.

11. Ravenelle, R. M.; Copeland, J. R.; Kim, W. G.; Crittenden, J. C.; Sievers, C. *ACS Catal.* **2011,** *1*, 552-561.

12. Pollock, R. A.; Gor, G. Y.; Walsh, B. R.; Fry, J.; Ghampson, I. T.; Melnichenko, Y. B.; Kaiser, H.; DeSisto, W. J.; Wheeler, M. C.; Frederick, B. G. *J. Phys. Chem. C* **2012,** *116*, 22802-22814.

13. Pham, H. N.; Anderson, A. E.; Johnson, R. L.; Schwartz, T. J.; O'Neill, B. J.; Duan, P.; Schmidt-Rohr, K.; Dumesic, J. A.; Datye, A. K. *ACS Catal.* **2015,** *5*, 4546-4555.

14. Xiong, H.; Schwartz, T. J.; Andersen, N. I.; Dumesic, J. A.; Datye, A. K. *Angew. Chem. Int. Ed.* **2015,** *54*, 7939-7943.

15. O'Neill, B. J.; Jackson, D. H. K.; Crisci, A. J.; Farberow, C. A.; Shi, F.; Alba-Rubio, A. C.; Lu, J.; Dietrich, P. J.; Gu, X.; Marshall, C. L.; Stair, P. C.; Elam, J. W.; Miller, J. T.; Ribeiro, F. H.; Voyles, P. M.; Greeley, J.; Mavrikakis, M.; Scott, S. L.; Kuech, T. F.; Dumesic, J. A. *Angew. Chem. Int. Ed.* **2013,** *52*, 13808-13812.

16. Mayanovic, R. A.; Yan, H.; Brandt, A. D.; Wang, Z.; Mandal, M.; Landskron, K.; Bassett, W. A. *Microporous and Mesoporous Mater.* **2014,** *195*, 161-166.

17. Ketchie, W. C.; Maris, E. P.; Davis, R. J. *Chem. Mater.* **2007,** *19*, 3406-3411.

18. Osada, M.; Sato, O.; Arai, K.; Shirai, M. *Energy Fuels* **2006,** *20*, 2337-2343.

19. Vleeming, J. H.; Kuster, B. F. M.; Marin, G. B.; Oudet, F.; Courtine, P. *J. Catal.* **1997,** *166*, 148-159.

20. Toebes, M. L.; Prinsloo, F. F.; Bitter, J. H.; van Dillen, A. J.; de Jong, K. P. *J. Catal.* **2003,** *214*, 78-87.

21. Pradoburguete, C.; Linaressolano, A.; Rodriguezreinoso, F.; Delecea, C. S. *J. Catal.* **1989,** *115*, 98-106.

22. Solhy, A.; Machado, B. F.; Beausoleil, J.; Kihn, Y.; Goncalves, F.; Pereira, M. F. R.; Orfao, J. J. M.; Figueiredo, J. L.; Faria, J. L.; Serp, P. *Carbon* **2008,** *46*, 1194-1207.

23. Wan, X.; Zhou, C.; Chen, J.; Deng, W.; Zhang, Q.; Yang, Y.; Wang, Y. *ACS Catal.* **2014,** *4*, 2175-2185.

24. H.P.Boehm. *Adv. Catal.* **1966**, *16*,179-274.

25. Figueiredo, J. L.; Pereira, M. F. R. *Catal. Today* **2010,** *150*, 2-7.

26. Figueiredo, J. L.; Pereira, M. F. R.; Freitas, M. M. A.; Orfao, J. J. M. *Carbon* **1999,** *37*, 1379-1389.

27. Anderson, J. M.; Johnson, R. L.; Schmidt-Rohr, K.; Shanks, B. H. *Carbon* **2014,** *74*, 333-345.

28. Johnson, R. L.; Anderson, J. M.; Shanks, B. H.; Fang, X.; Hong, M.; Schmidt-Rohr, K. *J. Magn. Reson.* **2013,** *234*, 112-124.

29. Baccile, N.; Laurent, G.; Babonneau, F.; Fayon, F.; Titirici, M.-M.; Antonietti, M. *J. Phys. Chem. C* **2009,** *113*, 9644-9654.

30. Zhao, D. Y.; Feng, J. L.; Huo, Q. S.; Melosh, N.; Fredrickson, G. H.; Chmelka, B. F.; Stucky, G. D. *Science* **1998,** *279*, 548-552.

31. Canton, P.; Fagherazzi, G.; Battagliarin, M.; Menegazzo, F.; Pinna, F.; Pernicone, N. *Langmuir* **2002,** *18*, 6530-6535.

32. Fagherazzi, G.; Canton, P.; Riello, P.; Pernicone, N.; Pinna, F.; Battagliarin, A. *Langmuir* **2000,** *16*, 4539-4546.

33. Mao, J. D.; Schmidt-Rohr, K. *Environ. Sci. Technol.* **2004,** *38*, 2680-2684.

34. Reiche, S.; Blume, R.; Zhao, X. C.; Su, D.; Kunkes, E.; Behrens, M.; Schloegl, R. *Carbon* **2014,** *77*, 175-183.

35. Barr, T. L.; Seal, S. *J. Vac. Sci. Technol., A* **1995,** *13*, 1239-1246.

36. Nakamizo, M.; Kammereck, R.; Walker, P. L. *Carbon* **1974,** *12*, 259-267.

37. Pimenta, M. A.; Dresselhaus, G.; Dresselhaus, M. S.; Cancado, L. G.; Jorio, A.; Saito, R. *Phys. Chem. Chem. Phys.* **2007,** *9*, 1276-1291.

38. Franklin, R. E. *Nature* **1956,** *177*, 239-239.

39. Lee, J.; Xu, Y.; Huber, G. W. *Appl. Catal., B* **2013,** *140*, 98-107.

40. Van Pelt, A. H.; Simakova, O. A.; Schimming, S. M.; Ewbank, J. L.; Foo, G. S.; Pidko, E. A.; Hensen, E. J. M.; Sievers, C. *Carbon* **2014,** *77*, 143-154.

2.7 Supporting Information

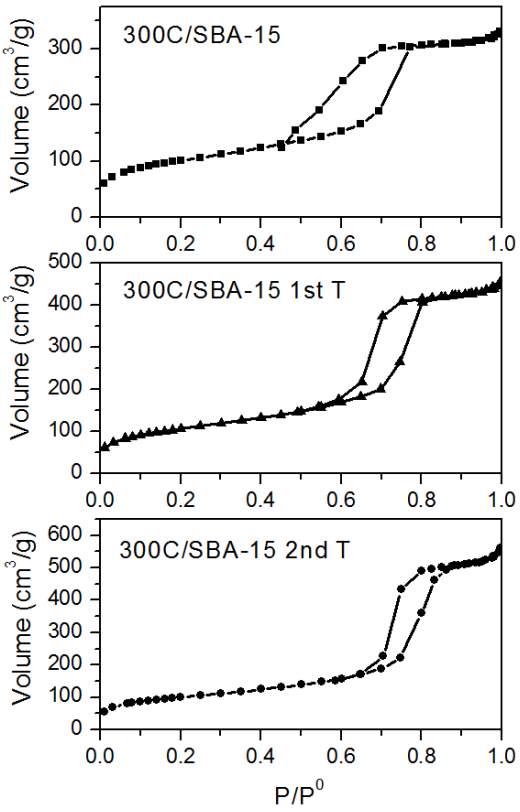

Figure S2.1. Nitrogen isotherms of 300C/SBA-15 before and after hydrothermal treatment (T stands for hydrothermal treatments).

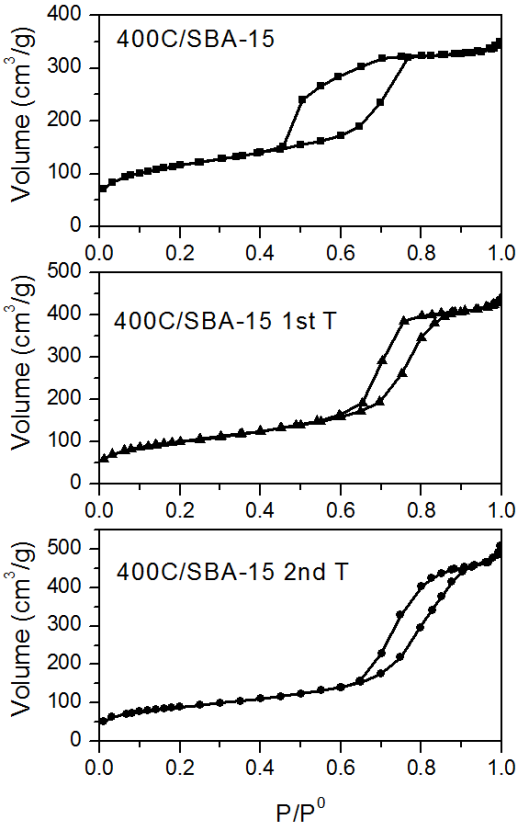

Figure S2.2. Nitrogen isotherms of 400C/SBA-15 before and after hydrothermal treatment.

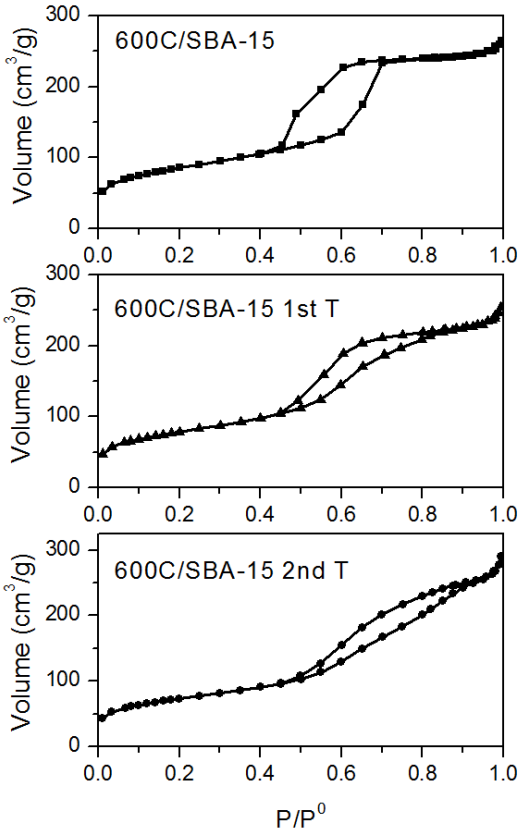

Figure S2.3. Nitrogen isotherms of 600C/SBA-15 before and after hydrothermal treatment.

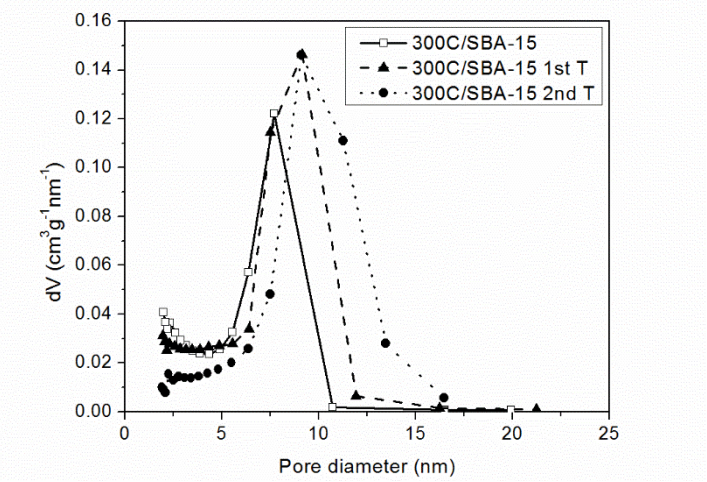

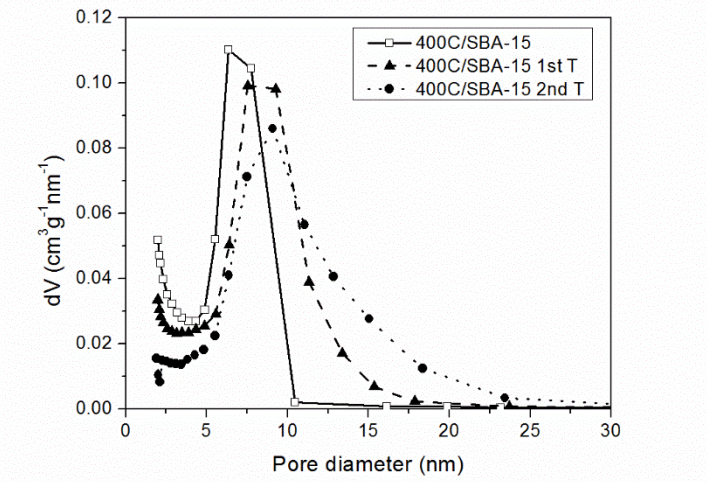

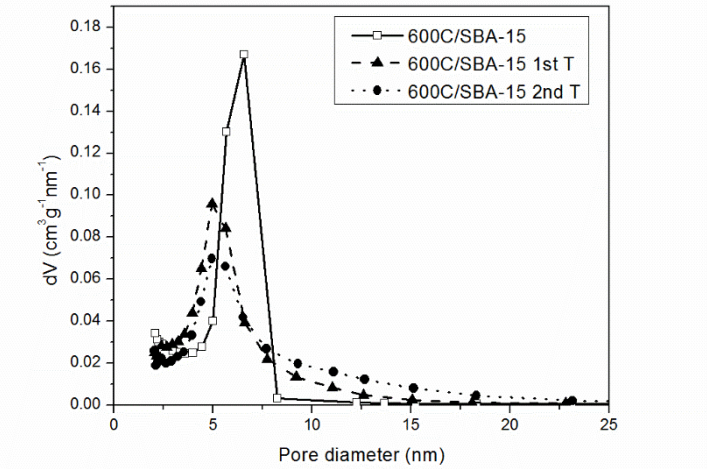

Figure S2.4. Pore size distribution of Pd 300, 400, 600C/SBA15 before and after hydrothermal treatment.

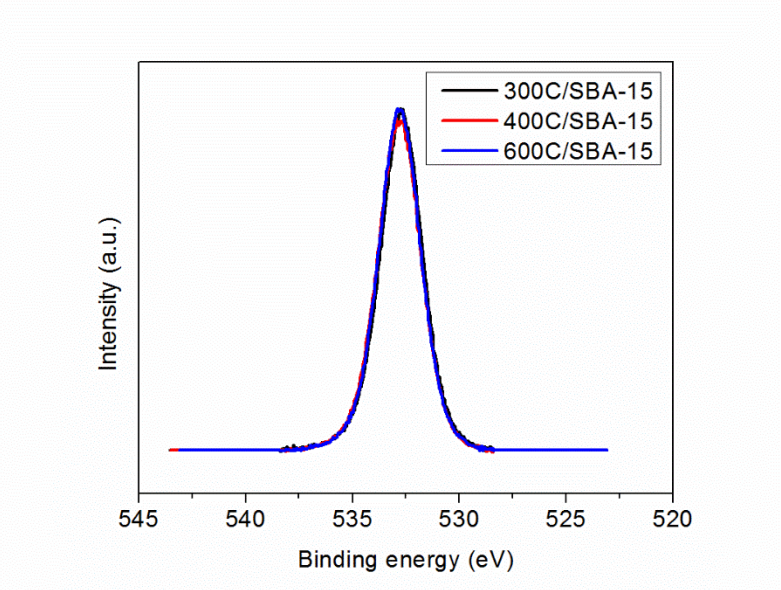

Figure S2.5. XPS O1s spectra of 300C/SBA-15, 400C/SBA-15 and 600C/SBA-15

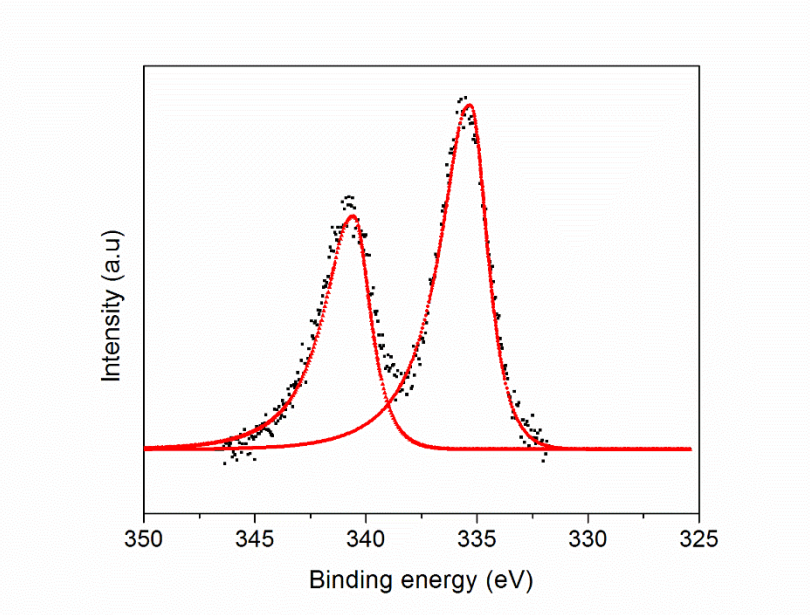

Figure S2.6. XPS Pd 3d spectrum of 5%Pd 300C/SBA-15.

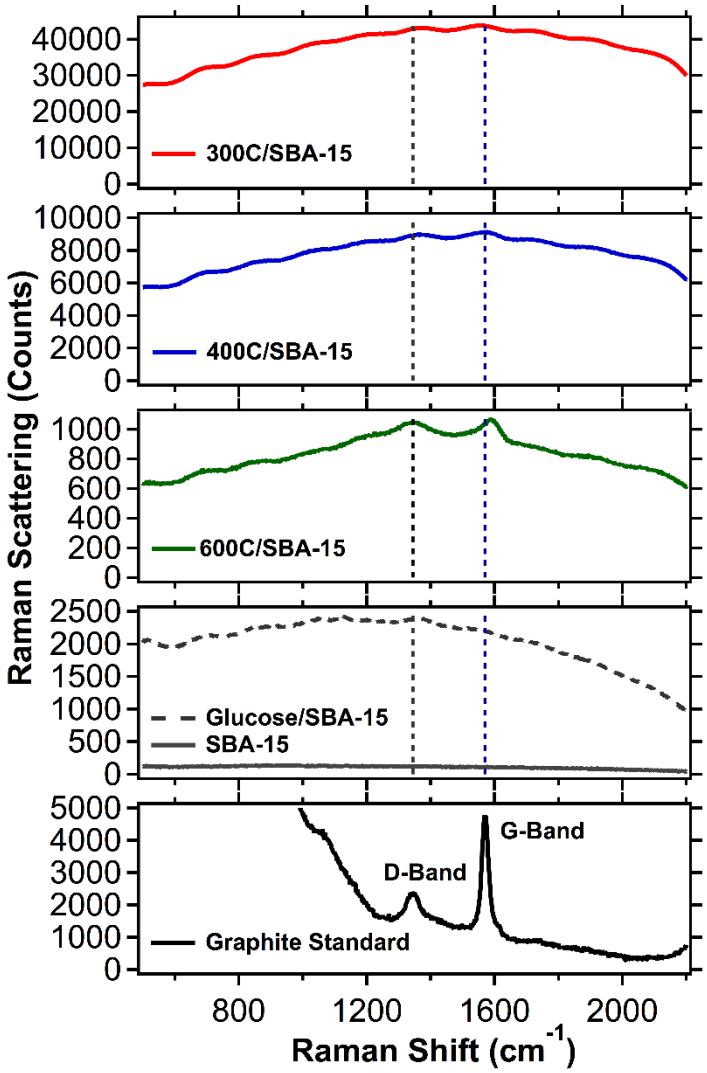

Figure S2.7. Raman spectra of graphite standard, SBA-15, Glucose-SBA-15, 300C/SBA-15, 400C/SBA-15 and 600C/SBA-15.

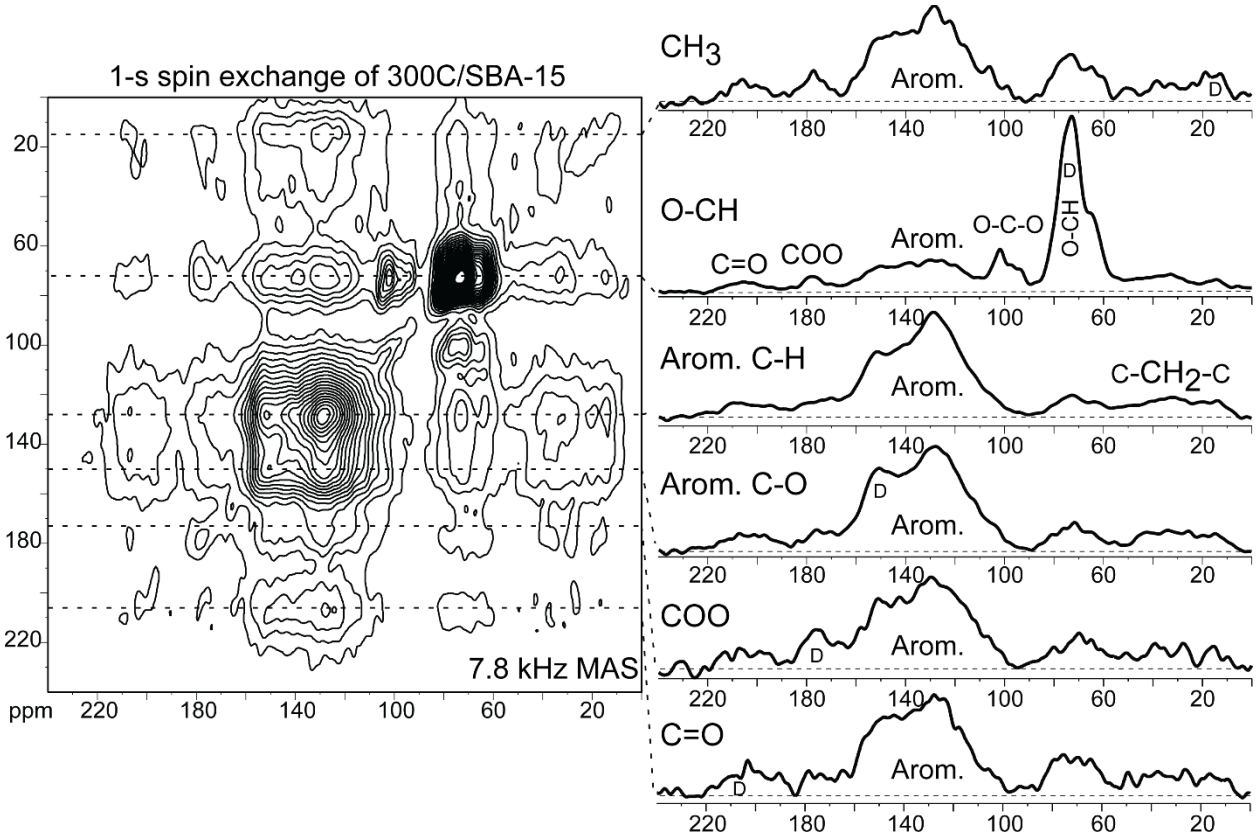

Figure S2.8. Two-dimensional ^{13}C-^{13}C NMR spectrum of 300C/SBA-15 with 1-s spin exchange, measured at 7.8 kHz MAS with TOSS-deTOSS around the evolution time, and total suppression of spinning sidebands (TOSS) before detection. The horizontal cross sections corresponding to magnetization originating from various different functional groups are shown on the right. Most cross sections have the same spectral pattern, indicating equilibration of magnetization over all types of functional groups, except for the OCH cross section, which shows more pronounced cross peaks typically observed within a sugar ring.

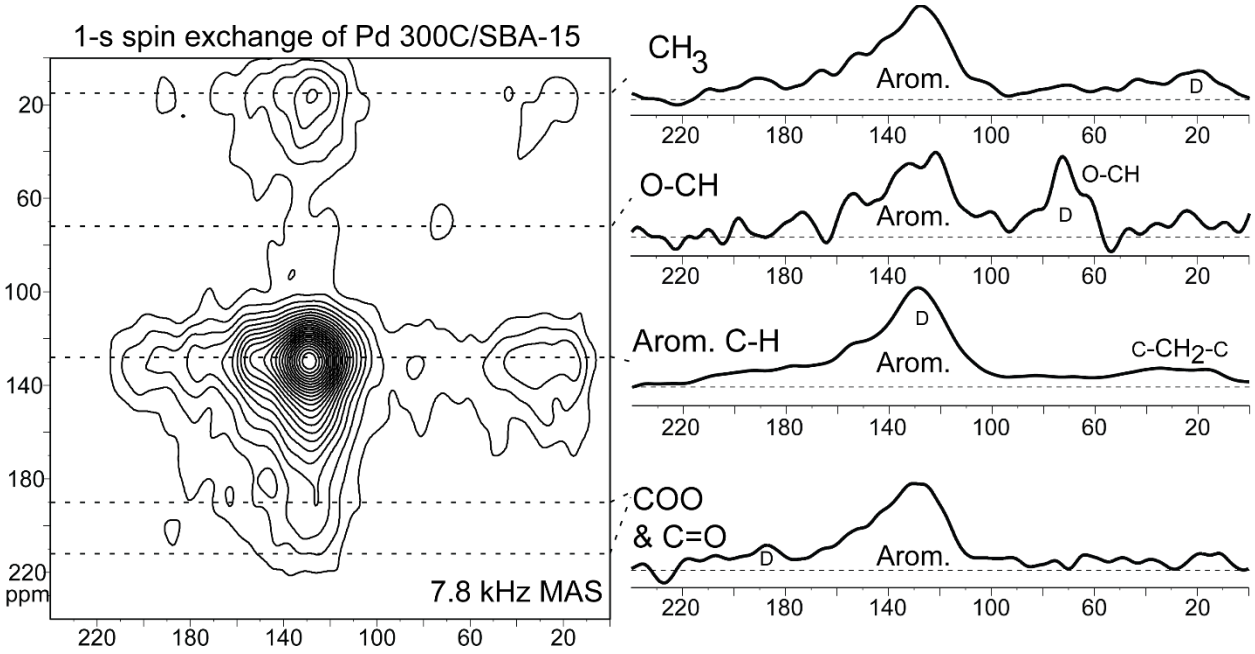

Figure S2.9. 1-s ^{13}C-^{13}C spin exchange NMR spectrum of Pd 300C/SBA-15 with conditions as described in the preceding figure caption. The horizontal cross sections corresponding to magnetization originating from four different functional groups are shown on the right. Residual diagonal peaks are labeled by "D".

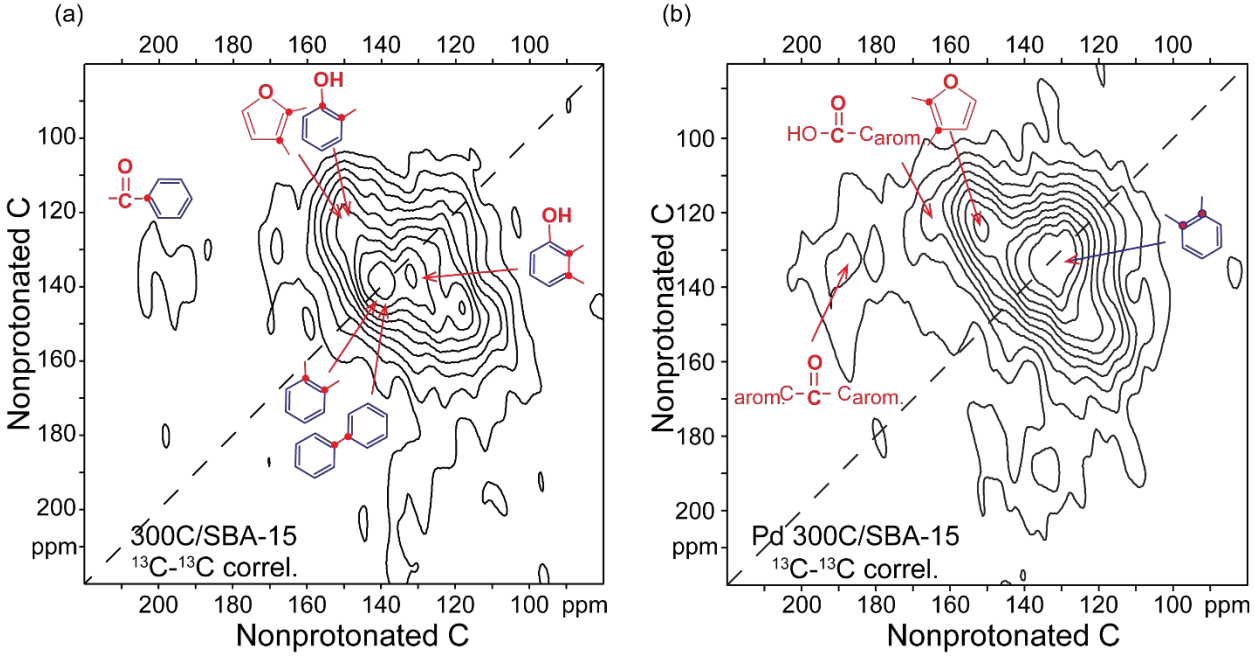

Figure S2.10. 2D ^{13}C-^{13}C NMR spectra of (a) 300C/SBA-15 and (b) Pd 300C/SBA-15. These dipolar-dephased double-quantum/single-quantum correlation spectra (DQ/SQ spectra, sheared along the vertical dimension) show only correlations between directly bonded nonprotonated carbons. Some peak assignments are indicated in red and blue.

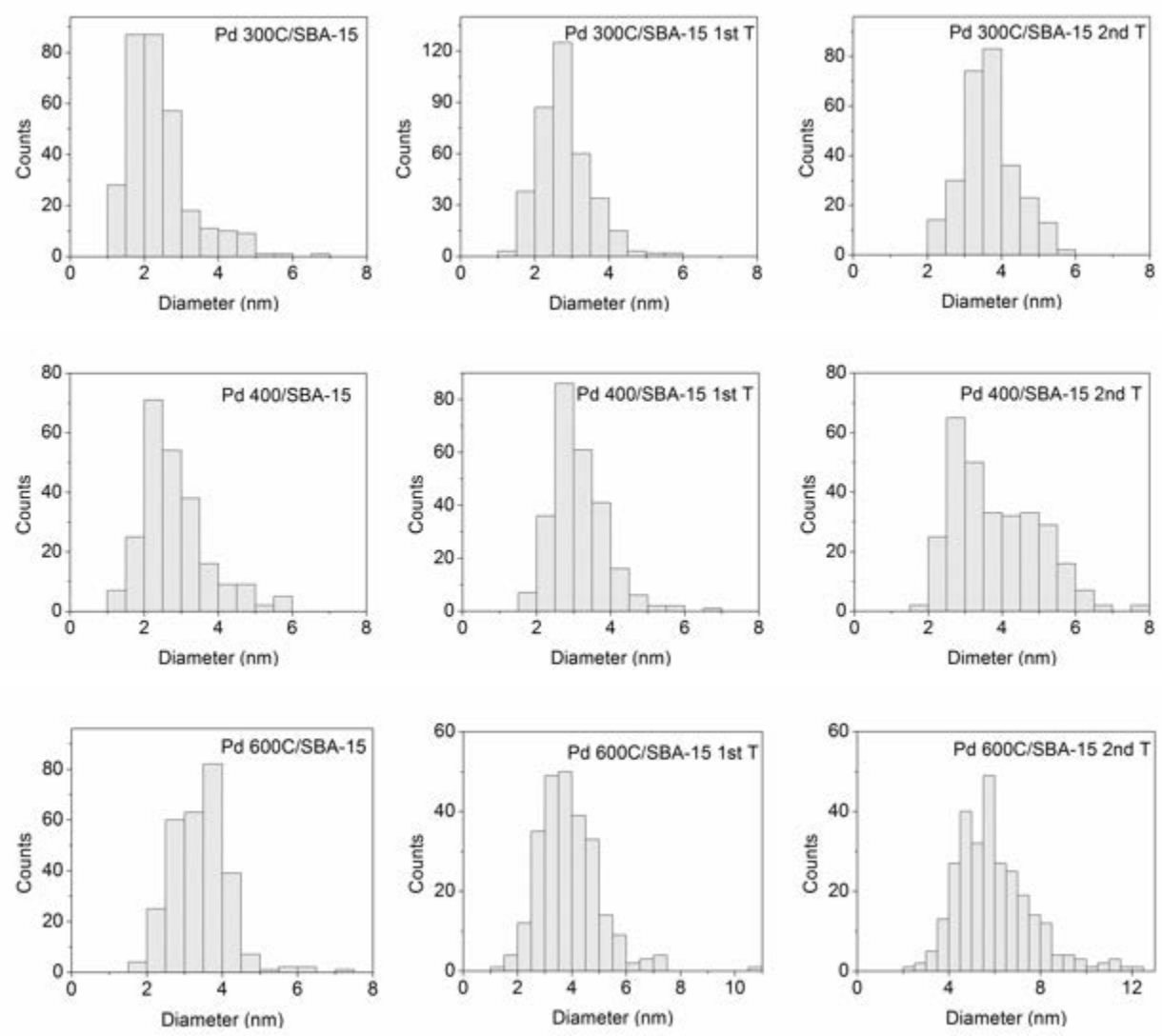

Figure S2.11. Particle size distribution of Pd 300C/SBA-15, Pd 400C/SBA-15, and Pd600C/SBA15 before and after two hydrothermal treatments. The Pd particle sizes were measured from HAADF-STEM images.

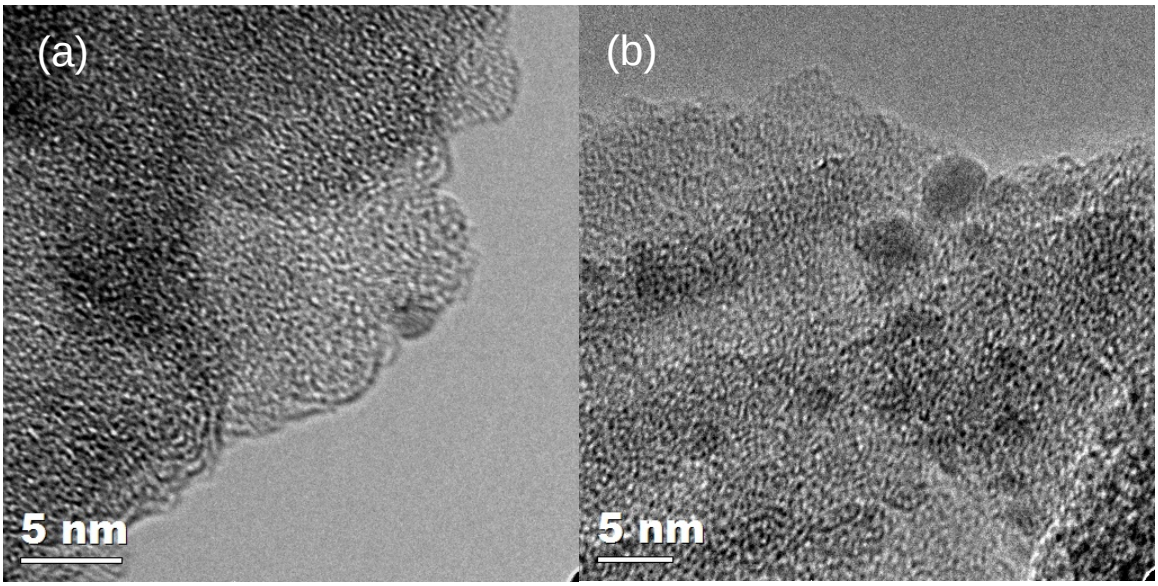

Figure S2.12. HRTEM images of fresh Pd 300C/SBA-15.

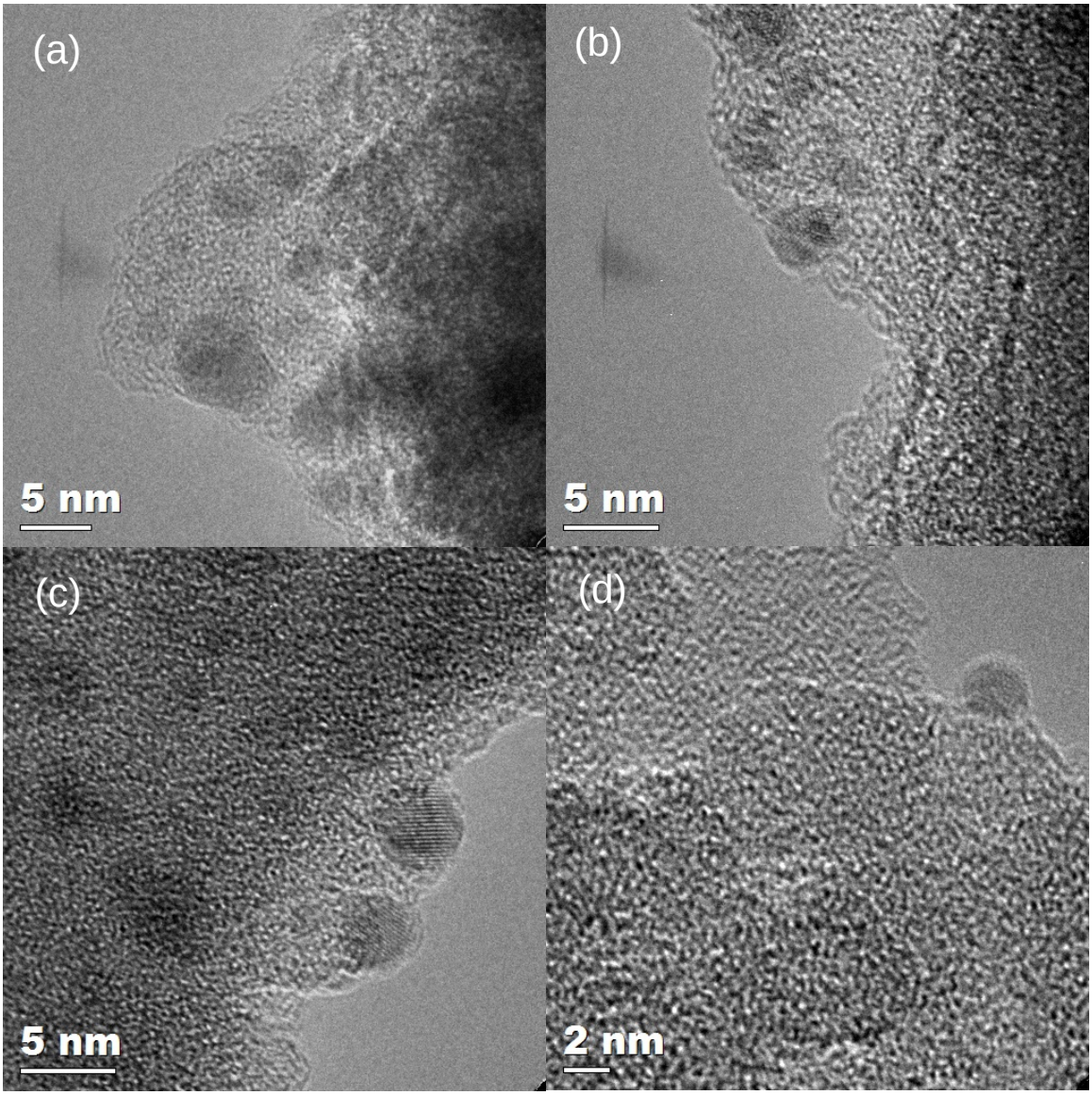

Figure S2.13. HRTEM images of Pd 300C/SBA-15 after first hydrothermal treatment.

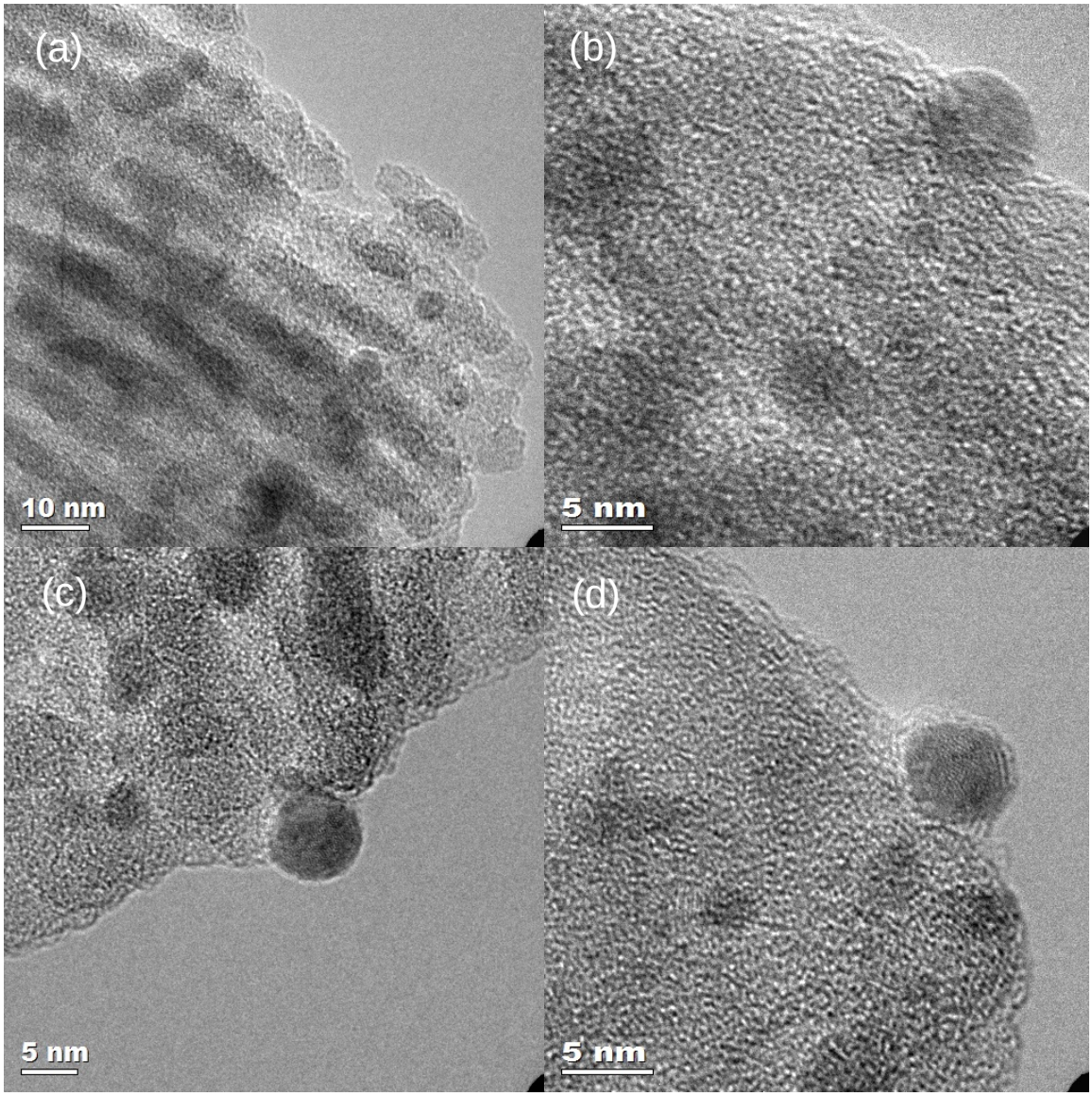

Figure S2.14. HRTEM images of Pd 300C/SBA-15 after second hydrothermal treatment.

Calculation for dispersion of Pd particles

The calculation for Pd particle dispersion is based on the equation below.[1]

$$\text{Dispersion} = \frac{6M_w}{S_a \cdot d \cdot \rho \cdot N_{AV}}$$

In the equation, $M_w$is the molecular weight of Pd (106.4 g/mol); S_a is the cross sectional area of Pd atom (0.0787 nm^2); ρ is the density of Pd (12.02 g/cm^3); N_{AV} is the Avogadro's number (6.022×10^{23}); d is the surface-averaged diameter of Pd particles from STEM analysis (unit is nm). The cross sectional area of Pd atom and density value are from Micrometrics ASAP manual.[2] Putting the values generate the equation below.

$$\text{Dispersion} = \frac{1.12}{d}$$

The dispersion from CO chemisorption is calculated in the same manner.

Calculation of Weisz-Prater parameter

The Weisz-Prater parameter was used to estimate internal mass diffusion limitations using equation below

$$\Phi_i = \frac{r^{eff} \cdot r_p^2}{c_{i,s} \cdot D_{i,mix}^{eff}} < 0.3$$

Where Φ_i is the dimensionless Weisz-Prater parameter; r^{eff} is the effective rate per volume of catalyst (mol s^{-1} m^{-3}); r_p is the radium of the catalyst particle (m); $c_{i,s}$ is the concentration of reactant i at the surface of the particle (mol/m^3); and $D_{i,mix}^{eff}$ is the effective diffusivity of i in the mixture (m^2 s^{-1}). When Φ_i is less than 0.3, it is safe to ensure absence of internal mass diffusion limitations.[3]

Assuming the catalyst density is the same with carbon black XC72R as 1.7 g/cm^3 and catalyst volume is 0.6 cm^3/g. r^{eff} is calculated as 589 mol s^{-1} m^{-3}. r_p is estimated as 4 μm, same as activated carbon.[4]

Diffusion coefficient of furfural and hydrogen gas in water at 80 °C is obtained as 3.361×10^{-9} m^2/s and 1.408×10^{-8} m^2/s.[5] The concentration of furfural is 0.106 M. Dissolved H_2 concentration is assumed to be the same at 100°C in water at 760 psig pressure as 0.044 M.[6]

$D_{i,\mathrm{mix}}^{\mathrm{eff}} = D_{i,\mathrm{mix}} \cdot \frac{\varepsilon}{\tau}$ is used for effective diffusivity calculation of porous material. Where ε is the catalyst porosity, τ is the tortuosity. ε is assumed to be 0.9 and a value of 15 is used for τ. $D_{F,mix}^{eff}$ of furfural is calculated as 2.02×10^{-10} m^2/s. $D_{H,mix}^{eff}$ of H_2 is calculated as 8.4×10^{-10} m^2/s.

Putting the values together, Φ_F of furfural is calculated as 0.44, and Φ_H of H_2 is calculated as 0.25, both of which are near 0.3, suggesting possible internal mass transfer limitations.

Generating structural models based on quantitative and 2D ^{13}C NMR spectra

Since the quantitative 1D spectra of 400C/SBA-15 and 600C/SBA-15 showed similar characteristics as previously observed for moderate and high temperature chars,[7, 8] structural models with analogous compositions were used as the starting point. ^{13}C chemical shifts were predicted using the ACD/NMR predictor and converted into spectra with peak broadening of 15- 17 ppm full width at half maximum. Spectra after dipolar dephasing were simulated by removing signals of CH and CH_2 groups, and scaling CH_3 signals by 0.57. Two spinning sidebands of 5% relative intensity each were included for the aromatic-carbon signals. The ratios of functional groups were fine-tuned to match the experimental quantitative 1D spectra, while making few changes to the connections between functional groups. For 300C/SBA-15 and Pd 300C/SBA-15, connections between functional groups identified in 2D EXPANSE and DQ/SQ spectra (Figure 2.5b, 2.6b, and S2.10) were included in the structural models. The simulated structure was converted into a representative repeat unit by taking out some functional groups at the edges, and leaving out their signals. To be general, functional groups were usually taken out in pairs. For example, if a furan connected to an aliphatic chain is removed, then another aliphatic chain connected to a

furan is taken out of the structure. In the end, a model with spectra of minimum difference (root mean square deviation) from the experimental spectra was chosen as representative.

The spectra of 300C/SBA-15 showed sharp carbohydrate peaks at 60-105 ppm, which matched well with the resonance positions of glucose (red vertical lines in Figure 2.5a). These carbons had weak dipolar couplings to ^{1}H, since they survived after dipolar dephasing (dashed-line spectrum), indicating that these carbohydrates were highly mobile. Whether they were segregated from the pyrolyzed carbons was determined by two-dimensional ^{13}C-^{13}C exchange NMR with a long, 1-s mixing time (Figure S2.8). While significant off-diagonal intensity was observed for all carbons, the O-CH cross section showed that the carbohydrates did not equilibrate their magnetization with the rest of the carbons, indicating separation on the scale of a few nanometers. Thus, the alcohol signal was mostly associated with only partially oxidized glucose somewhat separated from the rest of the carbon film. While the C-OH functionalities were not explicitly represented in our structural model in Figure 2.5c, they were included in the simulation as roughly three equivalents of glucose, with COOH groups instead of CH_2OH.

References

1. C. H. Bartholomew and R. J. Farrauto, *Fundamentals of Industrial Catalytic Processes, 2nd Edition*, 2006.
2. *Micromeritics AutoChem 2920 Automated Catalyst Characterization System Operator's Manual*, V4.00 edn., 2009.
3. S. Mukherjee and M. A. Vannice, *Journal of Catalysis*, 2006, **243**, 108-130.
4. J. H. Xie, B. Huang, K. H. Yin, H. N. Pham, R. R. Unocic, A. K. Datye and R. J. Davis, *ACS Catal.*, 2016, **6**, 4206-4217.

5. C. L. Yaws, *Yaws handbook of properties of the chemical elements*, Knovel, Norwich, N.Y., 2011.

6. E. F. Stephan, N. S. Hatfield, R. S. Peoples and H. A. H. Pray, *The solubility of gases in water and in aqueous uranyl salt solutionsat elevated temperatures and pressures*, Battelle Memorial Institute, Columbus, Ohio, 1956.

7. R. L. Johnson, J. M. Anderson, B. H. Shanks, X. Fang, M. Hong and K. Schmidt-Rohr, *J. Magn. Reson.*, 2013, **234**, 112-124.

8. J. M. Anderson, R. L. Johnson, K. Schmidt-Rohr and B. H. Shanks, *Carbon*, 2014, **74**, 333-345.

CHAPTER 3. IMPROVED HYDROTHERMAL STABILITY OF PD NANOPARTICLES ON NITROGEN-DOPED CARBON SUPPORTS

A paper published on Catalysis Science & Technology

Jiajie Huo,[ab] Pu Duan,[bc] Hien N. Pham,[bd] Yee Jher Chan,[a] Abhaya K. Datye,[bd] Klaus Schmidt-Rohr,[bc] Brent H. Shanks[ab*]

[a]Department of Chemical and Biological Engineering, Iowa State University, Ames, Iowa 50011, United States

[b]Center for Biorenewable Chemicals, Iowa State University, Ames, Iowa 50011, United States

[c]Department of Chemistry, Brandeis University, Waltham, Massachusetts 02453, United States

[d]Department of Chemical and Biological Engineering and Center for Microengineered Materials, University of New Mexico, Albuquerque, New Mexico 87131, United States

*Corresponding Author

Abstract

Carbon supports have been shown to provide better hydrothermal stability than alumina or silica supports, thus attracting more attention for aqueous-phase biomass conversion reactions. However, sintering and leaching of the metal particles still occur during condensed phase utilization of carbon supported metal catalysts. To further improve the stability of supported metal particles, a simple nitrogen-doped carbon coated SBA-15 was synthesized and systematically characterized. Better stability of supported Pd particles was found from nitrogen incorporation into the carbon support during extended hydrothermal treatment or under continuous flow reaction conditions. With these materials, leaching was negligible and sintering was suppressed. Based on solid-state ^{15}N and ^{13}C NMR analysis before and after hydrothermal treatment, the improved dispersion and stability from

nitrogen doping was ascribed to pyridine, pyrrole, and imidazolium groups. Relatively small carbon fragments resulting from nitrogen incorporation rendered more silica exposure to water and concomitant hydrolysis, but the stability and activity of Pd particles were preserved. The Pd stability advantage was also observed on nitrogen-doped carbon coatings of silica gel and CMK-3 supports. The enhanced stability of Pd particles on different nitrogen-doped carbon materials was correlated with the synergistic effect of oxygen and nitrogen heteroatoms and the formation of a decorative carbon overlayer on the Pd particles.

3.1 Introduction

Biomass conversion continues to attract significant attention as a potentially more sustainable approach to produce value-added fuels and chemicals.[1-5] These conversions are commonly performed in the aqueous phase at various temperatures, but the short term screening studies often used neglect to account for the limited hydrothermal stability of many heterogeneous catalysts. Therefore, stability under realistic reaction conditions remains a challenge.[6-9] Previous efforts have focused on carbon coating of metal oxides, such as alumina and silica, which was shown to increase hydrothermal stability.[10, 11] We have also demonstrated that low-temperature-synthesized carbon with more oxygen functional groups can help disperse and stabilize Pd nanoparticles compared with high temperature carbon supported Pd catalyst.[12] However, carbon coated oxide supported metal catalysts still suffer deactivation after repeated hydrothermal treatments due to leaching and sintering of the metal phase.[12] Carbon as an overcoat on supported Pd catalysts has also been shown to improve stability,[13] but the thin carbon layers can cover and block some of the active sites as well. Silica has been reported to improve the hydrothermal stability of niobia, ZrO_2 and TiO_2, but was still not stable over long

periods of time.[14, 15] Among various metal oxides, TiO_2 was found to be stable only with very low surface areas (< 52 m^2/g).[15]

Nitrogen-doped carbon materials have been explored extensively for electrochemical catalysis,[16-20] supercapacitors,[21] oxidation catalysts,[22] catalyst supports,[23-28] and adsorption.[29-31] Improved activity and selectivity have been observed with nitrogen-doped carbon supported Pd catalysts.[24-26] However, these research were mainly conducted in batch reactors with water or organic solvents at low temperature (less than or equal to 100°C) for a short period of time (less than 3 hours), which may are insufficient to study stability relative to real reactor operation utilizing flow conditions at higher temperature. Moreover, stability studies typically involved repeated batch reactions where complete conversion were performed, which could benefit from excess catalyst loading, so limited detailed information on the catalyst stability is available.[24, 25]

Graphite nitrides have been studied extensively and found to yield improved stability and activity, but usually the surface area is very low (< 10 m^2/g).[32, 33] To overcome this shortcoming, mesoporous graphite nitrides have been explored by using a template, usually with the help of HF etching after nanocasting on mesoporous silicas such as SBA-15.[26, 34] However, this process poses significant chemical handling challenges.

While nitrogen-doped carbon materials showed better activity and stability, the chemical interactions leading to improved activity and stability are still unclear. XPS has been the main technique used to quantify different nitrogen functional group in these materials.[22, 24-26, 28, 35] Unfortunately, the accuracy of XPS interpretation depends on the peak deconvolution procedure used and the resolution of the instrument.[36] Ideally, a complementary technique could be developed that helps refine the understanding of the chemical nature of the nitrogen-doped carbon. Therefore, an important contribution of the current study was to use solid-state NMR to

quantitatively evaluate the nitrogen- and oxygen-containing functional groups in the carbon matrix.

As carbon coating has successfully improved the hydrothermal stability of silica and Pd particles, we further introduced nitrogen into the carbon coating in order to further stabilize Pd particles. Coating nitrogen-doped carbon onto SBA-15 also allowed us to use ^{13}C and ^{15}N solid-state NMR to investigate the chemical moieties on the catalyst surface. A simple nitrogen-doped carbon coated SBA-15 supported Pd catalyst was prepared, which showed improved stability of Pd particles under hydrothermal conditions for an extended time. While the silica structure collapsed as a result of smaller carbon fragments in the carbon coating after nitrogen incorporation, the same stabilization of Pd particles was observed on CMK-3, which maintained its structure during hydrothermal treatment. The nitrogen doping effect on Pd particles was characterized by the traditional XPS, BET surface area, high angle annular dark field (HAADF)-STEM, and high resolution TEM (HRTEM) approaches as well as advanced ^{13}C and ^{15}N solid-state NMR before and after hydrothermal reactions.

3.2 Experiment Section

3.2.1 Catalyst Preparation

The nitrogen-doped carbon materials were synthesized using the following procedure. First, SBA-15 was synthesized according to the literature.[37] Melamine (0.1 g, 99%, Sigma-Aldrich) and glucose (0.5 g, D-glucose anhydrous, Fisher Scientific) were dissolved in nanopure water and then SBA-15 (1 g) was added into the mixture. The resulting aqueous solution with SBA-15 was stirred in an open evaporating dish at room temperature overnight until the water was evaporated and white solid was obtained. The white solid was ground, transferred into a quartz boat, and pyrolyzed in a quartz tube in a tube furnace under UHP argon flow at 300 °C,

400 °C or 600 °C for 10 h with a ramp rate of 5 °C min^{-1}. The nitrogen-doped carbon coated SBA-15 was denoted as 300, 400 or 600NC/SBA-15 depending on the pyrolysis temperature. After washing with hydrochloric acid (1 M), the NC/SBA-15 was then washed with deionized water and vacuum filtered. As a reference, carbon coated SBA-15 was synthesized in a similar manner without melamine and denoted as C/SBA-15. ^{13}C-labeled D-glucose, ^{15}N-labeled melamine, and ^{13}C-labeled melamine were reacted in the same manner for use in the ^{13}C and ^{15}N NMR studies. To examine the effect of the support, nitrogen-doped carbon coating was also synthesized at 300 °C using the same method on an amorphous silica gel (high-purity grade Davisil Grade 636, Sigma Aldrich) and on an ordered mesoporous CMK-3 carbon material. These were denoted as 300NC/silica gel and 300NC/CMK-3, respectively. The CMK-3 was synthesized according to the literature.[38] In addition, 300NC/SBA-15s with different amounts of melamine were also synthesized while keeping the glucose and SBA-15 amounts the same. Incipient wetness impregnation was used for introducing 5 wt% Pd onto the carbon-coated materials using palladium acetate (99.98%, Sigma Aldrich) dissolved in acetone. The catalysts were dried at room temperature and reduced in a tube furnace at 200 °C under 200 mL min^{-1} hydrogen gas flow for 2 h with a ramp rate of 2 °C min^{-1}.

3.2.2 Catalyst Characterization

An ASAP 2020 (Micromeritics) was used to perform BET surface area analysis at -196 °C with liquid nitrogen. Nitrogen physisorption was performed after degassing at 150 °C for 10 hr. The pore volume was reported at a relative pressure of 0.97. Pore size distribution from the adsorption isotherm was calculated by the BJH method. CO pulse chemisorption was measured on an ASAP 2920 (Micromeritics) coupled with a TCD detector. Hydrogen reduction at 200 °C for 2 h was followed by flushing with UHP argon for 15 min before analysis. A stoichiometric

factor of 2 was used for the dispersion calculations.[39, 40] A Kratos Amicus/ESCA 3400 was used to perform X-ray photoelectron spectroscopy (XPS) analysis. Un-monochromated Mg Kα X-ray radiation was used as the X-ray source with CasaXPS software used to process the raw data. A CHNS elemental analyzer (Vario MICRO cube) was used to perform elemental analysis. ICP-OES was performed on a PerkinElmer Optima 8000 ICP-OES Spectrometer with the Pd loading quantified after the catalyst was digested in freshly-made aqua regia for 24 h. For electron microscopy, the samples were dispersed in ethanol and mounted on holey carbon grids for examination using a JEOL 2010F 200 kV transmission electron microscope (resolution of 0.14 nm). Images were recorded in high angle annular dark field (HAADF) and bright-field (HRTEM) modes. At least 250 particles were counted for each catalyst in the particle size distribution analysis.

3.2.3 Hydrothermal Treatment

Hydrothermal treatment was performed in the aqueous phase at 170 °C for 48 h following the same method described previously.[12] A known amount of catalyst was loaded in a 10 mL thick-wall glass vial together with 6 mL of nanopure water. After capping tightly, the glass vials were placed in an oil bath at 170 °C with 400 rpm stirring for 48 h. The catalysts were filtered and washed with DI water, while the aqueous filtered solution was analyzed by ICP-OES to determine the amount of leached Pd.

3.2.4 Reaction Testing

Liquid phase furfural hydrogenation was performed on the catalyst in a fixed-bed reactor as described elsewhere.[41] Before reaction, the catalyst (20 mg) was reduced *in situ* in the reactor with 200 mL/min H_2 (UHP, Airgas) at 200 °C for 30 min (heating tape, a type K thermocouple and a Omega CSI32K PID controller). The reaction was performed at 130 °C. The H_2 gas flow

rate of 20 mL min^{-1} was controlled by a mass flow controller (Brooks SLA5850). The furfural solution (10 g L^{-1}) was fed into the reactor by a high performance liquid chromatograph (HPLC) pump (Series I) at a rate of 0.04 mL min^{-1}. All reactions were performed at the same conditions. A back-pressure regulator was used to maintain the H_2 pressure at 750 psi. The liquid solution was accumulated in a condenser at the top of the reactor, sampled periodically, and filtered with a 0.2 μm syringe filter for gas chromatograph analysis (Agilent 7890A with a flame ionization detector (FID) and a HP-5 ms column). The carbon balances for reactions were calculated based on furfural, furfuryl alcohol, and tetrahydrofurfuryl alcohol and were usually above 90% except those for Pd 600C/SBA-15 and Pd 300NC/SBA-15 (20:8), which were above 85%.

3.2.5 Solid-state ^{15}N and ^{13}C NMR

Solid-state ^{15}N and ^{13}C NMR were performed on the nitrogen-doped carbon overlayers synthesized from selectively isotope-labeled precursors. ^{13}C- and ^{15}N-labeled samples of 300 and 600 NC/SBA-15 were synthesized from melamine-(triamine-$^{15}N_3$) (Sigma-Aldrich, 80-90% ^{15}N in triamine, 10-20% in triazine) and ^{13}C-enriched glucose (U-^{13}C, 99%, Cambridge Isotope Laboratories). ^{13}C-Labeled samples were synthesized from ^{13}C-enriched melamine (Sigma-Aldrich, 99% ^{13}C, 95% purity). The NC/SBA-15 samples were packed into 4 mm outer-diameter zirconia rotors. ^{13}C and ^{15}N NMR spectra were recorded at 100 MHz and 40 MHz, respectively, on a Bruker DSX400 spectrometer. Nearly quantitative ^{13}C and ^{15}N spectra were measured under 14 kHz magic angle spinning (MAS) and high-power ^{1}H decoupling, using composite-pulse multiCP[42, 43] with 2 s recycle and ten 0.3 s repolarization delays. Nearly quantitative spectra of nonprotonated carbon or mobile segments were obtained by using 68 μs of recoupled dipolar dephasing before detection,[44] while the spectra of nonprotonated ^{15}N and ^{13}C multiple bonds away from ^{1}H were obtained from long-range recoupled ^{1}H dipolar dephasing.[45] To identify

protonated and nonprotonated carbons from glucose linked by a bond, two-dimensional (2D) exchange with protonated and nonprotonated spectral editing (EXPANSE) NMR spectra[46] were recorded with a mixing time of 10 ms. To identify the proximity of different carbons originating from melamine in 300NC/SBA-15, a double-quantum/single-quantum (DQ/SQ) spectrum[46] of the sample synthesized from ^{13}C-melamine was measured. A ^{1}H-^{13}C heteronuclear correlation spectrum[47] was also recorded from this sample to elucidate the fate of melamine. To select the signal of ^{13}C near ^{15}N in 300NC/SBA-15, ^{13}C detected rotational-echo double-resonance (REDOR) spectra with 5 rotation periods of recoupling were recorded after multiCP. After selecting the magnetization of ^{13}C near ^{15}N, 1 s spin-diffusion was performed to demonstrate that the nitrogen is uniformly mixed into the carbon film on the 3 nm scale. To identify bonding between ^{13}C and ^{15}N in the doubly-labeled 300NC/SBA-15, 2D ^{13}C-^{15}N HSQC spectra were measured at 7 kHz MAS with 6 rotation periods of ^{13}C-^{15}N recoupling.[48] The corresponding spectra between ^{13}C and nonprotonated ^{15}N were collected after suppression of the signal of nitrogen bonded to hydrogen by the recoupled ^{15}N-^{1}H dipolar interaction.[48]

3.3 Results and Discussion

3.3.1 Characterization of Nitrogen-Doped Carbon Supports

Elemental analysis was performed on the three catalysts before and after 48 h of hydrothermal treatment in water (Figure 3.1). As the pyrolysis temperature increased, the carbon, hydrogen, and nitrogen content decreased, which was likely due to further condensation of the carbon coating. After the treatment, there was some loss of carbon, nitrogen and hydrogen, with 300NC/SBA-15 losing the most weight while 600NC/SBA-15 did not change appreciably. As discussed later in the NMR characterization, small amounts of incompletely pyrolyzed glucose and melamine remained on the 300NC/SBA-15, which were removed during treatment. It was

likely that the weight change for the 400NC/SBA-15 was also due to incompletely pyrolyzed glucose and melamine. These unpyrolyzed species were not present in the higher temperature treated 600NC/SBA-15, so it had the least change in C and N content after hydrothermal treatment.

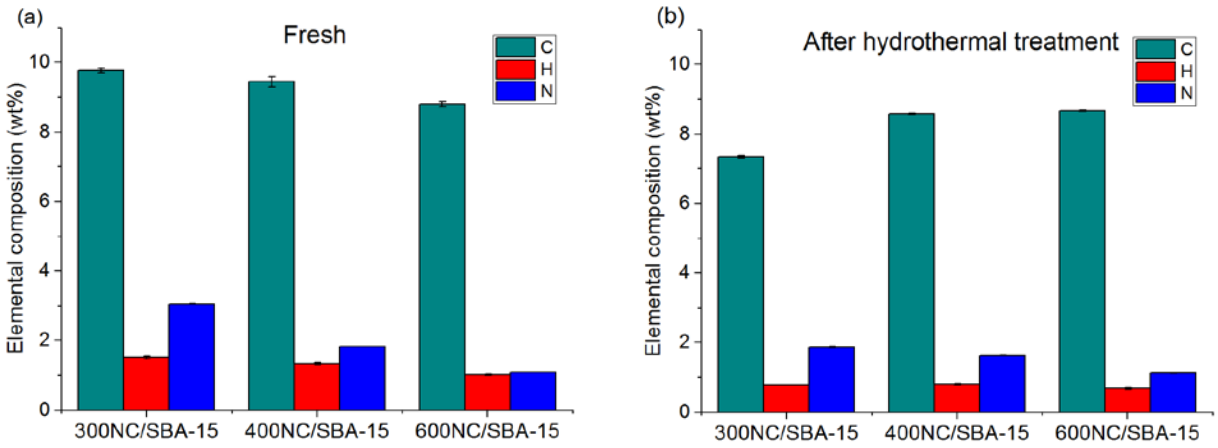

Figure 3.1. Elemental analysis of NC/SBA-15 before (a) and after (b) 48 h hydrothermal treatment.

The surface area of the three NC/SBA-15 materials also increased as the pyrolysis temperature increased (Table 3.1). As shown in Figure S3.1, Type IV isotherms were observed, which indicated mesoporous structure for all three nitrogen-doped carbon materials. A H1 hysteresis was observed for all three fresh supports, indicating ordered cylinder-like pore structures as with the underlying SBA-15. After the 48 h hydrothermal treatment, the hysteresis changed to a H3 type. The pore size distributions of the materials before and after the hydrothermal treatments are shown in Figure S3.2. It was apparent that the mesoporous structure collapsed after hydrothermal treatment as evidenced by the pore size distribution curves as the pore size increased and the pore size distribution was broadened. Table 3.1 shows that both micropore and mesopore volumes decreased after hydrothermal treatment, with the 600NC/SBA-15 synthesized at higher temperature decreasing the least. Compared with just carbon coated

SBA-15 (previously reported results[12]), the nitrogen-doped carbon coating provided less structural integrity to the base SBA-15 as the surface area of the C/SBA-15 only decreased by around 10% after two 24 h hydrothermal treatments.[12] As will be shown below (through NMR characterization) the NC/SBA-15 materials contained significant amounts of pyridine, pyrimidine, pyrrole and amide groups. The nitrogen atoms in the C-N=C or C-NH-C groups have at least one less bond to carbon compared with graphitic carbon, which led to smaller condensation fragments and hence more water-exposed silica surface area. Therefore, the silica was hydrolyzed resulting in the collapse of the ordered mesoporous structure and a decrease in surface area. 300NC/SBA-15 lost the most surface area after the hydrothermal treatment while 600NC/SBA-15 lost the least. This trend was consistent with a more condensed carbon coating obtained from a higher pyrolysis temperature. Since 300NC/SBA-15 and 400NC/SBA-15 contained small amounts of incompletely pyrolyzed glucose and melamine species (confirmed by NMR later), these species dissolved more easily into the aqueous solution, thereby leaving some of the SiO_2 surface unprotected. As a result, the Si-O-Si bond was hydrolyzed by water to Si-OH groups.[49]

As a point of comparison, nitrogen-doped carbon coated 300NC/silica gel and 300NC/CMK-3 were also prepared. The BET surface area, physisorption isotherm, and pore size distribution of the 300NC/silica gel after hydrothermal treatment showed a similar trend to those of 300NC/SBA-15. Conversely, the BET surface area of 300NC/CMK-3 increased after hydrothermal treatment, possibly due to surface roughness. This trend was also seen for carbon coated alumina and silica, resulting in an increase in surface area after a shorter hydrothermal treatment period.[10] As shown in Figure S3.2, the pore size distribution for 300NC/CMK-3 did

not change after hydrothermal treatment and, within error, the BJH average pore diameter remained unchanged.

Table 3.1. BET surface area, pore volume and average pore diameter of supported NC materials before and after hydrothermal treatment.

Sample name		BET surface area (m^2/g)	Total pore volume (cm^3/g)	t-Plot micropore volume (cm^3/g)	Mesopore volume (cm^3/g)	BJH adsorption avg pore diameter (nm)
300NC /SBA-15	fresh	339	0.456	0.017	0.439	5.4
	48h HT[a]	94	0.251	0.006	0.245	10.7
400NC /SBA-15	fresh	351	0.459	0.026	0.433	5.2
	48h HT	147	0.260	0.011	0.249	7.1
600NC /SBA-15	fresh	365	0.468	0.031	0.437	5.1
	48h HT	235	0.371	0.019	0.352	6.3
300NC /silica gel	fresh	261	0.420	0.017	0.403	7.0
	48h HT	119	0.308	0.012	0.296	14.2
300NC /CMK-3	fresh	325	0.381	0.000	0.381	4.5
	48h HT	494	0.515	0.000	0.515	4.2

[a]: HT stands for 48 h of hydrothermal treatment in water at 170 °C.

While it was apparent that use of a nitrogen-doped carbon coating did not provide the same hydrothermal protection for the underlying silica support as did carbon coating, the primary goal of the study was to determine if introducing the nitrogen heteroatoms influenced the hydrothermal stability of Pd particles on the support. Therefore, the materials were also tested after Pd impregnation. CO chemisorption and HAADF-STEM were performed on the catalysts before and after the 48 h hydrothermal treatment. As shown in Table 3.2, CO chemisorption revealed that the dispersions of the Pd NC/SBA-15 catalysts were generally better than with those of the Pd C/SBA-15 materials. The Pd dispersion in all of the samples decreased after hydrothermal treatment, but to a significantly lesser extent for the Pd NC/SBA-15s than for the Pd C/SBA-15s. Additionally, ICP-OES data showed that leaching of Pd from the NC/SBA-15

materials into the solution during hydrothermal treatment was negligible, while it was significant for the C/SBA-15 materials.

Table 3.2. Dispersion and particle size of Pd NC/SBA-15 from CO chemisorption before and after hydrothermal treatment, and leached Pd percentage during hydrothermal treatment.

Sample name	Fresh		48 h HT		
	Dispersion %	Particle size/nm	Dispersion %	Particle size/nm	Pd leached during HT %
Pd 300C/SBA-15[a]	38	2.9	17	6.5	12.130
Pd 400C/SBA-15[a]	32	3.5	15	7.3	9.060
Pd 600C/SBA-15[a]	28	4.1	9	12.0	0.550
Pd 300NC/SBA-15	38	2.9	27	4.1	0.005
Pd 400NC/SBA-15	44	2.6	34	3.3	0.000
Pd 600NC/SBA-15	63	1.8	37	3.1	0.000
Pd 300NC/silica gel	26	4.3	22	5.2	NA

[a]; For Pd C/SBA-15 materials, 48 h of HT (hydrothermal treatment) was performed by two separate 24 h hydrothermal treatments.[12]

HAADF-STEM images (Figure 3.2) show that Pd particles were well dispersed on the fresh 300NC/SBA-15. After the 48 h hydrothermal treatment, the ordered mesoporous silica structure collapsed, in accordance with the decreased BET surface area and the drastic change in pore size distribution. Interestingly, the Pd particles were still well-dispersed, with the STEM surface-weighted average Pd particle diameter increasing only slightly, from 2.0 nm to 2.4 nm. In contrast, Pd on C/SBA-15 sintered to form much bigger particles after two 24 h hydrothermal treatments.[12]

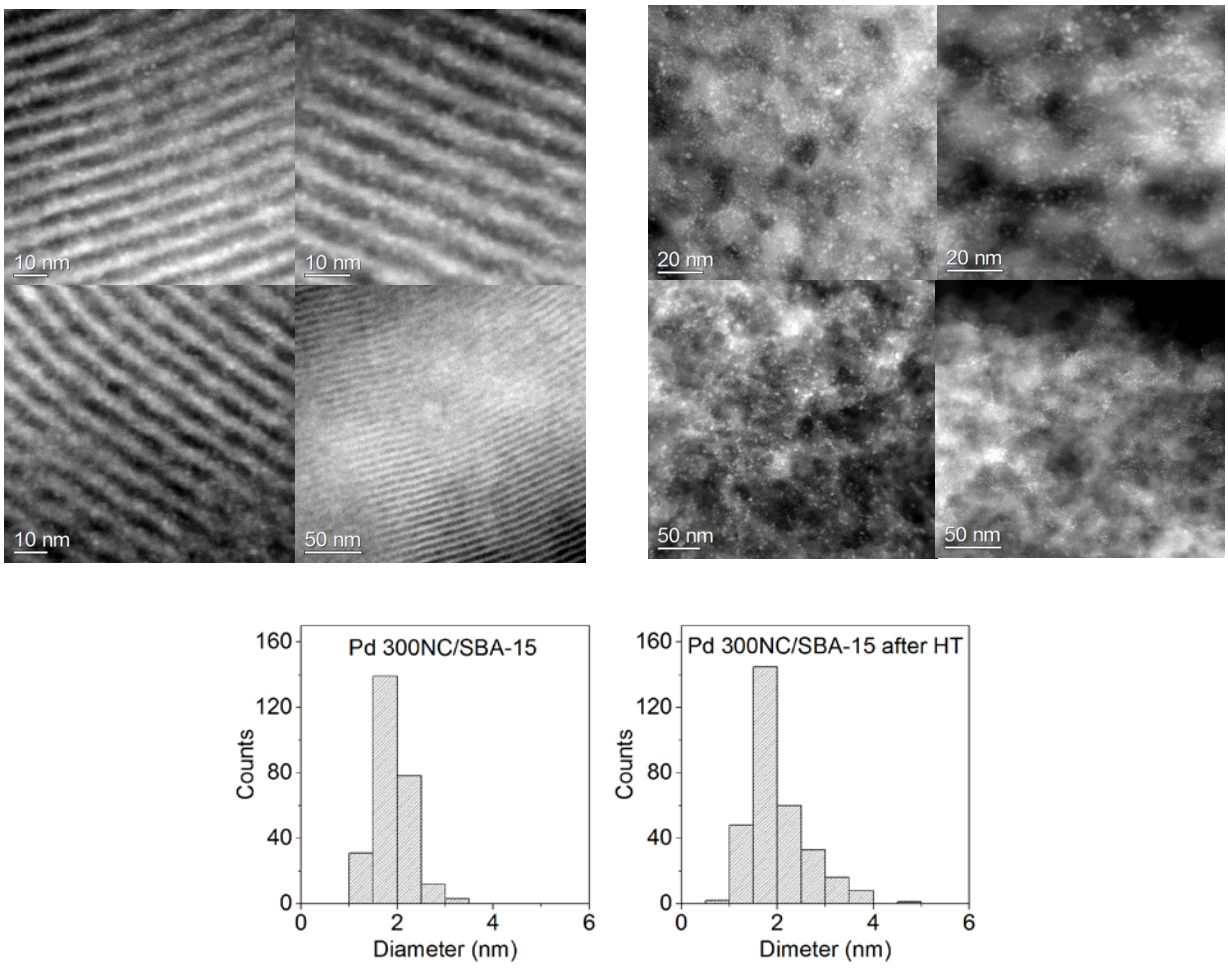

Figure 3.2. HAADF-STEM images (top) and particle size distribution (bottom) of Pd 300NC/SBA-15 before and after 48 h hydrothermal treatment at 170 °C.

To investigate the nitrogen functional groups of the Pd NC/SBA-15s, XPS was performed on the materials. Silicon at 103.4 eV was used to calibrate the spectra. Metallic Pd was found on all three NC/SBA-15 supported Pd catalysts from the Pd 3d XPS spectra (Figure S3.3). Figure 3.3 shows the N1s spectra, in which pyridinic N was assigned at 398.5 eV, pyrrolic N at 400.1 eV, and graphitic N at 401.4 eV.[24, 28]

The nitrogen content decreased with increasing pyrolysis temperature in accordance with elemental analysis. As the pyrolysis temperature increased, both the pyridinic and pyrrolic nitrogen groups decreased. There was a small amount of a graphitic N species in 600NC/SBA-15. Previously, C1s has been used to characterize different C-containing functional groups.[50] However, distinguishing between the many carbon (sp^2 carbon and sp^3 carbon, C=O, COOH, C-O, C=C-O, C=C-N, C=N, C-N) functional groups on the carbon surface in the current materials was beyond the resolution of the XPS instrument. As a result, NMR was used to analyze the carbon surface chemistry and its changes with synthesis temperature and hydrothermal treatment.

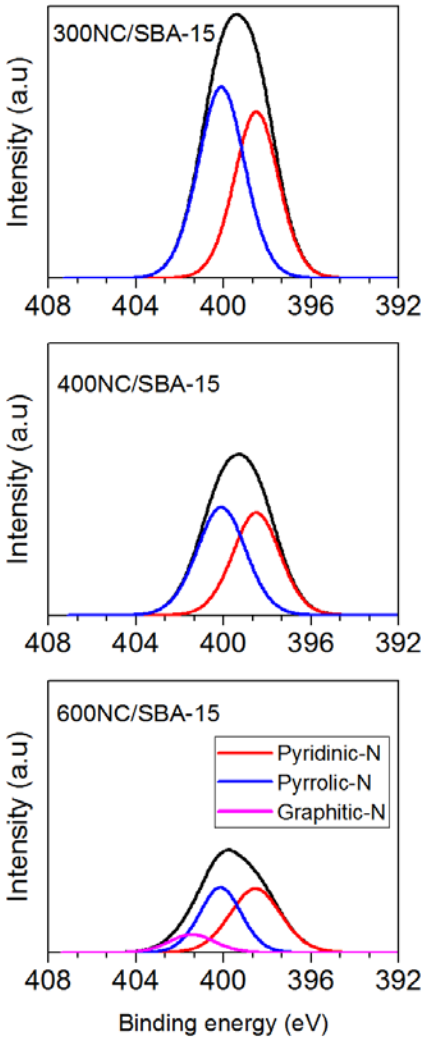

Figure 3.3. N1s XPS spectra of Pd NC/SBA-15, normalized to the same scale.

3.3.2 NMR Characterization

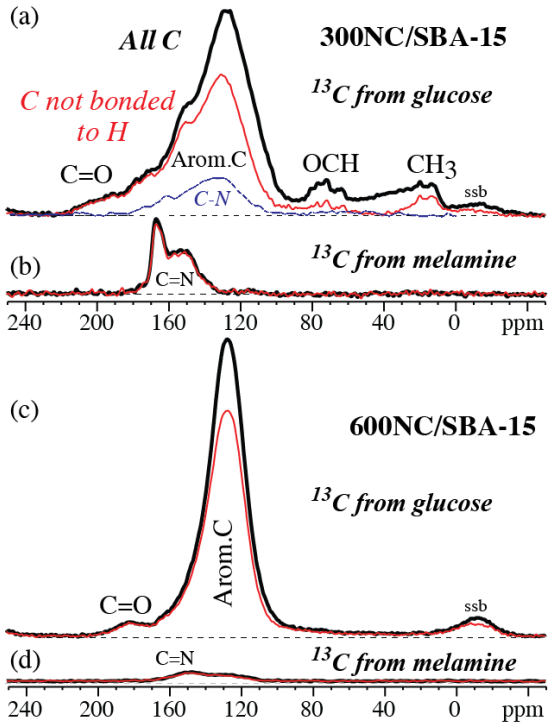

Figure 3.4: Quantitative ^{13}C NMR spectra of (a, b) 300NC/SBA-15 and (c, d) 600NC/SBA-15. (a, c) Signal of carbon derived from $^{13}C_6$-glucose; (b, d) signal of carbon derived from $^{13}C_3$-melamine, corrected for a minor background from natural-abundance ^{13}C in glucose. Spectra of all carbons: bold black line; spectra of nonprotonated carbons and mobile groups: thin red line; spectra of carbon bonded to nitrogen: dashed blue line. The deconvolution of the latter spectra, which was obtained by $^{13}C^{51}$ REDOR[51], is presented in Figure 3.6 below. "ssb": spinning sideband.

To provide structural information on the NC overlayers, the quantitative 13C NMR spectra of 300 and 600NC/SBA-15 were recorded (see Figure 3.4), with and without selection of carbons not bonded to H. Matching the ^{13}C NMR spectra of nominally equivalent materials with and without ^{13}C enrichment (see Figure S3.8) confirmed the reproducibility of the synthesis. A deconvolution of the ^{13}C NMR spectrum of 300NC/SBA-15 in terms of functional groups is shown in Figure S3.9. The spectra derived from ^{13}C-enriched glucose (see Figure 3.4a and c) quite closely resembled those of the corresponding carbon materials made without melamine. This was also confirmed in the ^{13}C-^{13}C correlation spectra of materials made at 300 °C (see

Figure S3.10) which showed signals of furan and arene rings as well as C=O and COO groups bonded to CH_2 and CH_3 groups. On the other hand, the signals of melamine-derived carbon in Figure 3.4b and d were quite distinctive, reflecting continued bonding of these carbons to nitrogen.

For the performance of the materials, knowledge of the chemical forms of nitrogen in the NC overlayers was of particular interest. This was studied by advanced multinuclear (^{15}N, ^{13}C, and ^{1}H) solid-state NMR on variously isotope-labeled materials, with a focus on 300NC/SBA-15. Tracing the fate of the carbons of melamine using 300NC/SBA-15 made from $^{13}C_3$-melamine, it was found that the melamine (i.e. triazine, C_3N_3) rings contributed 7% of all C (compared with 13% in the melamine-glucose reactant mixture) and remained mostly intact after pyrolysis at 300 °C: most ^{13}C derived from melamine resonated in a fairly narrow range between 145 and 170 ppm (see Figure 3.4b), showing that it was still sp^2-hybridized and bonded to three nitrogen atoms or two N and an O atom. This implied that a significant fraction of the nitrogen remained in the nonprotonated triazine form.

On the other hand, the ^{15}N NMR spectra of 300NC/SBA-15 made from $(^{15}NH_2)_3$-labeled melamine (see Figure 3.5 and 3.6) show that most of the NH_2 nitrogen of melamine had undergone a wide variety of chemical transformations, as expected in a Maillard reaction between an amine compound and glucose, a reducing sugar.[48] This result was also consistent with the decreased peak intensities of glucose-like species at 60-90 ppm in Figure 3.4a compared with the just carbon-coated SBA-15 material.[12] Only about 11% of the NH_2 remained in the primary amine form, giving rise to fairly sharp peaks at the edges (right and left, respectively) of the ^{15}N and ^{13}C spectra of the correspondingly isotope-labeled melamine (see Figure 3.5 and 3.4b). As expected, the ^{15}N-^{13}C correlation NMR spectrum of 300NC/SBA-15 made from ^{13}C-

glucose and $(^{15}NH_2)_3$-labeled melamine (Figure 3.6) lacks the NH_2 resonance at 90 ppm in the ^{15}N spectrum since the amine group of melamine is not bonded to any glucose-derived carbon.

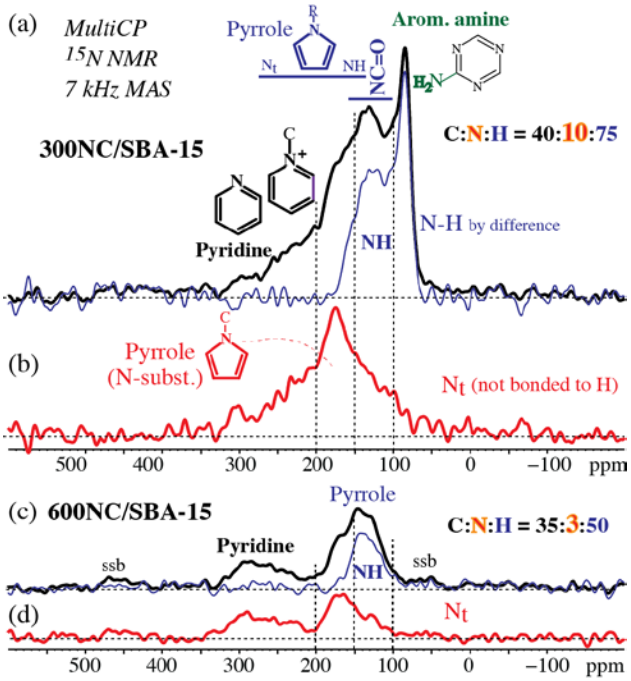

Figure 3.5. MultiCP ^{15}N NMR spectra of (a, b) 300NC/SBA-15 and (c, d) 600NC/SBA-15 made from unlabeled glucose and $(^{15}NH_2)_3$-labeled melamine. (a, c) Top trace (black): full spectrum; bottom trace (thin, blue): spectra of NH, obtained by dipolar-dephasing difference. (b, d): Spectra after dipolar dephasing, with signals of nonprotonated N (tertiary, N_t).

The various forms of nitrogen formed from the NH_2 groups of melamine have been identified by the ^{15}N NMR spectra with spectral editing shown in Figure 3.5 and by ^{15}N-^{13}C 2D NMR with and without dipolar dephasing (Figure 3.6 and S3.11); their amounts were estimated by simultaneous deconvolution of the ^{15}N and ^{13}C spectra[51] (see Figure 3.6). Data for 600NC/SBA-15 are shown in Figure S3.12. The ^{1}H-^{13}C NMR and ^{13}C-^{13}C correlation of ^{13}C derived from $^{13}C_3$-melamine (Figure S3.13 and S3.14) was also taken into account. Overall, 12-14% of all glucose-derived carbons were bonded to nitrogen (see Figure 3.4a and S3.9).

In 300NC/SBA-15, the major form of nitrogen (ca. 27%) was substituted N of pyrrole or imidazolium resonating near 170 ppm. The next abundant form (ca. 13%) was pyridinium, visible as a broad shoulder around 220 ppm in Figure 3.5b and 3.6, and merging with the pyridine/pyrimidine band (~10%), which extends out to 320 ppm. The pyridinium nitrogen presumably remained bonded to melamine. Amide and NCX_2 groups occurred with around 10% abundance each. Their N was mostly bonded to hydrogen. NCX_2 groups with a distinctive ^{13}C resonance near 160 ppm contain sp^2-hybridized carbon bonded to nitrogen and two other heteroatoms, of which one was double-bonded. Ureido ($N_2C=O$) and, less likely, guanidino ($N_2C=N$) groups are examples.[51] The ~160 ppm ^{13}C and 130-160 ppm ^{15}N chemical shifts also match those of cyclic amides with a bond to another sp^2-hybridized carbon, for instance in uracil.[51] A detailed analysis of these spectra is provided in the Supporting Information. While only pyridine, pyrrole and graphitic nitrogen groups were identified by XPS, NMR provided a better resolution of the functional groups including both nitrogen and oxygen moiety groups.

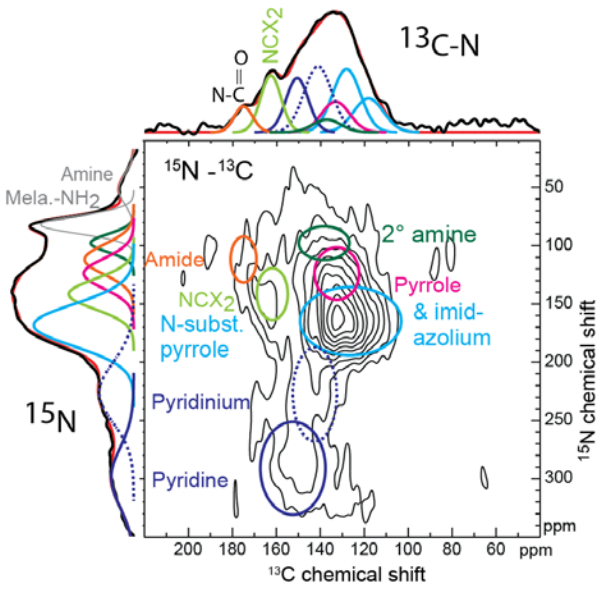

Figure 3.6. Correlated deconvolution of ^{13}C (top) and ^{15}N (left) spectra of 300NC/SBA-15, based on 2D ^{15}N-^{13}C correlation (center). The deconvoluted ^{15}N spectrum along the vertical axis is a

2:1 average of the multiCP spectrum and the projection of the 2D spectrum onto the ^{15}N axis, which partly compensates for enhanced intensity of NH_n in the multiCP and NC_2 in the ^{15}N-^{13}C spectrum. The signals of various functional groups are color coded. The concentrations derived from the analysis are compiled in Table 3.3.

Table 3.3. ^{15}N-^{13}C REDOR NMR analysis of 300NC/SBA-15

	Pyridine	Pyrid-inium	N-subst. pyrrole & imidazolium	Imide	Pyrrole N-H	Amide	2° amine	Mela. -NH_2	Amine
$^{13}C^*$	12%	18%	28%	11%	9%	5%	3%	N. D.	N. D.
^{15}N	9%	13%	27%	13%	10%	10%	5%	11%	3%

*: Since melamine-NH_2 is not bonded to ^{13}C from labeled glucose, it did not show up in the REDOR 2D spectrum. The total percentage of ^{13}C in the table is renormalized to 86%. N. D.: not determined.

Equilibration of ^{13}C magnetization originating from carbons bonded to nitrogen within 1 s of ^{13}C spin diffusion (see Figure S3.15) showed that the nitrogen-containing structures were mixed with the furan, arene, and alkyl segments (but not with most of the untransformed OCH) on a <3 nm scale.

In the 600NC/SBA-15 material, the ^{13}C and ^{15}N NMR signals overall were strongly reduced (see Figure 3.4d and 3.5c). The fraction of carbon from melamine was reduced to 2%, and the nitrogen derived from NH_2 was lower than in 300NC/SBA-15 by a factor of ~4. Pyridine and pyrrole remained most prominent, while NH_2 and pyridinium had been preferentially lost.

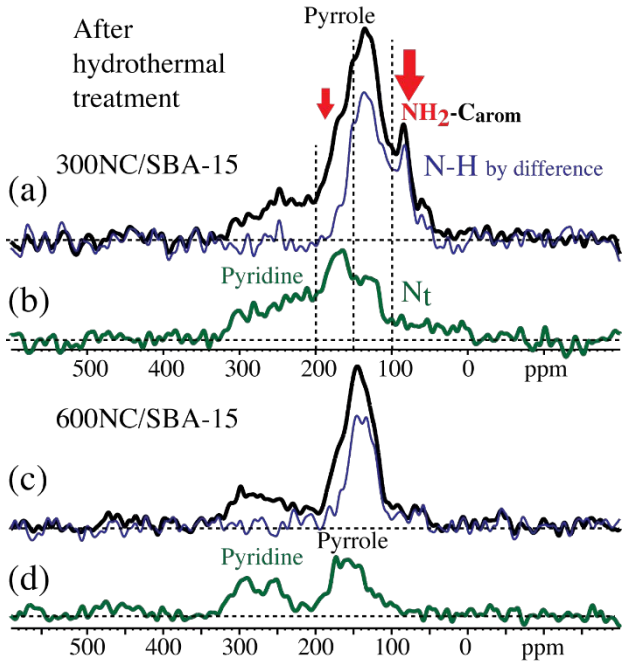

Figure 3.7. MultiCP ^{15}N NMR spectra of (a, b) 300NC/SBA-15 and (c, d) 600NC/SBA-15 made from $(^{15}NH_2)_3$-labeled melamine, after hydrothermal treatment. (a, c) Top trace (black): Full spectrum; bottom trace (thin, blue): Spectra of NH, obtained by dipolar-dephasing difference. (b, d): Spectra after dipolar dephasing, with signals of nonprotonated nitrogen (tertiary, N_t). Red arrows mark signals that have been reduced significantly by the hydrothermal treatment.

Figure 3.7 shows the ^{15}N NMR spectra of 300 and 600 NC/SBA-15 after hydrothermal treatment. Comparison with the spectra in Figure 3.5 demonstrates a partial loss of NH_2 and pyridinium in 300NC/SBA-15, while little change was seen for 600NC/SBA-15. The loss of nitrogen species in 300NC/SBA-15 and little loss in 600NC/SBA-15 were also confirmed by the elemental analysis after hydrothermal treatment, as 300NC/SBA-15 lost about 1/3 of the nitrogen while 600NC/SBA-15 did not lose a significant amount of nitrogen species. The changes in carbon and nitrogen functional groups after hydrothermal treatment are summarized in Tables 3.4 and 3.5. The data in Table 3.4 show a slight decrease in carbon functional groups on 300NC/SBA-15 after hydrothermal treatment, in accordance with elemental analysis, where the carbon percentage dropped from 9.77% to 7.34%. On the other hand, 600NC/SBA-15 showed a

much smaller decrease in carbon functional groups as the carbon percentage in the elemental analysis changed only from 8.80% to 8.67%.

Table 3.4. Fresh vs. hydrothermally treated NC/SBA-15, ^{13}C NMR analysis

^{13}C	Ket-one	Amide & COO	α-XC	Nonp. Arene & NC	Nonp. β-XC	Prot. Arene	Prot. β-XC	OCH_n	CH_n & NCH_n	CH_3
300 **NC**	4%/ 3%	9%/8 %	12%/ 10%	28%/ ~27%*	12%/ ~10%*	10%/ ~9%*	9%/ ~7%*	6%/ 1%	5%/ 3%	5%/ 3%
600 **NC**	4%/6%(2.5% of amide)		13%/ 12%	74%/73%		9%/9%		~0%/~0%		

Each double entry in the table is the percentage of the functional group in the fresh sample vs. the corresponding sample after hydrothermal treatment. The total percentage of the sample after hydrothermal treatment is referenced to the fresh sample.

*: Not fully resolved, estimated.

Table 3.5. Fresh vs. hydrothermally treated NC/SBA-15, NMR analysis of ^{13}C bonded to ^{15}N

^{15}N [1]	Pyridine	Pyridinium	N-subst. pyrrole & imidazolium	Imide	Pyrrole N-H	Amide	2° amine	Mela. $-NH_2$	Am-ine
300°**C**	5%/5%	13%/9%	22%/14%	12%/ 13%	12%/ 11%	10%/ 5%	7%/ 2%	17%/ 5%	2%/ 2%
600°**C**	30%/30%		38%/38%	~0%/ ~0%	32%/ 32%	~0%/ ~19%[2]	~0%/~0%		

Each entry in the table is the percentage of the functional group in the fresh sample vs. the corresponding sample after hydrothermal treatment. The total percentage for the sample after hydrothermal treatment (66% at 300°C, 119% at 600°C) is referenced to the fresh sample.

[1]: This table is for comparison between the fresh and hydrothermally-treated samples only, due to under-estimation of non-protonated ^{15}N in ^{1}H-^{15}N cross polarization (CP). A more quantitative estimation is given in Table 3.3.

[2]: The amide appears to undergo a net increase in ^{15}N. However, it might be due to a highly proton-deficient environment of ^{15}N converted to amide, making it less visible in CP.

The improved hydrothermal stability of Pd NC/SBA-15 was closely correlated with nitrogen doping. Pyridine, pyrrole and imidazolium groups helped to improve the hydrothermal stability of Pd particles since both 300NC/SBA-15 and 600NC/SBA-15 showed better stability than 300C/SBA-15 and 600C/SBA-15, as discussed in the next section. Further, the pyridine and pyrrole contents in both 300NC/SBA-15 and 600NC/SBA-15 remained unchanged after hydrothermal treatment. There was some decrease in amide, secondary amine, and melamine content in 300NC/SBA-15, which was likely due to dissolution of unpyrolyzed melamine-like species during the hydrothermal treatment (Table 3.5). However, as the Pd particle size did not change much and negligible leaching was observed on Pd 300NC/SBA-15, it seems likely that the Pd particles were not anchored on these less stable nitrogen functional groups. The nitrogen functional groups in 600NC/SBA-15 did not change much after hydrothermal treatment. Furthermore, as 300NC/SBA-15 showed better stability in conversion than 600NC/SBA-15 (see below), it was likely that synergistic effects between nitrogen and oxygen heteroatoms induced the extra stability on 300NC/SBA-15 as there were significantly more oxygen-containing functional groups in the carbon coating.

3.3.3 Hydrothermal Reaction Data

The fixed-bed continuous flow reaction of aqueous-phase hydrogenation (APH) of furfural was used as a probe reaction to test the stability of the catalyst at 130 °C and 750 psi for 48 h, see the catalytic data in Figure 3.8. All of the Pd NC/SBA-15 catalysts showed both better activity and stability than the Pd C/SBA-15 catalysts. The better activity of Pd NC/SBA-15 could be attributed to smaller Pd particles, as indicated by both CO chemisorption in Table 3.2 and HAADF-STEM analysis in Figure 3.9 and Table 3.6. The incorporation of nitrogen helped to improve the dispersion of Pd particles, which was likely due to the strong interaction between Pd

particles and nitrogen functional groups.[25, 27, 52] It appeared that this strong interaction also greatly diminished the sintering of the metal particles. This effect was demonstrated with the better stability of Pd NC/SBA-15 compared with Pd C/SBA-15. As reported previously, Pd 300C/SBA-15 gave better activity and stability than Pd 600C/SBA-15, suggesting that the low-temperature synthesized carbon with its more oxygen functional groups allowed for better dispersion and stabilization of the Pd particles.[12] Pd 300NC/SBA-15 also showed better stability than the higher temperature Pd 600NC/SBA-15 as the deactivation rate of Pd 300NC/SBA-15 was about half that of Pd 600NC/SBA-15. Importantly, less than 1% of the total Pd leached into the reaction solution for all four catalysts, as verified by ICP-OES.

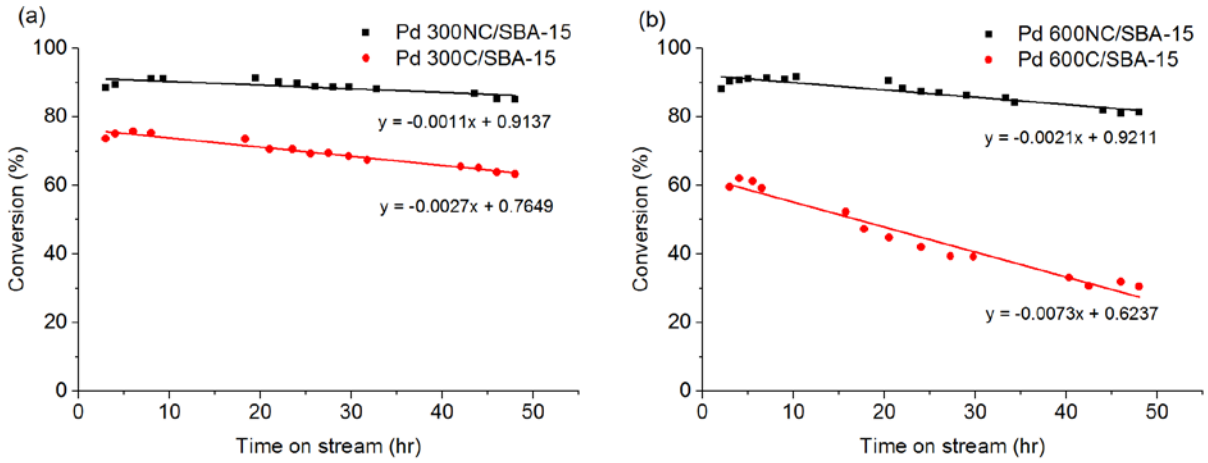

Figure 3.8. Furfural hydrogenation (a) Pd 300NC/SBA-15, Pd 300C/SBA-15, (b) Pd 600NC/SBA-15, Pd 600C/SBA-15, at 130 °C, 750 psi for 48 h.

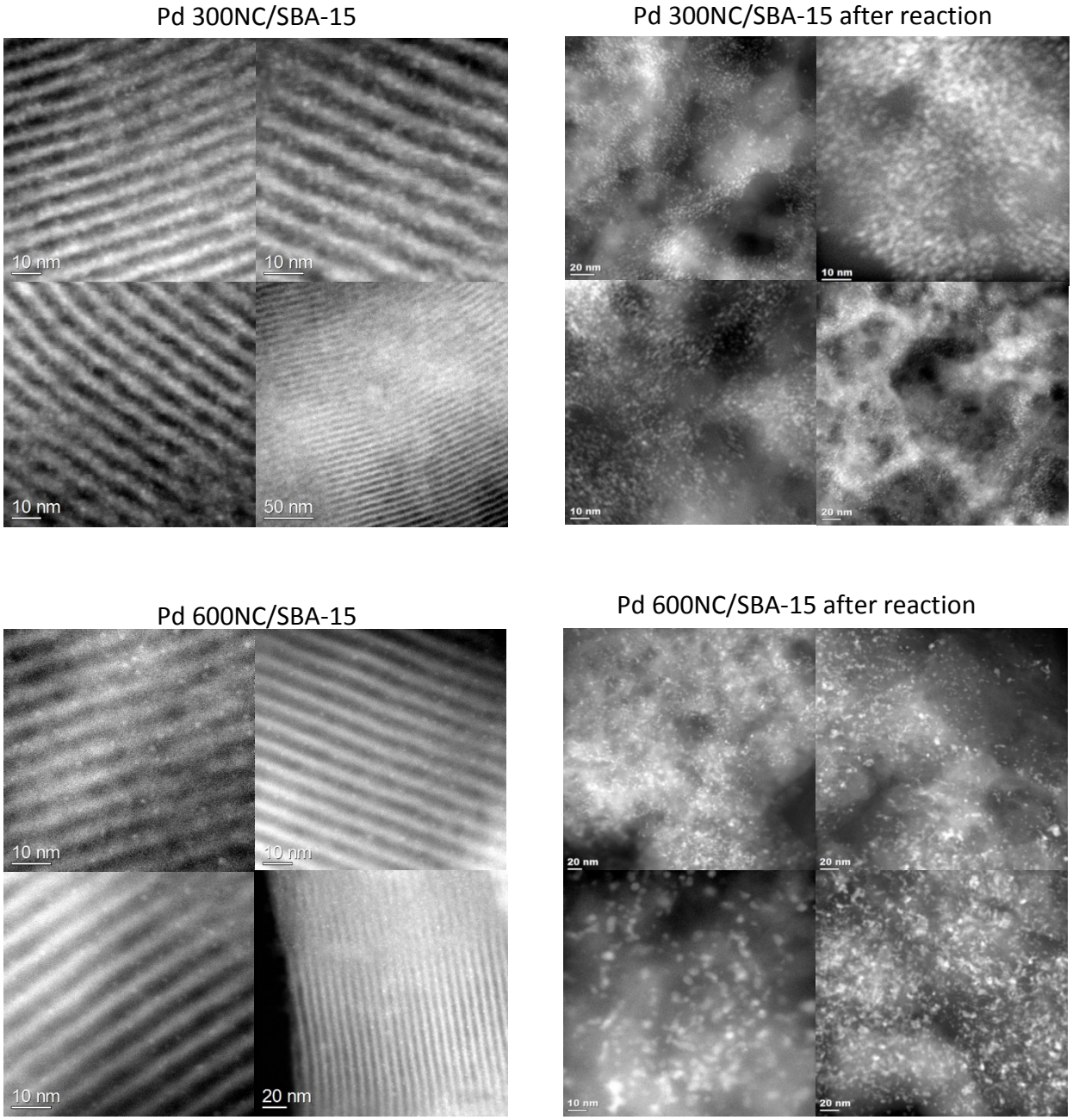

Figure 3.9. HAADF-STEM images of Pd 300NC/SBA-15, and Pd 600NC/SBA-15 before and after 48 h of reaction time-on-stream.

Monitoring catalyst changes is indispensable in a stability study. Therefore, STEM analysis was performed on Pd 300NC/SBA-15 and Pd 600NC/SBA-15 before and after 48 h of reaction (Figure 3.9). As with the hydrothermal stability tests, the mesoporous structure

collapsed for both 300NC/SBA-15 and 600NC/SBA-15 as the ordered cylindrical pores of SBA-15 disappeared. However, the Pd particles were still well dispersed. This result was surprising since previous work found that when the underlying oxide support lost its structural integrity, the metal phase significantly sintered.[13]

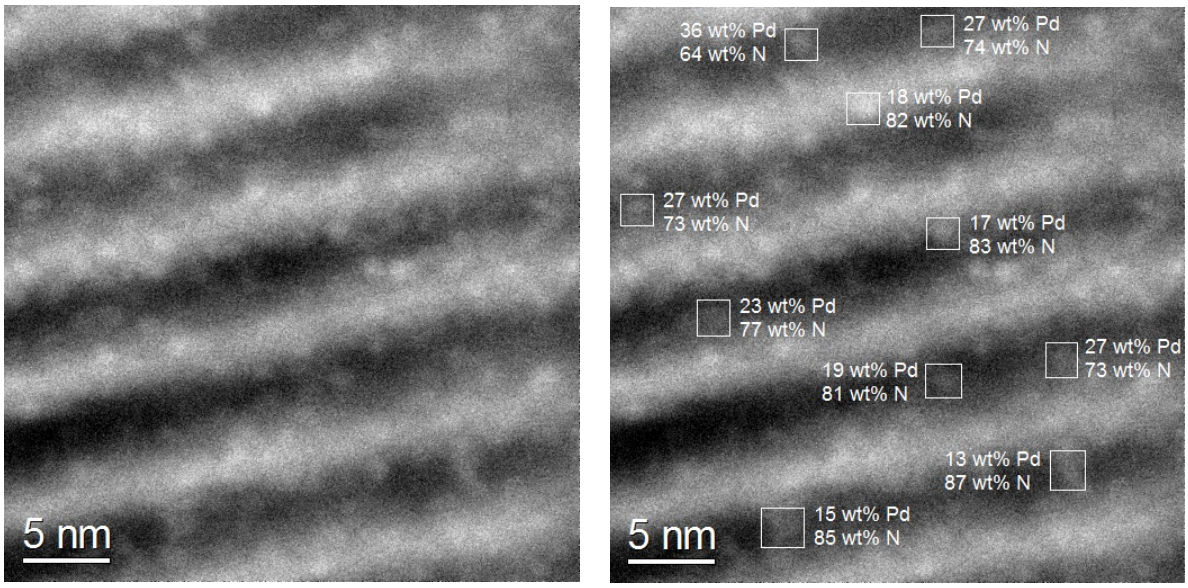

Figure 3.10. HAADF-STEM image (left) and elemental compositions of individual Pd particles (right) for fresh Pd 300NC/SBA-15.

Sintering occurred to some extent in both catalysts, as indicated by the particle size data in Table 3.6 and particle size distribution in Figure S3.4. More sintering was observed for the Pd 600NC/SBA-15 as the particle size increased from 2.2 nm to 4.0 nm while Pd 300NC/SBA-15 only slightly increased from 2.0 nm to 2.3 nm. To examine how fast the ordered mesoporous structure of SBA-15 was destroyed, STEM analysis was performed after a shortened reaction time (10 h). As shown in Figure S3.5, some of the ordered mesoporous structure was intact at that time, suggesting a gradual destruction of the SBA-15 structure with time-on-stream. STEM-EDS analysis on fresh Pd 300NC/SBA-15 in Figure 3.10 suggested that the Pd particles were

anchored to nitrogen functional groups. This direct interaction between the nitrogen heteroatoms and Pd could be the reason that the Pd particles had minimal sintering even when the underlying silica support was hydrolyzed.

Previous research on hydrothermal reactions has shown that sintering was a common cause of deactivation rather than leaching.[13, 53] Bond et al. found that Ru particles sintered to larger particles on Al_2O_3, TiO_2, SiO_2, and carbon at temperatures as low as 50 °C during aqueous hydrogenation of levulinic acid.[54] As evidenced here, nitrogen-doping of carbon appears to offer a promising approach for stabilizing Pd particles.

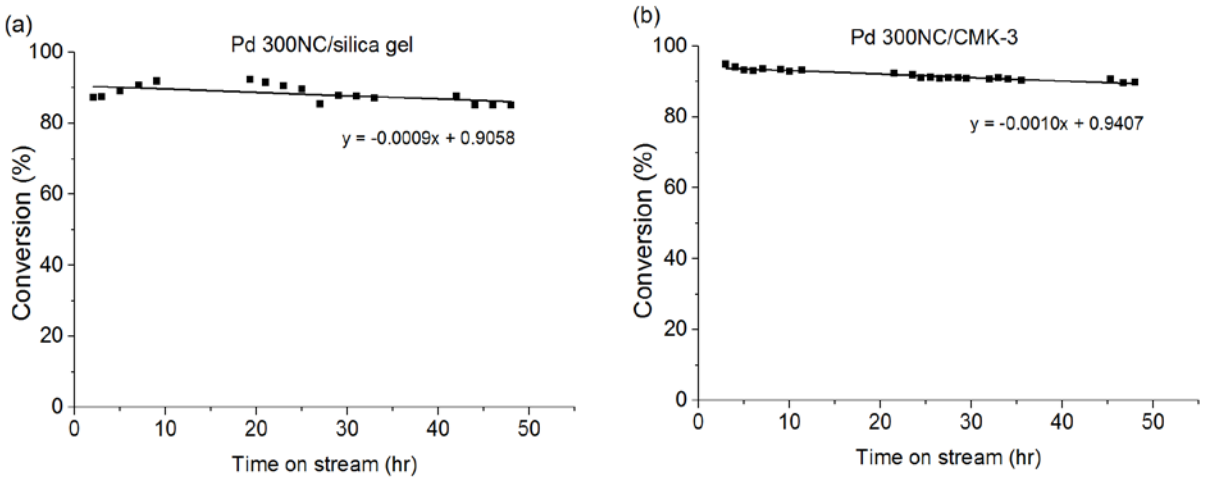

Figure 3.11. Continuous flow hydrogenation of furfural on (a) Pd 300NC/silica gel and (b) Pd 300NC/CMK-3 at 130 °C, 750 psi for 48 h.

To further investigate the effect of the underlying support on stability, a nitrogen-doped carbon coating was synthesized on mesoporous silica gel, followed by 48 h of hydrothermal treatment and continuous flow reaction. The 300NC/silica gel also lost more than half of its initial surface area during hydrothermal treatment (Table 3.1) and showed a much broader pore size distribution (Figure S3.2). However, the Pd 300NC/silica gel as shown in Figure 3.11 gave a

similar activity and stability in furfural conversion to Pd 300NC/SBA-15. STEM analysis also revealed no change in average Pd particle size after the reaction (Figure S3.4 and S3.16).

As the SBA-15 and silica gel supports were hydrolyzed under hydrothermal conditions due to smaller carbon fragments from nitrogen incorporation, we further prepared a nitrogen-doped carbon coated CMK-3, an ordered mesoporous carbon material known to have hydrothermal stability. A similar retention of catalytic activity was observed on Pd 300NC/CMK-3 compared to Pd 300NC/silica gel (Figure 3.11). The ordered mesoporous structure of CMK-3 was confirmed by STEM both before and after reaction for 48 h in Figure S3.16, with little Pd sintering (Figure S3.4).

Although the initial Pd particle sizes for the Pd 300NC/SBA-15, Pd 600NC/SBA-15, Pd 300NC/silica gel, and Pd 300NC/CMK-3 materials were different, their initial activity was similar (around 90% conversion). The initial and final overall reactivity of the catalyst were calculated as summarized in Table 3.6 below. These calculated values strongly suggest that the reaction was mass-transfer limited as the furfural hydrogenation is quite fast with a Pd catalyst and the reactivity per site increased as the pore size increased during the hydrothermal reaction. While the reaction conditions could have been selected to avoid mass transfer limitations by lowering the reaction temperature, an important goal of the study was to examine catalyst stability under hydrothermal conditions relevant to common aqueous phase reactions. The greater deactivation rate of Pd 600NC/SBA-15 than Pd 300NC/SBA-15 was likely due to its more significant Pd particle sintering. For Pd 300NC/silica gel and Pd 300NC/CMK-3, the overall reactivity per site remained unchanged throughout the reaction. The different reactivity per site induced by the different particle size and potentially different metal-support interaction is not the focus of this paper.

Table 3.6. Dispersion and particle size from CO chemisorption and STEM before and after 48 hr flow reaction.

Sample name	Fresh					After reaction		
	Disper-sion[a] %	Particle size[a] /nm	STEM Particle diameter[b] /nm	Fraction of surface atoms[c] %	Initial reactiv-ity[d] /s^{-1}	STEM Particle diameter[b] /nm	Fraction of surface atoms[c] %	Ending reactiv-ity[d] /s^{-1}
Pd 300NC /SBA-15	38	2.9	2.0	55	0.0132	2.3	49	0.0145
Pd 600NC /SBA-15	63	1.8	2.2	52	0.0139	4.0	28	0.0233
Pd 300NC /silica gel	26	4.3	3.2	35	0.0185	3.2	35	0.0183
Pd 300NC /CMK-3	27	4.1	2.5	45	0.0158	2.7	41	0.0162
Pd 300C /SBA-15	38	2.9	3.1	36	0.0153	NA	NA	NA
Pd 600C /SBA-15	28	4.1	3.8	30	0.0154	NA	NA	NA

[a]; Data from CO chemisorption. [b]: Data from surface-weighted average diameter from STEM using $\sum d^3/\sum d^2$. [c]: Fraction of surface atoms is calculated from $1.12/d$ (measured by STEM).[12] [d]: Initial and final overall reactivity per site were calculated by using the equation below; fraction of surface atoms from STEM was used as dispersion in the calculation.

$$\text{reactivity per site} = \frac{(\text{moles of reactant converted})}{\{(\text{moles of metal in catalyst}) \times (\text{dispersion}) \times (\text{reaction time})\}}$$

3.3.4 The Influence of Nitrogen Loading on Hydrothermal Stability

To study the effects of nitrogen loading on hydrothermal stability, Pd 300NC/SBA-15 materials were synthesized with different melamine loadings while keeping the SBA-15 to glucose ratio the same. Table 3.7 shows the dispersion and particle size of Pd 300NC/SBA-15 with different amounts of nitrogen in the coating. In the reaction studies, the stability decreased when too little nitrogen was present in the coating (Figure 3.12). The material with a melamine ratio of 20:4 gave the highest dispersion and the lowest activity loss during reaction.

Table 3.7. CO chemisorption dispersion and particle size of Pd 300NC/SBA-15 with different melamine content (G: glucose, M: melamine).

	Dispersion%	Particle size/nm
Pd 300NC/SBA15 (G:M 20:8)	33	3.4
Pd 300NC/SBA15 (G:M 20:4)	38	3.0
Pd 300NC/SBA15 (G:M 20:2)	33	3.4
Pd 300NC/SBA15 (G:M 20:1)	32	3.5

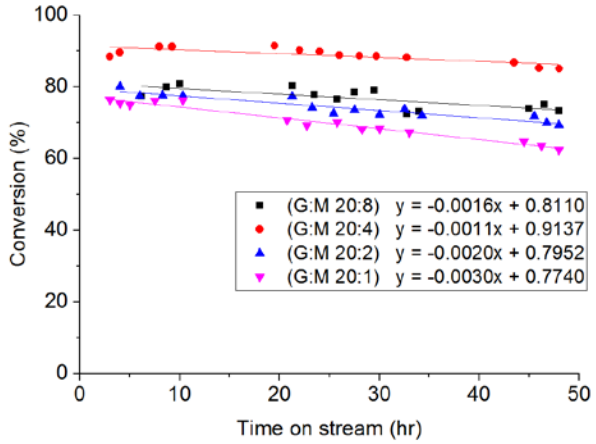

Figure 3.12. Aqueous-phase hydrogenation of furfural for Pd 300NC/SBA-15 with different melamine contents. G stands for glucose and M stands for melamine.

3.3.5 Insights into the Nitrogen-Doped Carbon Coating on Improved Hydrothermal Stability

HRTEM of the Pd 300NC/SBA-15 and Pd 600NC/SBA-15 after 48 h of reaction showed that the Pd particles were covered with a carbon protective overlayer. A thicker carbon overlayer was observed for the Pd 300NC/SBA-15 as seen in Figure 3.13. Meanwhile, the carbon overlayer was significantly less for the Pd particles on Pd 600NC/SBA-15. Given the high reactivity of Pd 300NC/SBA-15 even after 48 h, it would appear that the carbon overlayer on the Pd particles was porous and did not block the active sites. The HRTEM images suggested that the carbon overlayer may help to protect the Pd particles from sintering and leaching under the hydrothermal conditions. The different thickness of the carbon overlayer on the Pd particles

could have been due to the carbon coating on 300NC/SBA-15 being less condensed and containing more oxygen and nitrogen functional groups, which allowed for more mobility of the carbon relative to the more condensed carbon coating on 600NC/SBA-15. A similar trend was seen for the Pd 300C/SBA-15 and Pd 600C/SBA-15 materials as well. Given the enhanced

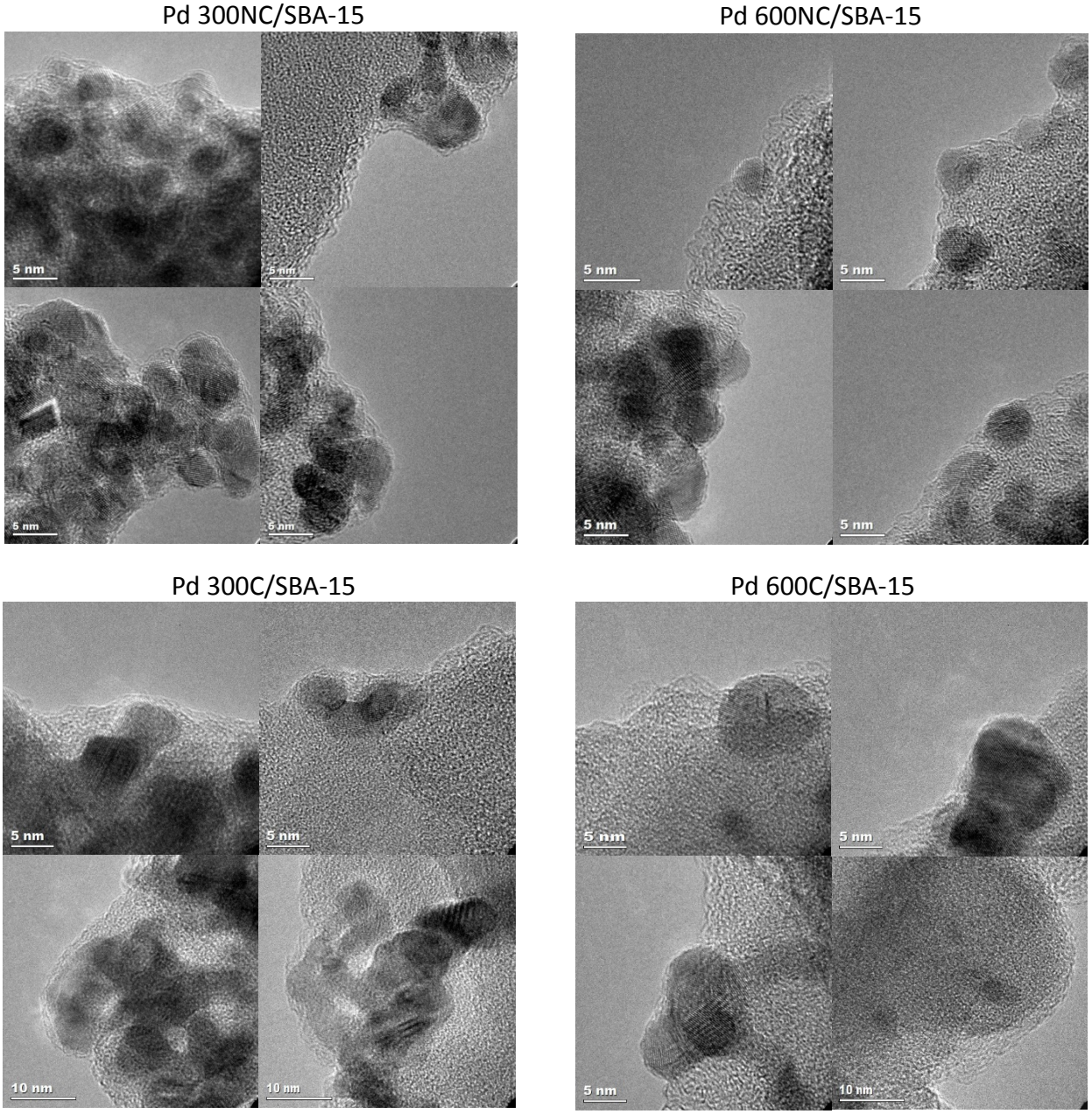

Figure 3.13. HRTEM images of Pd 300NC/SBA-15 and Pd 600NC/SBA-15 (top); Pd 300C/SBA-15 and Pd 600C/SBA-15 (bottom) after 48 h of flow reaction.

stability of Pd 300NC/SBA-15 relative to Pd 300C/SBA-15, the apparent migration of some

carbon over the Pd particles was not the only mechanism for stabilizing the Pd particles. Therefore, the presence of nitrogen heteroatoms in the coating layer was still an important contributor to the stability of the Pd 300NC/SBA-15 catalyst.

3.4 Conclusions

Novel Pd NC/SBA-15 materials were synthesized and characterized extensively through HRTEM, HAADF-STEM, as well as ^{13}C and ^{15}N NMR before and after hydrothermal treatment and flow reaction conditions. These materials gave better hydrothermal stability of the Pd nanoparticles than carbon coated SBA-15 materials without nitrogen functional groups, as both leaching and sintering of the Pd were reduced. Better dispersion of the Pd particles was also observed for the nitrogen-doped materials. The lower temperature synthesized Pd 300NC/SBA-15, which had more nitrogen and oxygen heteroatoms in the carbon coating, showed better stability than Pd 600NC/SBA-15. Unfortunately, the introduction of nitrogen into the carbon coating resulted in a less stable underlying silica support relative to the carbon-only coated SBA-15, as smaller carbon fragments resulting from nitrogen incorporation appeared to allow water to interact with the underlying silica, leading to structural collapse of the mesoporous silica structure under hydrothermal conditions. Remarkably, the stability of the Pd particles was not affected by hydrolysis of the silica. A similar testing with Pd 300NC/silica gel and Pd 300NC/CMK-3 demonstrated that the coating technique could be applied to other support materials as well, with the CMK-3 in particular being promising due to its intrinsic hydrothermal structural stability. Detailed ^{15}N and ^{13}C NMR characterization indicated that pyridine, pyrrole, and imidazolium groups helped to improve the hydrothermal stability of Pd particles. The particularly enhanced stability of 300NC/SBA-15 could have been due to both the presence of oxygen and nitrogen functional groups in the carbon coating as well as the formation of a

protective carbon overlayer on the Pd particles. The strategy of nitrogen doping into carbon material offers a new approach to improve the hydrothermal stability of the supported metal catalyst under relevant biomass conversion conditions.

3.5 Acknowledgement

This work is supported by the Center for Biorenewable Chemicals funded by NSF grant EEC-0813570. We would like to thank Dr. Dapeng Jing for XPS analysis, Dr. Yuan Xue for elemental analysis, and Dr. Patrick Johnston for ICP analysis. We also thank Professor Jean-Philippe Tessonnier for helpful discussions.

3.6 References

1. D. M. Alonso, J. Q. Bond and J. A. Dumesic, *Green Chem.*, 2010, **12**, 1493-1513.
2. J. S. Luterbacher, D. M. Alonso and J. A. Dumesic, *Green Chem.*, 2014, **16**, 4816-4838.
3. G. W. Huber, S. Iborra and A. Corma, *Chem. Rev.*, 2006, **106**, 4044-4098.
4. J. N. Chheda, G. W. Huber and J. A. Dumesic, *Angew. Chem. Int. Ed.*, 2007, **46**, 7164-7183.
5. M. J. Climent, A. Corma and S. Iborra, *Green Chem.*, 2014, **16**, 516-547.
6. J.-P. Lange, *Angew. Chem. Int. Ed.*, 2015, **54**, 13186-13197.
7. H. Xiong, H. N. Pham and A. K. Datye, *Green Chem.*, 2014, **16**, 4627-4643.
8. T. J. Schwartz, B. J. O'Neill, B. H. Shanks and J. A. Dumesic, *ACS Catal.*, 2014, **4**, 2060-2069.
9. C. Sievers, Y. Noda, L. Qi, E. M. Albuquerque, R. M. Rioux and S. L. Scott, *ACS Catal.*, 2016, **6**, 8286-8307.
10. H. N. Pham, A. E. Anderson, R. L. Johnson, K. Schmidt-Rohr and A. K. Datye, *Angew. Chem. Int. Ed.*, 2012, **51**, 13163-13167.

11. H. Xiong, T. J. Schwartz, N. I. Andersen, J. A. Dumesic and A. K. Datye, *Angew. Chem. Int. Ed.*, 2015, **54**, 7939-7943.

12. J. Huo, R. L. Johnson, P. Duan, H. N. Pham, D. Mendivelso-Perez, E. A. Smith, A. K. Datye, K. Schmidt-Rohr and B. H. Shanks, *Catal. Sci. Technol.*, 2018, **8**, 1151-1160.

13. H. N. Pham, A. E. Anderson, R. L. Johnson, T. J. Schwartz, B. J. O'Neill, P. Duan, K. Schmidt-Rohr, J. A. Dumesic and A. K. Datye, *ACS Catal.*, 2015, **5**, 4546-4555.

14. H. N. Pharn, Y. J. Pagan-Torres, J. C. Serrano-Ruiz, D. Wang, J. A. Dumesic and A. K. Datye, *Appl. Catal. A*, 2011, **397**, 153-162.

15. J. Z. Duan, Y. T. Kim, H. Lou and G. W. Huber, *Catal. Today*, 2014, **234**, 66-74.

16. Y. Qiu, J. J. Huo, F. Jia, B. H. Shanks and W. Z. Li, *J. Mater. Chem. A*, 2016, **4**, 83-95.

17. H. B. Wang, T. Maiyalagan and X. Wang, *ACS Catal.*, 2012, **2**, 781-794.

18. W. Ju, M. Favaro, C. Durante, L. Perini, S. Agnoli, O. Schneider, U. Stimming and G. Granozzi, *Electrochim. Acta*, 2014, **141**, 89-101.

19. L. Perini, C. Durante, M. Favaro, S. Agnoli, G. Granozzi and A. Gennaro, *Appl. Catal. B*, 2014, **144**, 300-307.

20. L. Perini, C. Durante, M. Favaro, V. Perazzolo, S. Agnoli, O. Schneider, G. Granozzi and A. Gennaro, *ACS Appl. Mater. Interfaces*, 2015, **7**, 1170-1179.

21. L. F. Chen, X. D. Zhang, H. W. Liang, M. G. Kong, Q. F. Guan, P. Chen, Z. Y. Wu and S. H. Yu, *ACS Nano*, 2012, **6**, 7092-7102.

22. Z. S. Ma, H. Y. Zhang, Z. Z. Yang, G. P. Ji, B. Yu, X. W. Liu and Z. M. Liu, *Green Chem.*, 2016, **18**, 1976-1982.

23. K. Chizari, I. Janowska, M. Houlle, I. Florea, O. Ersen, T. Romero, P. Bernhardt, M. J. Ledoux and C. Pham-Huu, *Appl. Catal. A*, 2010, **380**, 72-80.

24. Z. L. Li, J. H. Liu, C. G. Xia and F. W. Li, *ACS Catal.*, 2013, **3**, 2440-2448.

25. Z. L. Li, J. L. Li, J. H. Liu, Z. L. Zhao, C. G. Xia and F. W. Li, *ChemCatChem*, 2014, **6**, 1333-1339.

26. Y. Wang, J. Yao, H. R. Li, D. S. Su and M. Antonietti, *JACS*, 2011, **133**, 2362-2365.

27. X. Xu, Y. Li, Y. T. Gong, P. F. Zhang, H. R. Li and Y. Wang, *JACS*, 2012, **134**, 16987-16990.

28. P. F. Zhang, Y. T. Gong, H. R. Li, Z. R. Chen and Y. Wang, *Nat. Commun.*, 2013, **4**.

29. W. Z. Shen and W. B. Fan, *J.Mater. Chem. A*, 2013, **1**, 999-1013.

30. Z. X. Wu, P. A. Webley and D. Y. Zhao, *J. Mater. Chem.*, 2012, **22**, 11379-11389.

31. S. S. Feng, W. Li, Q. Shi, Y. H. Li, J. C. Chen, Y. Ling, A. M. Asiri and D. Y. Zhao, *Chem. Commun.*, 2014, **50**, 329-331.

32. Y. Wang, X. C. Wang and M. Antonietti, *Angew. Chem. Int. Ed.*, 2012, **51**, 68-89.

33. A. Thomas, A. Fischer, F. Goettmann, M. Antonietti, J. O. Muller, R. Schlogl and J. M. Carlsson, *J. Mater. Chem.*, 2008, **18**, 4893-4908.

34. X. H. Li, X. C. Wang and M. Antonietti, *Chem. Sci.*, 2012, **3**, 2170-2174.

35. M. Lezanska, P. Pietrzyk and Z. Sojka, *J. Phys. Chem. C*, 2010, **114**, 1208-1216.

36. G. Ertl, H. Knözinger and J. Weitkamp, *Handbook of Heterogeneous Catalysis*, Wiley, 2008.

37. D. Y. Zhao, J. L. Feng, Q. S. Huo, N. Melosh, G. H. Fredrickson, B. F. Chmelka and G. D. Stucky, *Science*, 1998, **279**, 548-552.

38. S. Jun, S. H. Joo, R. Ryoo, M. Kruk, M. Jaroniec, Z. Liu, T. Ohsuna and O. Terasaki, *JACS* 2000, **122**, 10712-10713.

39. P. Canton, G. Fagherazzi, M. Battagliarin, F. Menegazzo, F. Pinna and N. Pernicone, *Langmuir*, 2002, **18**, 6530-6535.

40. G. Fagherazzi, P. Canton, P. Riello, N. Pernicone, F. Pinna and A. Battagliarin, *Langmuir*, 2000, **16**, 4539-4546.

41. B. J. O'Neill, D. H. K. Jackson, A. J. Crisci, C. A. Farberow, F. Shi, A. C. Alba-Rubio, J. Lu, P. J. Dietrich, X. Gu, C. L. Marshall, P. C. Stair, J. W. Elam, J. T. Miller, F. H. Ribeiro, P. M. Voyles, J. Greeley, M. Mavrikakis, S. L. Scott, T. F. Kuech and J. A. Dumesic, *Angew. Chem. Int. Ed.*, 2013, **52**, 13808-13812.

42. R. L. Johnson and K. Schmidt-Rohr, *J. Magn. Reson.*, 2014, **239**, 44-49.

43. P. Duan and K. Schmidt-Rohr, *J. Magn. Reson.*, 2017, **285**, 68-78.

44. J. D. Mao and K. Schmidt-Rohr, *Environ. Sci. Technol.*, 2004, **38**, 2680-2684.

45. J. D. Mao and K. Schmidt-Rohr, *J. Magn. Reson.*, 2003, **162**, 217-227.

46. R. L. Johnson, J. M. Anderson, B. H. Shanks, X. Fang, M. Hong and K. Schmidt-Rohr, *J. Magn. Reson.*, 2013, **234**, 112-124.

47. J. D. Mao, B. Xing and K. Schmidt-Rohr, *Environ. Sci. Technol.*, 2001, **35**, 1928-1934.

48. X. Fang and K. Schmidt-Rohr, *J. Agric. Food. Chem.*, 2009, **57**, 10701-10711.

49. R. A. Pollock, G. Y. Gor, B. R. Walsh, J. Fry, I. T. Ghampson, Y. B. Melnichenko, H. Kaiser, W. J. DeSisto, M. C. Wheeler and B. G. Frederick, *J. Phys. Chem. C*, 2012, **116**, 22802-22814.

50. S. Reiche, R. Blume, X. C. Zhao, D. Su, E. Kunkes, M. Behrens and R. Schloegl, *Carbon*, 2014, **77**, 175-183.

51. X. W. Fang, J. D. Mao, R. M. Cory, D. M. McKnight and K. Schmidt-Rohr, *Magn. Reson. Chem.*, 2011, **49**, 775-780.

52. S. S. Chen, P. Y. Qi, J. Chen and Y. Z. Yuan, *RSC Adv.*, 2015, **5**, 31566-31574.

53. O. A. Abdelrahman, A. Heyden and J. Q. Bond, *ACS Catal.*, 2014, **4**, 1171-1181.

54. O. A. Abdelrahman, H. Y. Luo, A. Heyden, Y. Roman-Leshkov and J. Q. Bond, *J. Catal.*, 2015, **329**, 10-21.

3.7 Supporting Information

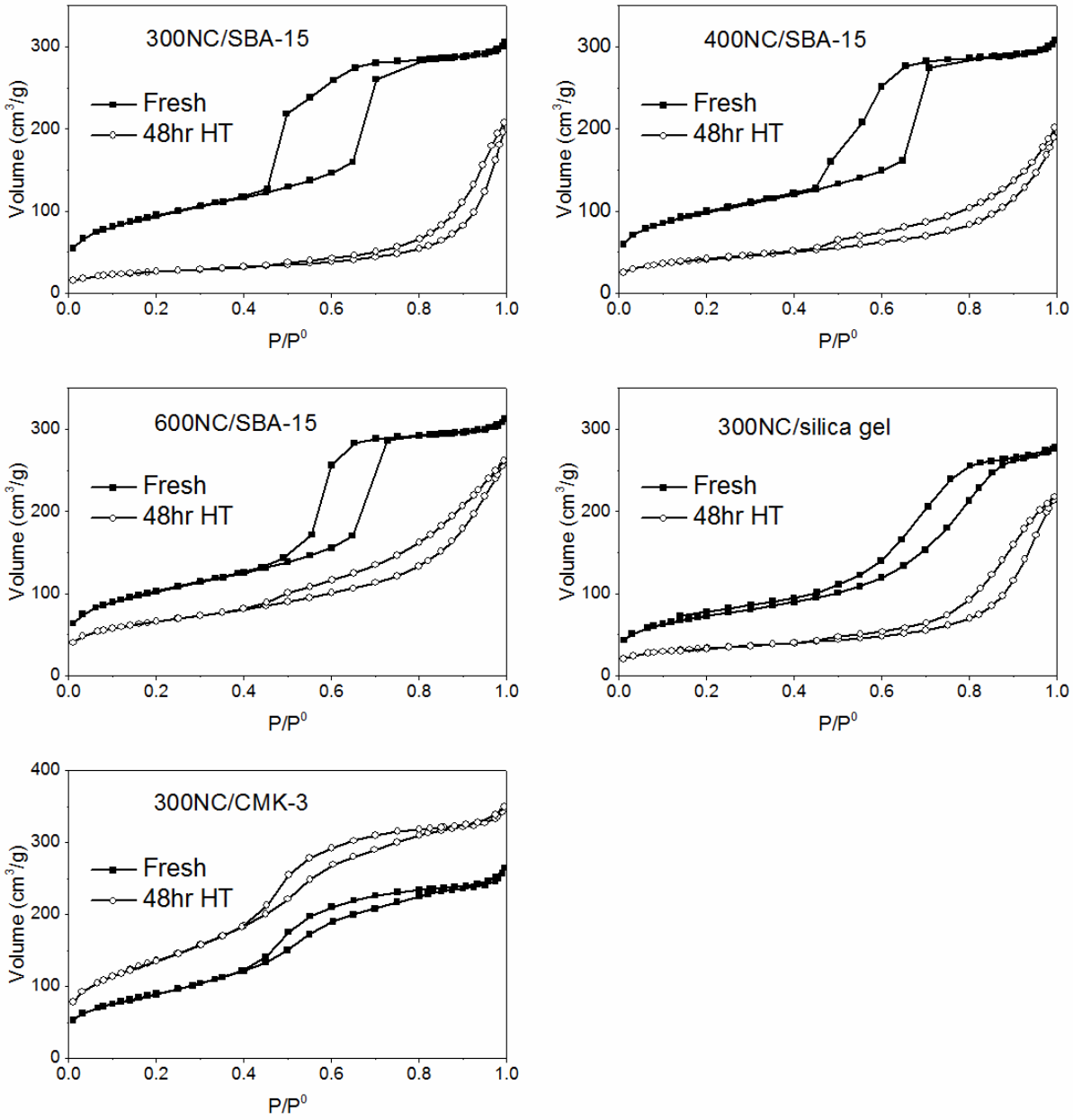

Figure S3.1. Nitrogen physisorption isotherms of 300NC/SBA-15, 400NC/SBA-15, 600NC/SBA-15, and 300NC/silica gel before and after 48 h of hydrothermal treatment. (HT: hydrothermal treatment)

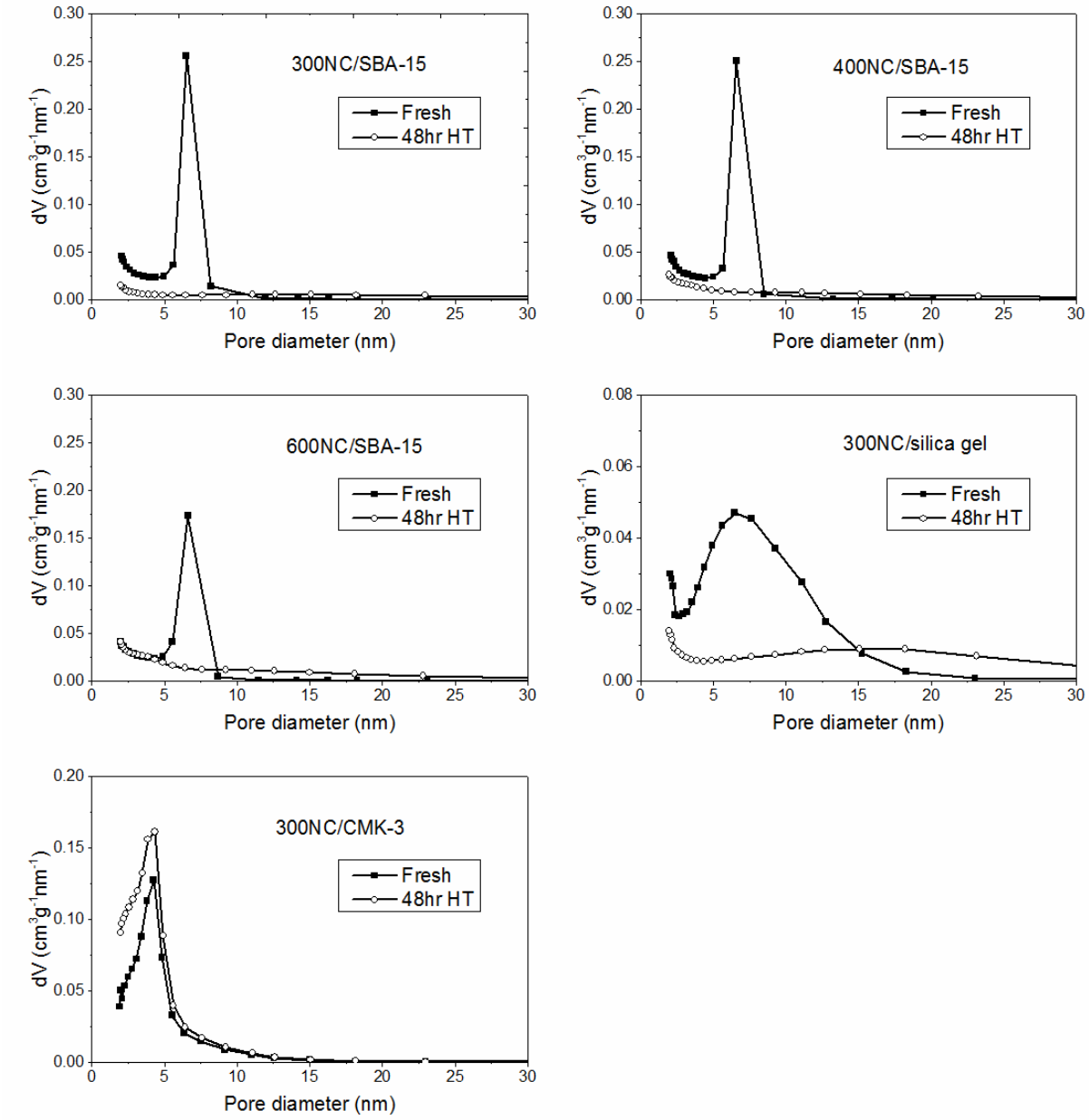

Figure S3.2. Pore size distribution curves of 300NC/SBA-15, 400NC/SBA-15, 600NC/SBA-15, 300NC/silica gel, and 300NC/CMK-3 before and after 48 h of hydrothermal treatment. (HT: hydrothermal treatment)

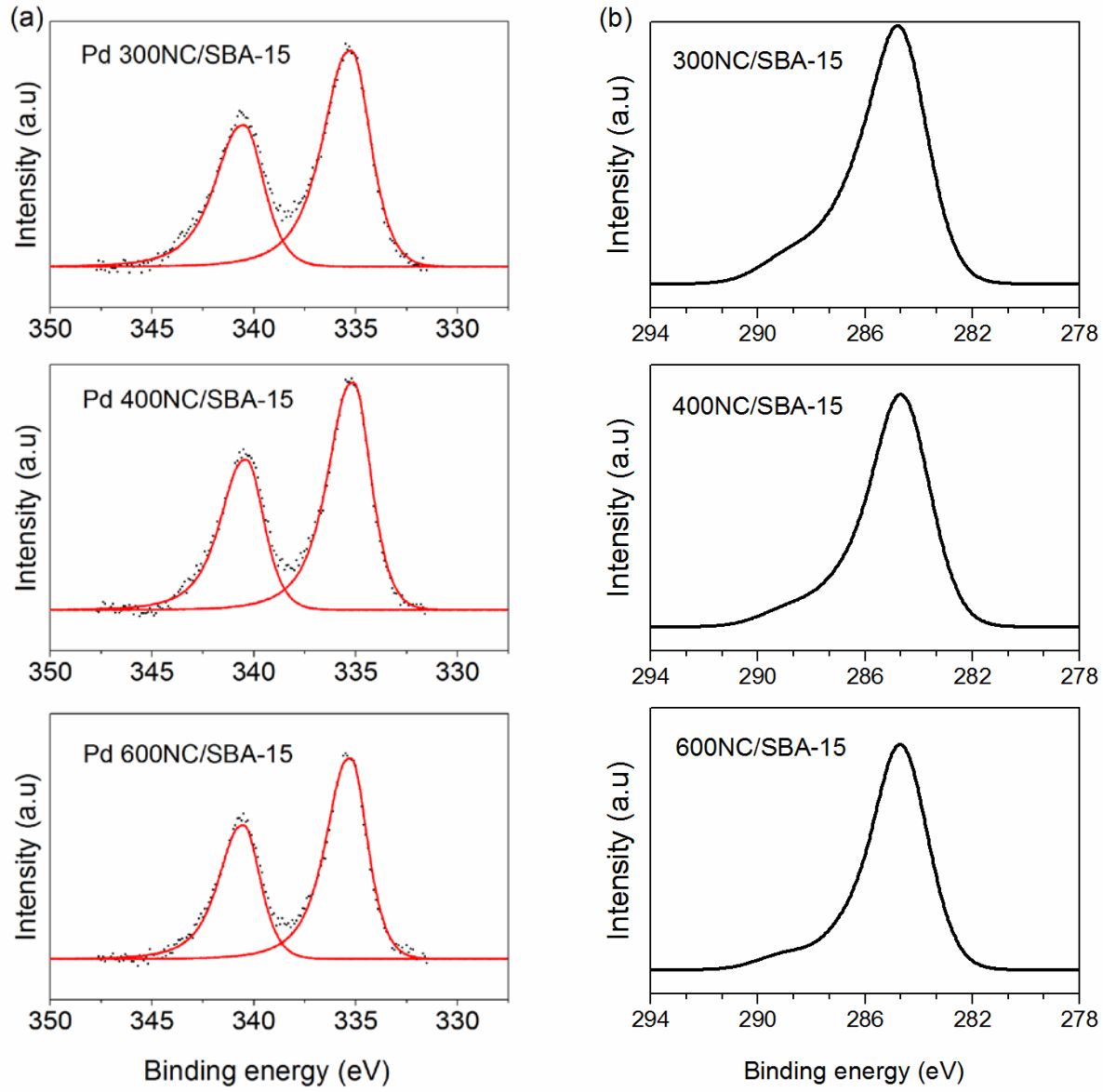

Figure S3.3. Pd 3d XPS (a) and C1s (b) spectra of Pd 300NC/SBA-15, Pd 400NC/SBA-15, and Pd 600NC/SBA-15.

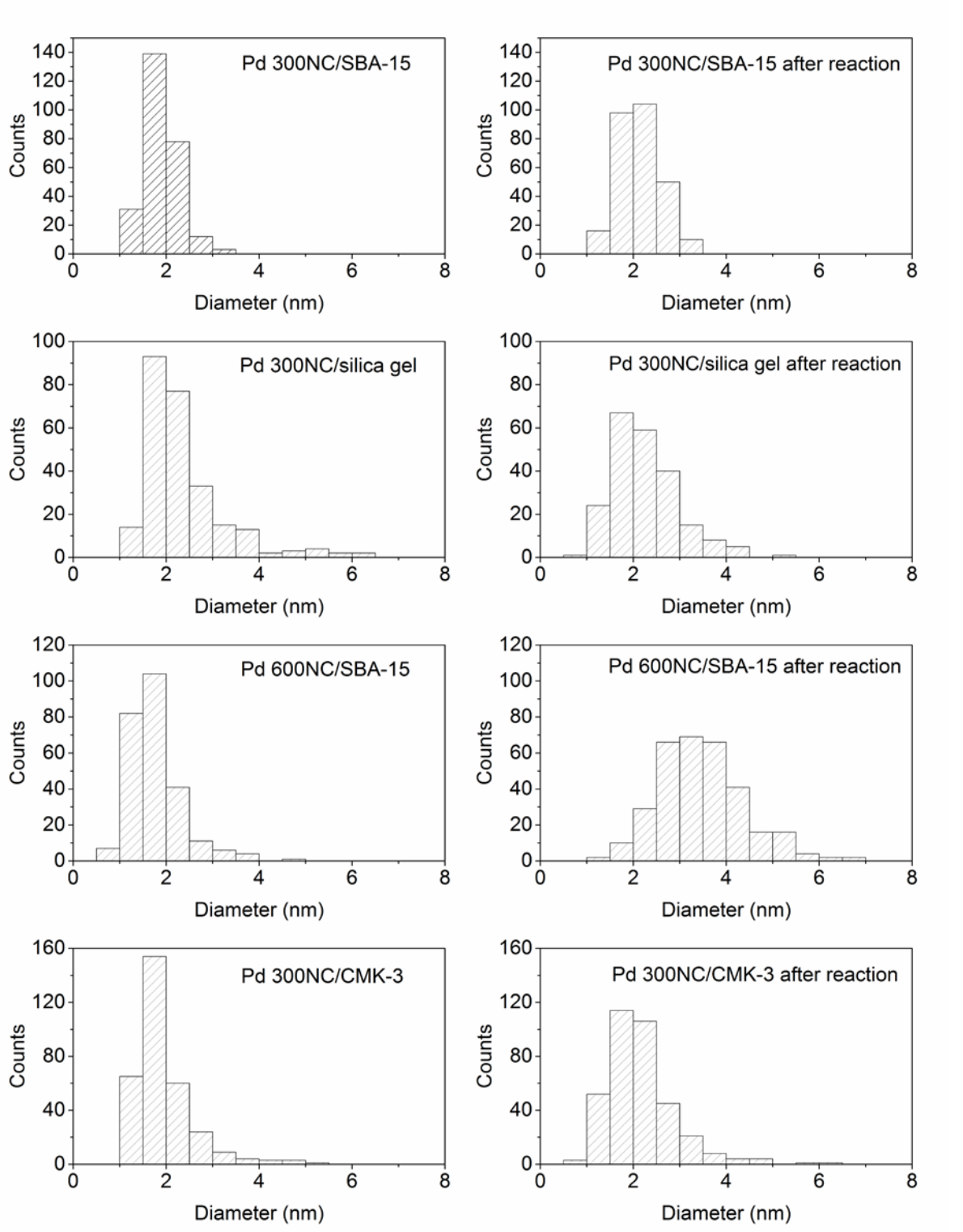

Figure S3.4. Particle size distribution of Pd 300NC/SBA-15, Pd 300NC/silica gel, Pd 600NC/SBA-15, and Pd 300NC/CMK-3 before and after 48 h of flow reaction.

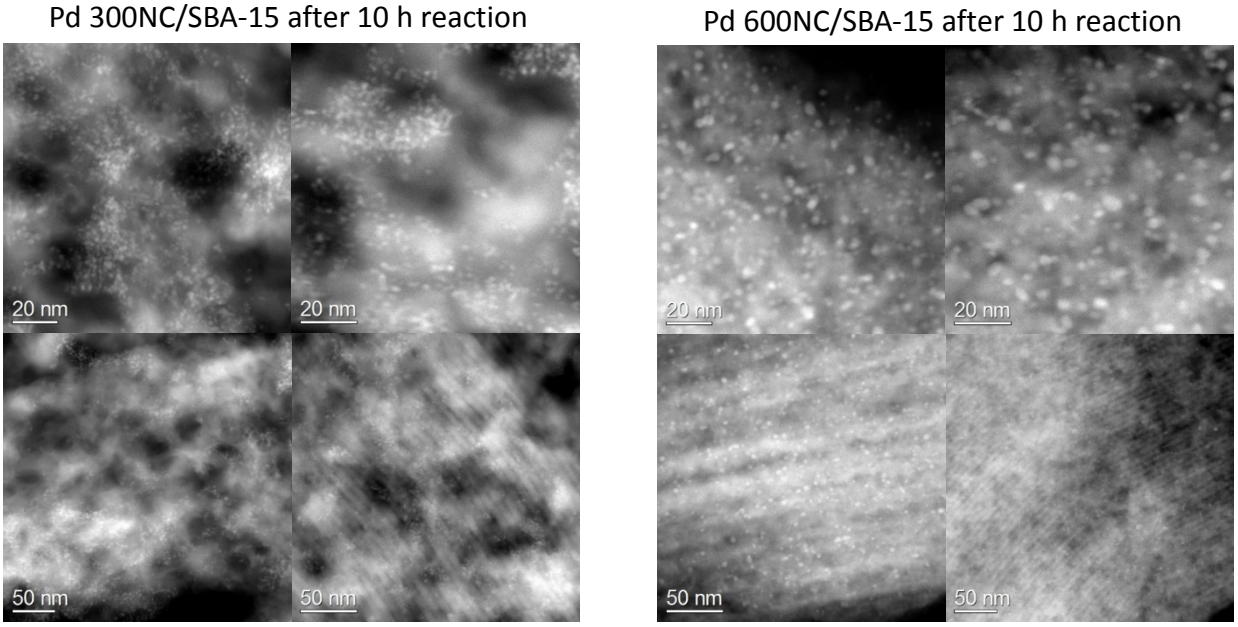

Figure S3.5. HAADF-STEM images of Pd 300NC/SBA-15 and Pd 600NC/SBA-15 after 10 h of flow reaction at 130°C and 750 psi H_2.

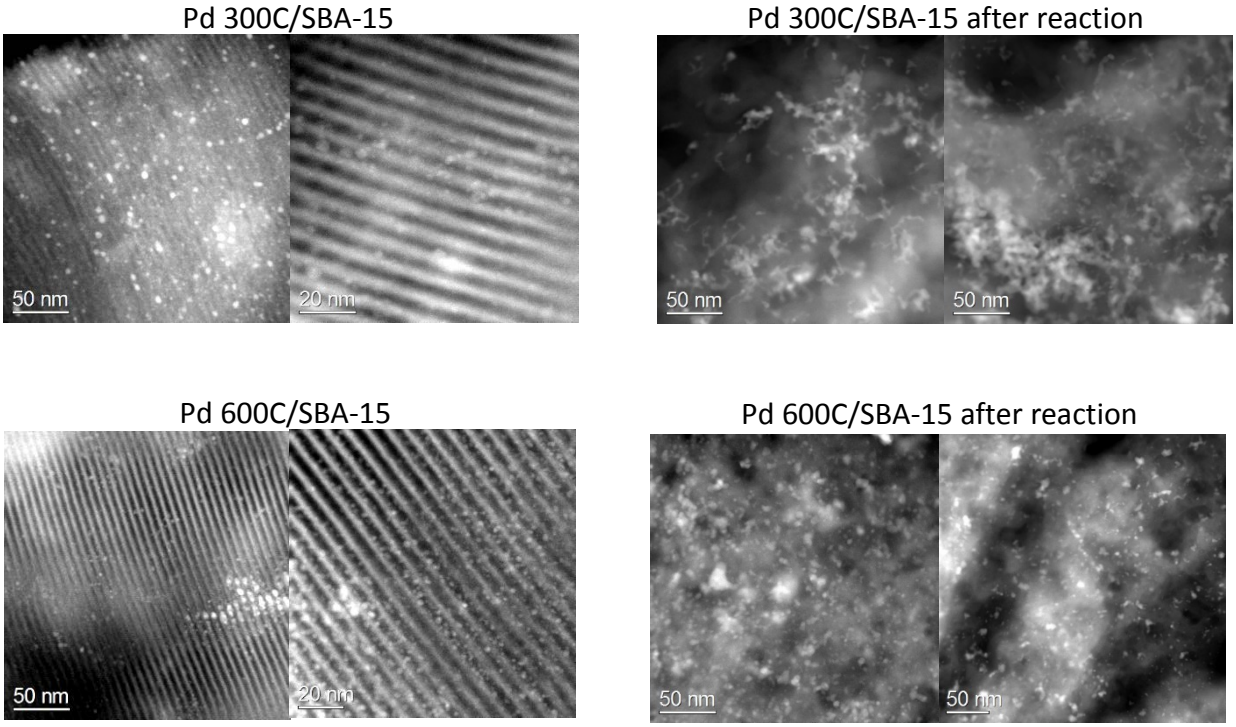

Figure S3.6. HAAFD-STEM images of Pd 300C/SBA-15 and Pd 600C/SBA-15 before and after 48 h of flow reaction.

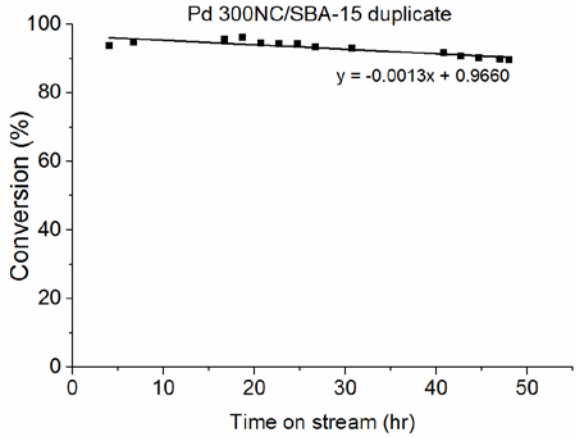

Figure S3.7. Duplicate of continuous flow hydrogenation of furfural on Pd 300NC/SBA-15 at 130°C and 750 psi H_2 for 48 h.

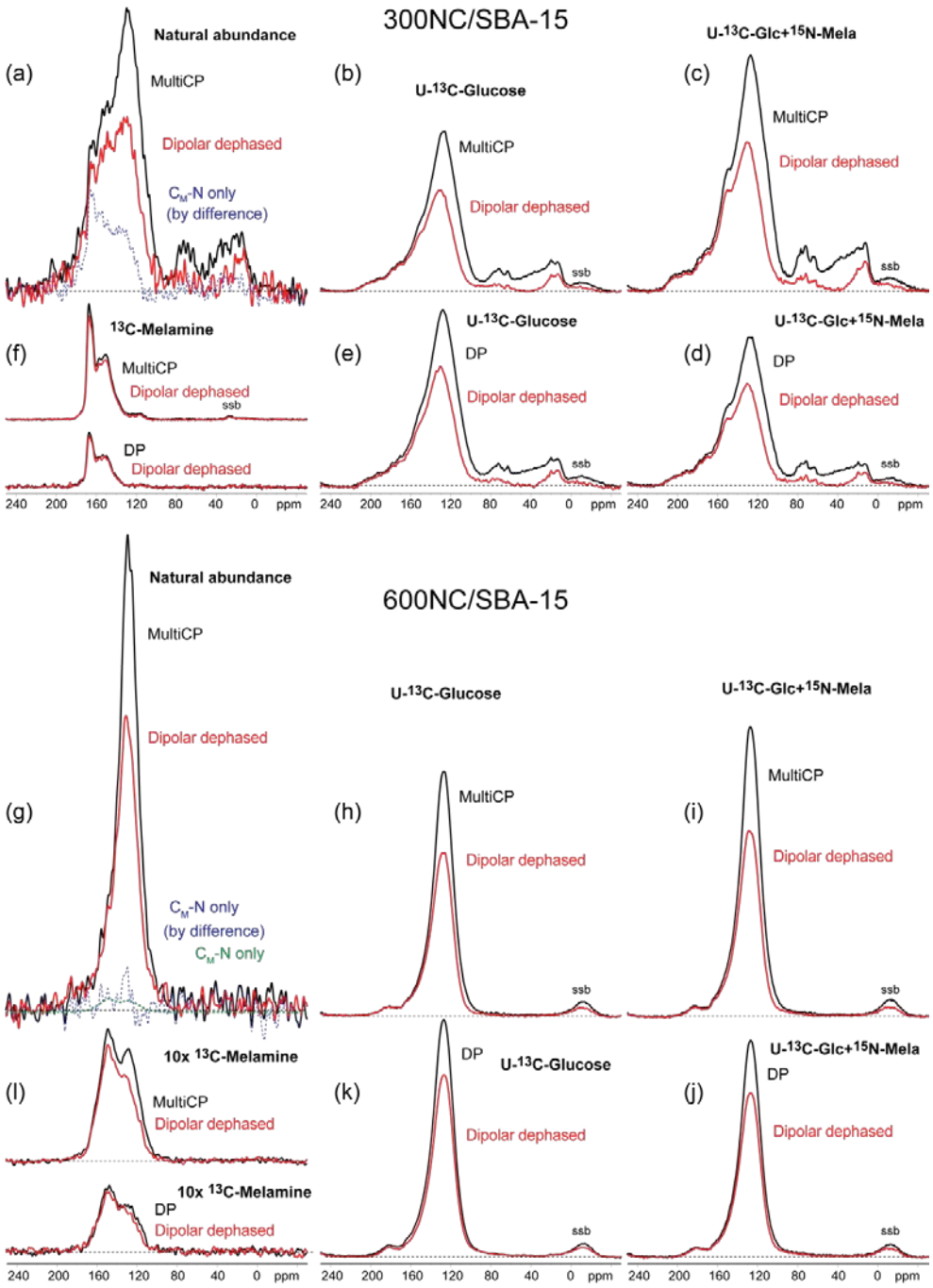

Figure S3.8: Overview of quantitative ^{13}C NMR spectra of several NC/SBA-15 materials made with different isotopic enrichments. Spectra are scaled to correct for sample mass, the ^{13}C enrichment level, and the number of scans. (a-e) Spectra of three nominally equivalent 300NC/SBA-15 samples: (a) Unlabeled (^{13}C in natural abundance of 1.1%), (b) from ^{13}C-enriched glucose. Top row: multiCP, bottom row: DP spectra. (f) Spectra of carbon in 300NC/SBA-15 derived from melamine. (g-k) Spectra of three nominally equivalent 600NC/SBA-15 samples. Top row: multiCP, bottom row: DP spectra. (l) Spectra of carbon in 600NC/SBA-15 derived from melamine.

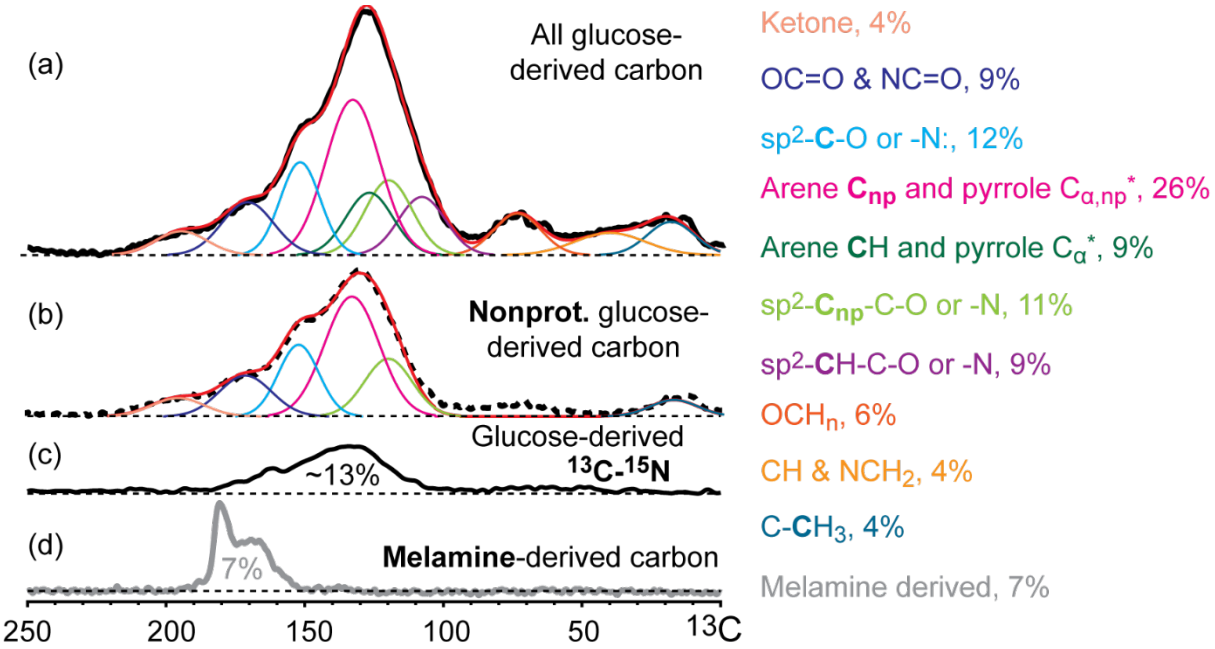

Figure S3.9. Deconvolution of the (a) DP and (b) DP/dipolar dephasing ^{13}C NMR spectra of NC300/SBA-15 made from ^{13}C-enriched glucose. (c) Corresponding $^{13}C^{1}$ REDOR difference spectrum of the same material, showing signals of glucose-derived carbon bonded to ^{15}N. The deconvolution of this spectrum is shown in Figure 3.6. (d) Corresponding spectrum of carbon derived from ^{13}C-enriched melamine.

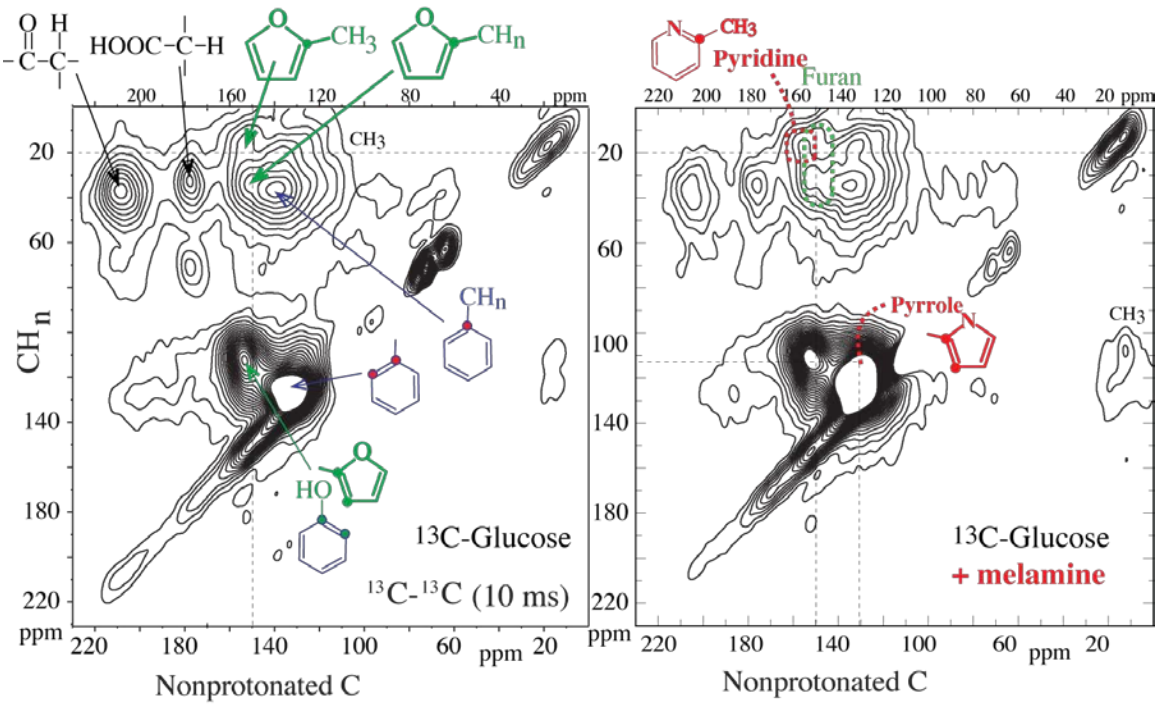

Figure S3.10. Spectrally edited ^{13}C-^{13}C correlation spectra of (left) a reference material 300C/SBA-15 made from ^{13}C-glucose without melamine and (right) 300NC/SBA-15 made from ^{13}C-glucose and melamine. Signals of protonated C along the vertical axis are correlated with peaks of nonprotonated C and mobile segments along the horizontal axis. Additional distinctive signals of C near N in the material with melamine are labeled.

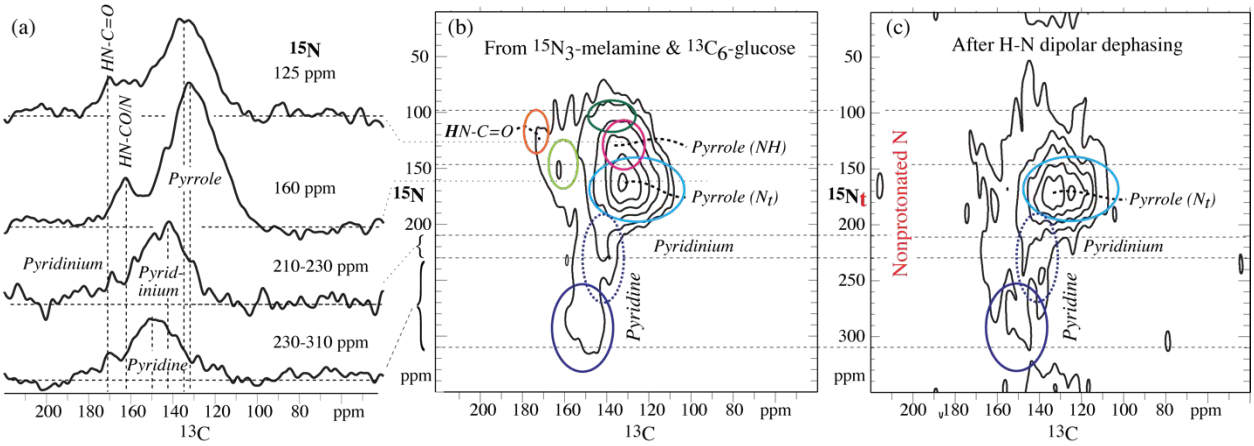

Figure S3.11. ^{15}N-^{13}C correlation spectra of 300NC/SBA-15 made from ^{13}C-glucose and $(^{15}NH_2)_3$-labeled melamine, facilitating assignment of the ^{15}N NMR signals. (a) Cross sections along the ^{13}C dimension, at 125 and 160 ppm in the ^{15}N dimension and partial projections from 210-230 ppm and 230-310 ppm, as indicated (top to bottom), from the 2D spectrum in b). (b) Contour plot of the full 2D spectrum. (b) Corresponding spectrum of nonprotonated N_t, after suppression of NH by recoupling of the ^{15}N-^{1}H dipolar interaction. The color coding of the ellipses is the same as in Figure 3.6.

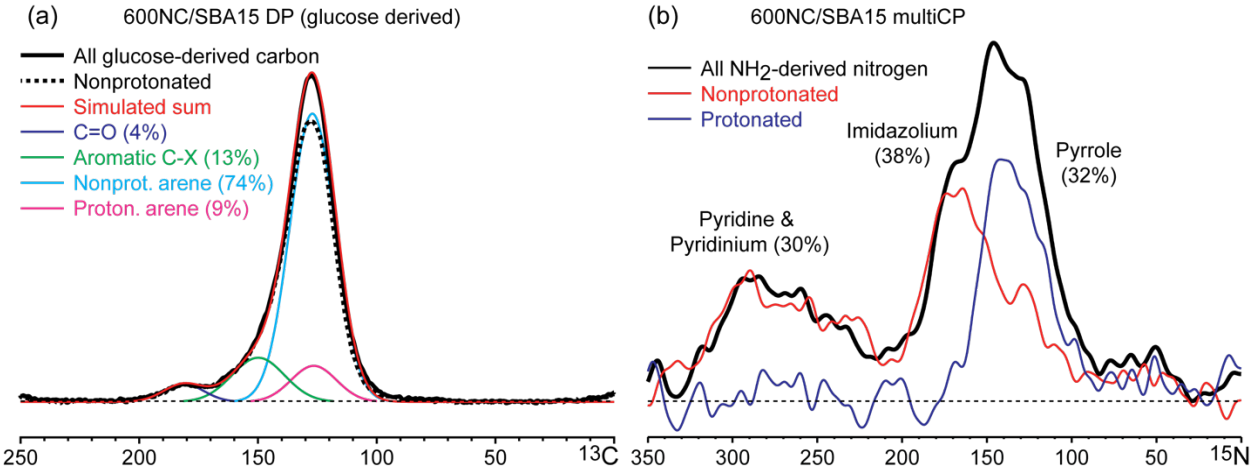

Figure S3.12. Analysis of NMR spectra of 600 NC/SBA-15. (a) Deconvolution of the quantitative DP ^{13}C NMR spectrum. (b) Assignments of multiCP and multiCP/dipolar dephasing ^{15}N spectra and fractional peak areas of the main components.

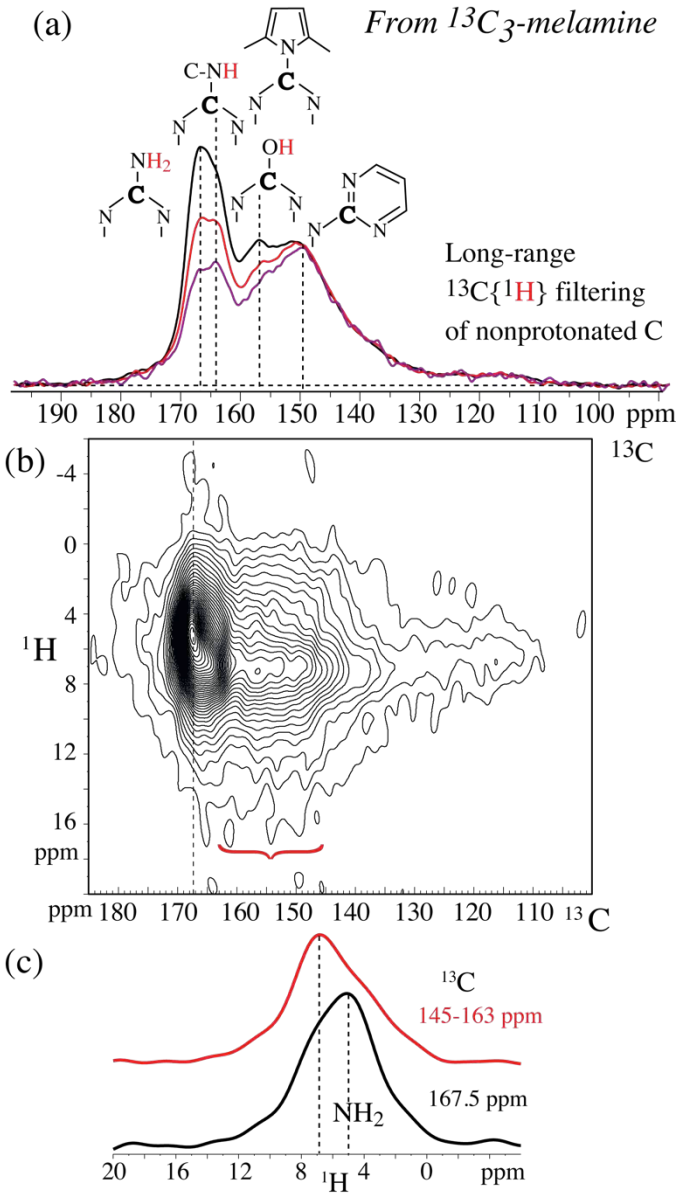

Figure S3.13. Spectra of 300NC/SBA-15 made from unlabeled glucose and $^{13}C_3$-melamine. (a) Series of ^{13}C NMR spectra after long-range ^{13}C dipolar dephasing, reflecting relative proximity of carbons to the nearest protons: full (top trace), after 0.38 ms (middle trace, red line), and after 0.57 ms (bottom trace, purple line) of long-range ^{13}C dipolar dephasing. The spectra after dephasing have been scaled vertically by 1.9 and 4.4, respectively, to match in intensity at 150 ppm. The assignment of the signal at 164 ppm to carbon bonded to NH is confirmed by ^{1}H-^{13}C NMR, see Figure S3.5. (b) ^{1}H-^{13}C heteronuclear correlation spectrum and (c) cross sections/partial projections. The distinct difference in the ^{1}H chemical shift associated with ^{13}C resonating at 164 vs. 167.5 ppm is attributed to NH vs. NH_2.

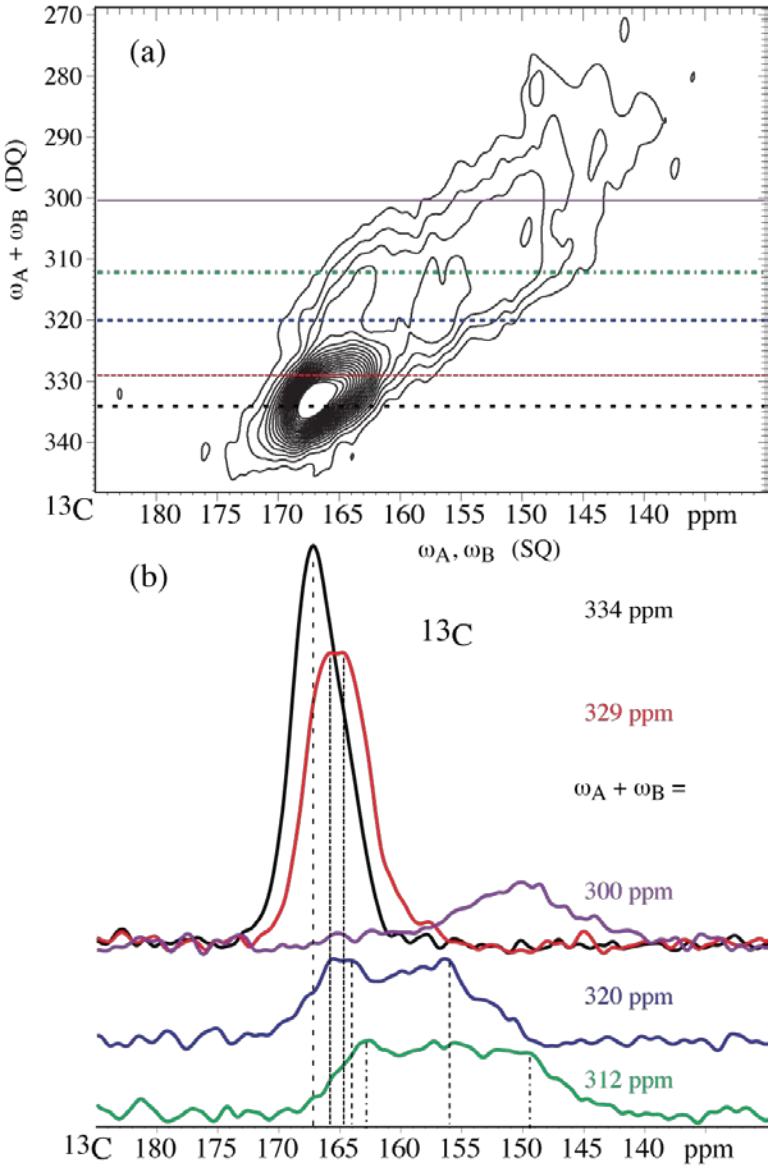

Figure S3.14. DQ/SQ ^{13}C-^{13}C correlation of 300NC/SBA-15 made from unlabeled glucose and $^{13}C_3$-melamine. (a) 2D spectrum; (b) Cross sections at the double-quantum frequencies indicated in a), with correlated frequencies indicated by vertical lines.

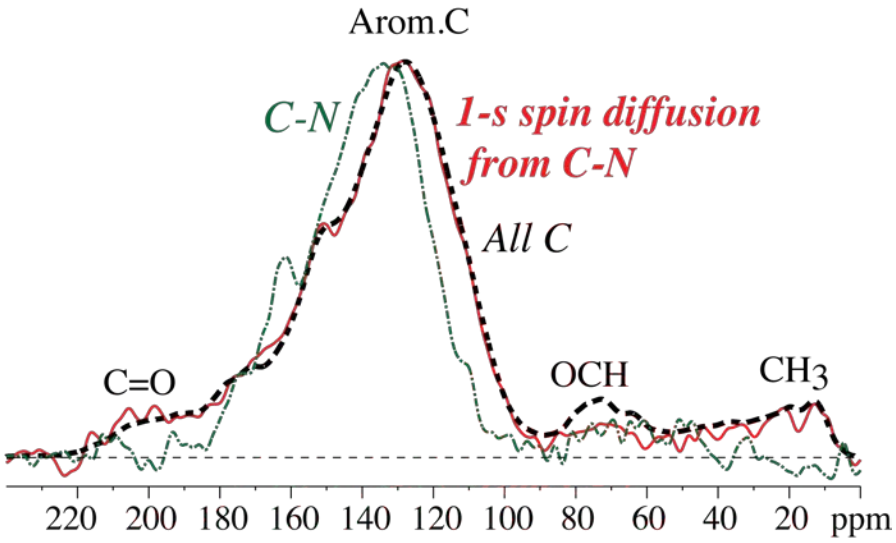

Figure S3.15. Spectra of ^{13}C near ^{15}N in 300 NC/SBA-15, on the 0.2-nm and 3-nm scales. Dash-dotted green line: ^{13}C bonded to ^{15}N. Solid red line: same after 1 s of ^{13}C spin diffusion, showing signal of ^{13}C within ~3 nm from ^{15}N. The signal of all C measured under the same conditions is shown for reference (dashed line), scaled to match the largest peak.

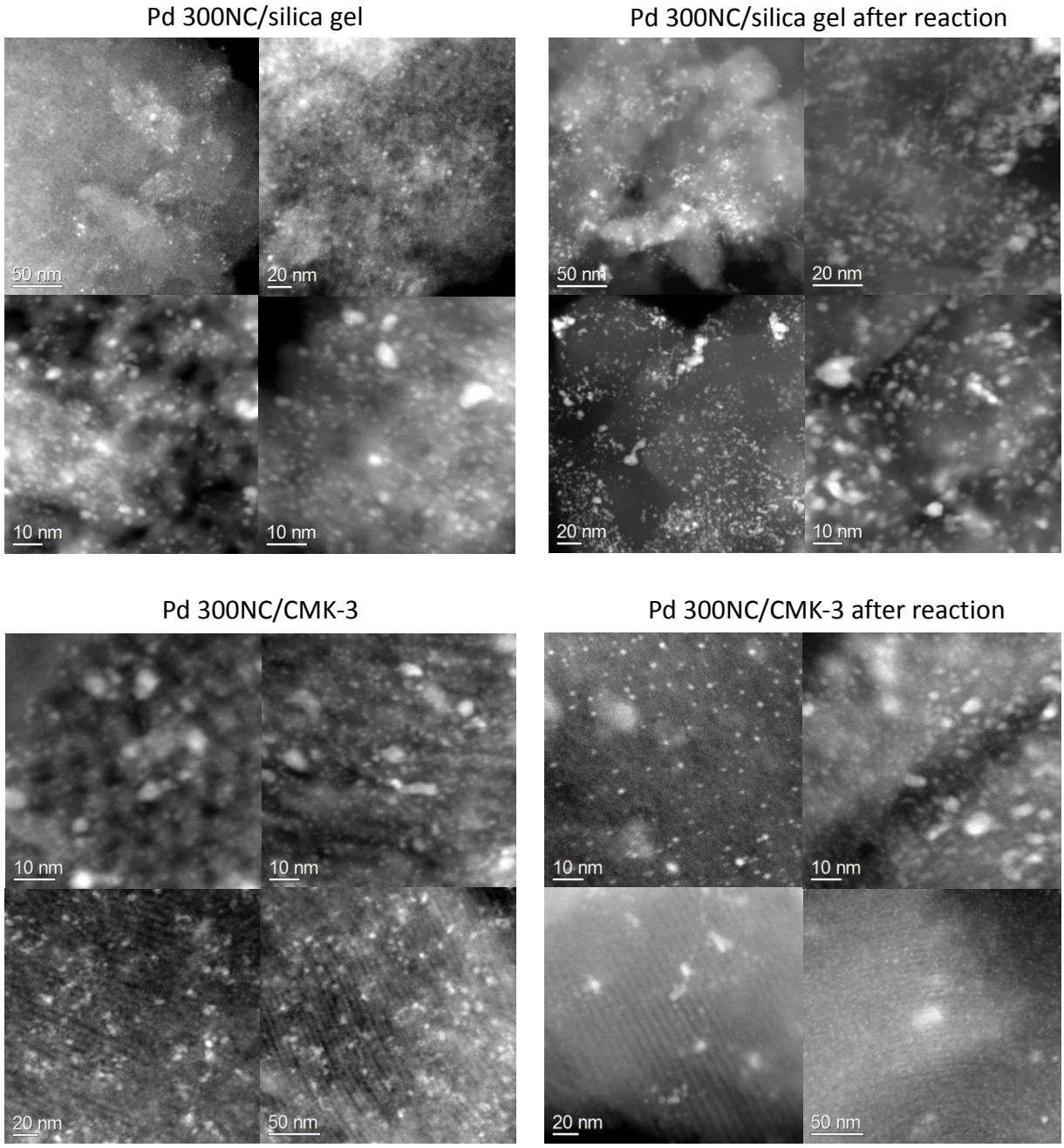

Figure S3.16. HAADF-STEM images of Pd 300NC/silica gel, and Pd 300NC/CMK-3 before and after 48 h of continuous flow reaction.

^{15}N functional group analysis of fresh 300NC/SBA-15 by NMR

In 300NC/SBA-15, the major form of nitrogen (ca. 27%) is substituted N of pyrrole or imidazolium resonating near 170 ppm, with nitrogen not bonded to hydrogen, according to the spectral editing in Figure 3.5b and S3.11c. The corresponding major ^{13}C resonance near 130 ppm, representing the maximum in the 2D spectra in Figure 3.6 and S3.11, confirms the assignment. Pyrrole without substitution of N has a similar aromatic ^{13}C chemical shift but the nitrogen resonates near 125 ppm and is bonded to ^{1}H (see Figure S3.11b,c). The structure suggests that the nitrogen has detached from the triazine ring of melamine.

The next most abundant form of nitrogen is pyridinium, visible as a broad shoulder around 220 ppm in Figure 3.5b and 3.6, and merging with the pyridine/pyrimidine band, which extends out to 320 ppm. The pyridinium nitrogen presumably remains bonded to melamine carbon after glucose has "wrapped around" the melamine amine. Pyrimidine could form by incorporation of triazine nitrogen and carbon of melamine and an NH_2 nitrogen into a pyrimidine ring (see Figure S3.13a). By contrast, pyridinic N would have to be incorporated individually into glucose-derived aromatic rings, originating from NH_2 detached from the melamine (strictly speaking, triazine) ring and being replaced by OH (^{13}C resonance near 157 ppm in Figure S13).

Amide and NCX_2 groups, with around 10% abundance each and with N mostly bonded to hydrogen, are best identified by the partially resolved peaks of their carbon atoms in Figure 3.6. While amide, NC=O, linking various aromatic or aliphatic units is a major component of lower-temperature Maillard reaction products, it is apparently less abundant in the synthesis at 300^{o}C. NCX_2 groups with a distinctive ^{13}C resonance near 160 ppm contain sp^2-hybridized carbon bonded to nitrogen and two other heteroatoms, of which one is double-bonded. Ureido (N_2C=O) and, less likely, guanidino (N_2C=N) groups are typical examples.[1] The melamine N_2C=N

resonances also fall into this category, but formation of a melamine ring from glucose carbon seems relatively unlikely. The ~160 ppm ^{13}C and 130-160 ppm ^{15}N chemical shifts also match those of cyclic amides with a bond to another sp^2-hybridized carbon, for instance in uracil.[1]

References

1. X. W. Fang, J. D. Mao, R. M. Cory, D. M. McKnight and K. Schmidt-Rohr, *Magn. Reson. Chem.*, 2011, **49**, 775-780.

CHAPTER 4. DEACTIVATION OF CARBON SUPPORTED PT AND RU CATALYSTS IN HYDROTHERMAL REACTIONS

A paper to be submitted

Jiajie Huo,[ab] Hien N. Pham,[bc] Yan Cheng,[ab] Luke T. Roling,[a] Abhaya K. Datye,[bc] Brent H. Shanks[ab*]

[a]Department of Chemical and Biological Engineering, Iowa State University, Ames, Iowa 50011, United States

[b]Center for Biorenewable Chemicals, Iowa State University, Ames, Iowa 50011, United States

[c]Department of Chemical and Biological Engineering and Center for Microengineered Materials, University of New Mexico, Albuquerque, New Mexico 87131, United States

Abstract

As aqueous phase biomass conversion offers the promise to produce fuels and chemicals in a more sustainable way, catalyst stability is crucial for further research and industrial application. While structural collapse of the support, sintering and leaching of the metal phase have been reported in the literature as the main deactivating mechanism, here we demonstrate carbon deposition and metal sintering as important deactivating mechanisms for carbon supported Pt catalysts in aqueous phase hydrogenation reactions of 2-pentanone. More importantly, a mild regeneration method involving air oxidation at 200 °C and H_2 reduction at 180 °C led to full recovery of the catalytic activity. The regeneration method was also applied to Ru catalysts with a full recovery of activity. This can serve as a suggestive method to regenerate the catalyst for hydrothermal reactions. A new carbon supported Pt and Ru catalyst derived from polyaniline was also synthesized and showed some unique properties.

4.1 Introduction

Hydrothermal reactions or aqueous-phase reactions have been explored extensively as biomass conversion to chemicals or fuels typically occurs in water at high temperatures.[1-4] Aqueous phase reactions include hydrogenation, reforming, hydrodeoxygenation, oxidation, and other reactions.[3,5-9] Using water as an inexpensive, green and clean solvent is more sustainable and environment-friendly compared with organic solvents.[10,11] The catalysts used for these aqueous-phase reactions are usually supported metal catalysts, especially noble metal catalysts. While active and selective catalysts are being developed for aqueous phase biomass-related reactions, the hydrothermal stability is one of the key challenges to be solved for scale-up and industrial applications.[12-14] On one hand, the common catalyst supports such as silica, alumina, zeolite, zirconia, and high surface area titania, which are used widely in gas phase reactions or organic solution reactions, are not stable under aqueous-phase reaction conditions.[15-17] On the other hand, the supported metal particles may undergo deactivation by poisoning, fouling (carbon deposition), sintering, leaching, or restructuring under hydrothermal conditions.[15,17-24] While the deactivation caused by carbon deposition and poisoning may be reversible by regeneration, the other deactivation mechanisms are usually irreversible. Carbon deposition and poisoning can also be avoided by process optimization such as removal of the poisoning compounds and dilution of feedstock.[13,25] The overall stability of the catalysts, including the support and metal nanoparticles, need to be considered.

Efforts to improve the hydrothermal stability of the catalyst have been explored, such as carbon coating and overcoating either by chemical vapor deposition or in an aqueous solution.[15,19,26] Bimetallic catalysts, strong metal-support interaction and atomic layered deposition (ALD) coating have also been shown to be effective.[5,27-29] Silica deposition on

Pt/Al_2O_3 was found to improve the stability of the catalyst, but still resulted in deactivation as the alumina support transformed to the boehmite phase along with sintering of Pt nanoparticles.[30] Alkyl phosphonate coating was also found to be effective for improving the hydrothermal stability of gamma-alumina.[31]

While carbon supports are generally stable under hydrothermal conditions without any further modifications, the prevention of metal particles from leaching and sintering on a stable carbon support remains a challenge. Sintering has been the major cause for irreversible catalyst deactivation both in gas phase and liquid phase reactions. Various approaches have been used to reduce the sintering of the metal phase either by shape control or by using bimetallic nanoparticles for gas phase reactions.[32] However, the sintering mechanism under hydrothermal conditions may be different from those under gas phase conditions. From our previous study, carbon surface chemistry such as oxygen and nitrogen heteroatoms have been shown to improve the stability of Pd nanoparticles under hydrothermal conditions.[33,34] While keeping the desired carbon surface functional groups for anchoring metal nanoparticles shows promise, we have been working on embedding the metal nanoparticles into the carbon support to further stabilize these nanoparticles. The common synthesis methods of supported metal catalysts, such as impregnation (incipient wetness impregnation and wet impregnation), reductive deposition, precipitation, colloidal, ion exchange, and strong electrostatic adsorption (SEA), always directly incorporates the metal precursors onto the catalyst support materials.[35-37] As a result, the stability of metal nanoparticles usually depends on the metal-support interaction, including electronic and geometric effects, which are likely to be affected by the carbon surface chemistry and particle sizes. Coatings of supports have been used to modify the support surface chemistry and protect the support materials from collapse under hydrothermal conditions.[15,19,27,38] Coating has also

been used to deposit selectively onto undesired low-coordinated Pd, Cu, and Pt sites, such as edges or steps, which are more prone to to coke formation, sintering and leaching.[29,39-41] Inspired by different coatings on supports using aqueous phase condensation or ALD, we proposed that by carefully controlling the carbon coating, the metal nanoparticles might be embedded within a support material, resulting in a stable catalyst.

Here, we demonstrated that using a polyaniline (PANI) coated carbon supported metal catalyst showed stable activity, while the commercial Pt AC and synthesized Pt XC72R catalysts showed deactivation in a continuous flow reactor. We found both carbon deposition and Pt sintering to be the major deactivating mechanisms. By using PANI coating, the PANI coated carbon was selective in interacting with the Pt sites that were more prone to carbon deposition under reaction, thus yielding a stable activity. A mild regeneration method composed of air oxidation at 200 °C and H_2 reduction at 180 °C resulted in full recovery of the catalytic activity. STEM analysis confirmed that some Pt sintering occurred on the catalyst, but the regeneration steps helped to some extent redisperse the metal nanoparticles. Further study on Ru catalyst also confirmed the carbon deposition as the major deactivating mechanism and that the regeneration method was able to recover the activity.

4.2 Experiment Section

4.2.1 Catalyst Synthesis

The carbon black, XC72R (Cabot), was used as received. Incipient wetness impregnation of aqueous H_2PtCl_6 solution was used to synthesize 1%Pt XC72R followed by drying at 80 °C in an oven overnight and reduction in H_2 at 300°C for 2 hr. For the synthesis of 1% Pt PANI XC72R, carbon black XC72R (800 mg) was mixed with aniline (200 mg) in 100 mL 1M HCl solution and sonicated for 1 hr. A 490 mg of $(NH_4)_4S_2O_8$ was dissolved in 100 mL of 1M HCl

solution and added into the mixture of the carbon black and aniline dropwise with vigorous stirring at room temperature. The solution was quickly transferred into a water chiller, where temperature was kept at 4 °C for 18 hr. After polymerization, the PANI coated XC72R was vacuum filtered, washed with water, and dried in an oven at 80 °C for 6 hr. An appropriate amount of H_2PtCl_6 was dissolved in water and loaded onto the PANI coated XC72R after drying by incipient wetness impregnation method with 1 wt% Pt loading. The catalyst was dried in an oven at 80 °C overnight and then carbonized at 600 °C for 1 hr in a flow of UHP argon in a ceramic boat sitting inside a furnace tube with a ramp of 10 °C/min. To compare with 1% Pt PANI XC72R, 1% Pt C XC72R was also made with 1 g of XC72R and 0.5 g of aqueous glucose solution. After stirring at room temperature to evaporate the water, the slurry was dried in an oven at 80 °C. Same incipient wetness impregnation of H_2PtCl_6 and carbonization at 600 °C for 1 hr was used to prepare the catalyst. For the Ru catalyst, $RuCl_3 \cdot xH_2O$ (Sigma-Aldrich, 99.98%) was used to synthesize 1% Ru XC72R and Ru PANI XC72R in the same manner with Pt catalysts.

4.2.2 Hydrothermal Treatment

A known amount of catalyst was added in a PTFE-lined autoclave together with 30 mL of nanopure water. The vessel was put in a furnace set at 170 °C or 200 °C and held at that temperature for certain time. The hydrothermal treatment of the Pt catalyst was performed at 170 °C for 48 hr in accordance with previous methods.[33,34]

4.2.3 Catalyst Characterization

BET surface area analysis by nitrogen physisorption was measured on an ASAP 2020 (Micromeritics) at -196 °C with liquid nitrogen after degassing at 150 °C for 5 hr. Pore volume was determined at a relative pressure of 0.97. The BJH method was used to evaluate the pore

size distribution from the adsorption isotherm. CO pulse chemisorption was performed at 35 °C after reduction in H_2 at 200 °C for 2 hr followed by flushing with UHP argon for 15 min using an ASAP 2920 (Micromeritics) instrument. A stoichiometric factor of 1 was used to calculate metal dispersion. Attenuated total reflectance-Fourier-transform infrared spectroscopy (ATR-FTIR) was performed on a Thermo-Scientific Nicolet iS50 FT-IR instrument with a MCT (Mercury Cadmium Telluride) detector. The catalyst powder was placed on an ATR crystal and pressed by the detector. All the spectra were collected at 4 cm^{-1} resolution with 32 scans. Samples were dispersed in ethanol and mounted on holey carbon grids for examination in a JEOL 2010F 200 kV transmission electron microscope. Images were recorded both in bright field (BF) and high angle annular dark field (HAADF) modes.

4.2.4 Reaction Testing

Aqueous phase hydrogenation of 2-pentanone was performed in a setup described elsewhere.[29] An amount of 40 mg or 20 mg catalyst was loaded in a stainless steel tube (quarter inch O.D.) by quartz wool and silica chips. An HPLC pump (series 1) was used to pump aqueous 2-pentanone (99 %, Sigma-Aldrich) solution (10 g/L), while a mass flow controller was used to control the flow rate of H_2 gas (20 mL/min, 750 psi). Before each run, the catalyst was reduced in a flow of H_2 (200 mL/min, 750 psi) at 180 °C for 30 min. The temperature was kept at the indicated temperature by a heating tape and PID controller. Samples were collected periodically at the bottom of the condenser and analyzed in GC (Angilent 7890A) equipped with an FID detector and a HP-5 ms column. The condenser was cooled by a water chiller set at 4 °C. The molar production of 2-pentanol over the initial 2-pentanone was used as the conversion rate. Carbon balance was usually above 95%, as shown later in the catalytic plots.

4.2.5 Regeneration of Catalysts

The in-situ regeneration of catalysts was performed after stopping the reaction and purging the reactor system with helium for 5 min followed by oxidation in flowing air at 200 °C for 30 min. After purging with helium again for 5 min, the system was switched to hydrogen, and the reduction was done at 180 °C with 750 psi and 200 mL/min H_2 for 30 min. After the reactor temperature changed to the desired temperature, the reaction continued with the described conditions. Ex-situ oxidation of the catalyst was also performed to investigate the change in surface area. For comparison, a known amount of commercial 1% Pt AC was placed in a quartz boat sitting inside a furnace tube with 35 ml/min air at 200 °C for 1, 2, or 3 hr.

4.3 Results

4.3.1 Regeneration of Carbon Supported Pt Catalysts

Polyaniline and carbon materials derived from polyaniline have been reported in electrocatalytic applications due to their good conductivity and ability to stabilize metal nanoparticles.[42-45] The Pt PANI XC72R was synthesized according to the method described by Guo, et al with some modifications.[43] Polyaniline was first coated on the carbon black followed by incipient wetness impregnation of the H_2PtCl_6 precursor as shown in Figure 4.1. Instead of mixing the Pt precursor and polyaniline together, coating with PANI followed by impregnation may help to expose more Pt particles on the surface without burying them within the carbon coating during the pyrolysis procedure. It is speculated that during carbonization, the Pt particles were partially embedded into the carbon matrix pyrolyzed from PANI, thereby keeping the Pt particles from moving while still exposing the partial surface of Pt particles.

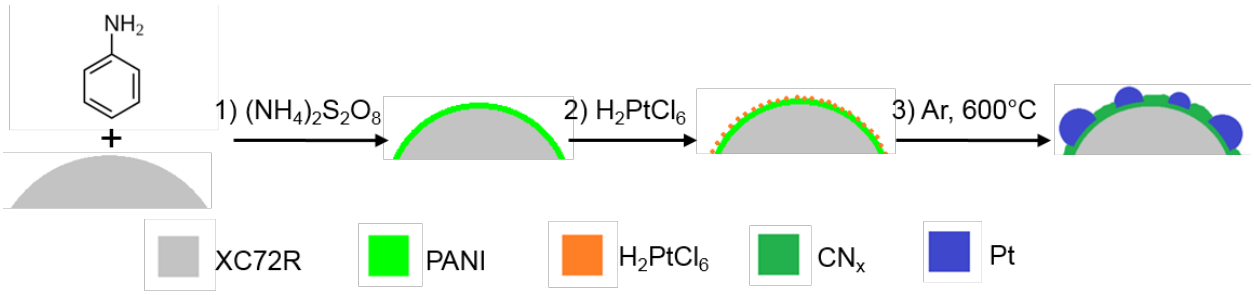

Figure 4.1. Synthesis procedure of Pt PANI XC72R including 1) polymerization, 2) incipient wetness impregnation of H_2PtCl_6, and 3) carbonization at 600 °C in argon for 1h.

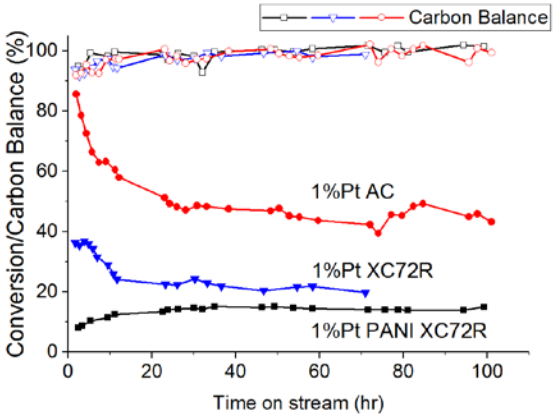

Figure 4.2. Catalytic conversion of 2-pentanone to 2-pentanol at 200 °C, 750 psi and 20 mL/min H_2, 20 mg of catalyst, and 0.08 mL/min 2-pentanone solution flow rate on 1% Pt AC, 1% Pt XC72R, and 1% Pt PANI XC72R.

Aqueous phase hydrogenation of 2-pentanone in a continuous flow reactor as shown in Figure 4.2 demonstrated the catalytic conversion of 1% Pt AC decreased from 85% to around 50% conversion in the first 30 hr and stabilized for the next 70 hr. A similar trend was observed when using 1% Pt XC72R with a decrease in activity in the first 12 hr and stabilization over longer time on stream. On the other hand, 1%Pt PANI XC72R showed an increase in conversion during the first 10 hr and remained stable for the next 90 hr on stream.

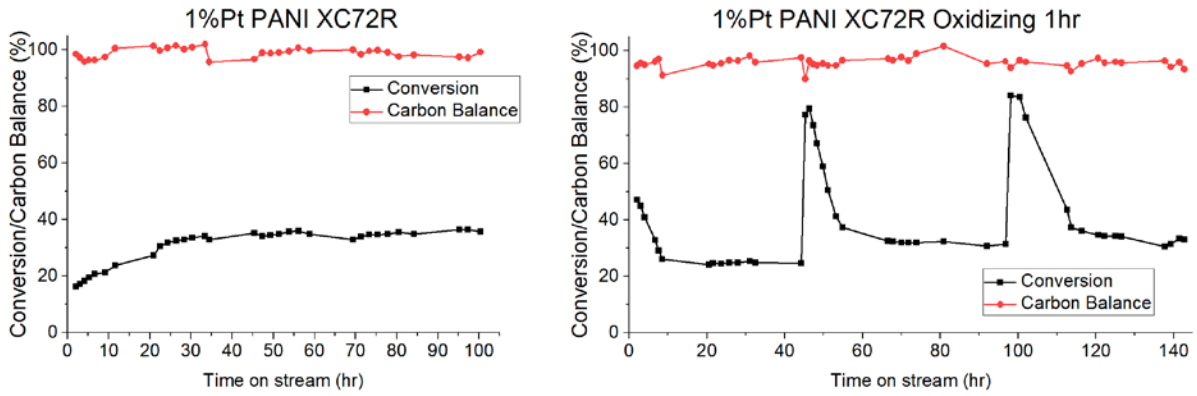

Figure 4.3. Catalytic conversion of 2-pentanone to 2-pentanol at 180 °C, 750 psi and 20 mL/min H_2, 40 mg of catalyst, and 0.08 mL/min 2-pentanone solution flow rate on 1% Pt PANI XC72R without regeneration (left) and with regeneration (right). The catalyst was first oxidized in-situ in air at 200 °C for 1 hr and then reduced in-situ in H_2 at 180 °C for 30 min before the reaction. The subsequent in-situ regeneration at 45 and 97 hr composed of oxidation in air at 200 °C for 30 min and reduction in H_2 at 180 °C for 30 min. Between switching gases, nitrogen gas was used to purge the reactor system.

To determine the role of PANI coating on XC72R, a simple in-situ regeneration was performed on the 1% PANI XC72R. A controlled reaction was performed at 180 °C in Figure 4.3a. A similar activation period was observed in the beginning and then stabilized around 34% conversion for the next 80 hr on stream. The catalytic activity of 1% Pt PANI XC72R was higher at 180 °C in Figure 4.3a than the activity at 200 °C in Figure 4.2 due to different reaction residence time as half of the catalyst was used at 200 °C. In Figure 4.3b, the initial catalytic activity after the in-situ oxidation and reduction was higher than the stabilized conversion in Figure 4.3a. The conversion dropped from 48 to 24% in 10 hr and remained around 24% for 35 hr. After regeneration at 45 hr, the catalytic conversion was recovered and was even higher than the initial conversion. The catalytic conversion then decreased from around 80% to 32% and remained around 32%. A second regeneration around 100 hr showed the same recovery in catalytic activity with subsequent decrease and final stabilization around 33% conversion. This conversion is similar to the controlled experiment without regeneration in Figure 4.3a, indicating

that the carbon from PANI coating can deposit selectively onto Pt sites that are more prone to deactivation, likely in a similar manner where alumina coating preferentially blocked the undesired low-coordinated Pd or Pt sites, which are more prone to coke formation.[39-41] During regeneration, the deposited carbon from PANI on these undesired Pt sites are removed and thus activity was recovered. However, during subsequent reaction, the undesired Pt sites are once again deposited by carbon resulting in the loss of high activity. The other Pt sites are not prone to carbon deposition, as the catalytic activity didn't decrease to zero and remained around 34% conversion. Different from ALD method on supported metal catalysts, where supported metal catalyst was first synthesized followed by ALD coating and then activation by high temperature treatment to produce porosity,[29,39] the Pt PANI XC72R synthesis incorporated metal precursor introduction and embedding metal particles by coating in a few simple steps.

To investigate the deactivating mechanism of the Pt catalyst without PANI coating, a same regeneration procedure was performed on commercial 1% Pt AC and as-prepared 1% Pt XC72R. Regeneration of 1% Pt AC in Figure 4a after 100 hr showed a complete recovery of the catalytic activity to 84% conversion. However, it quickly deactivated in the same manner. A second regeneration on 1% Pt AC showed a same regenerating effect on the catalyst, but with a higher initial conversion (90% conversion) followed by a stable conversion. Similarly, in Figure 4b the catalytic activity of 1% Pt XC72R after the first regeneration was even higher than the fresh catalyst. To test if the catalytic activity kept increasing after each regeneration, 6 regenerations were performed on the catalyst with a total time on stream of 450 hr. Subsequent regenerations showed that the catalyst was regenerable, and the peak conversion was around 90% and then stabilized around 55% conversion. This indicates that carbon deposition is the main deactivation mechanism of the catalyst. The catalyst is fully regenerable to the initial or

even higher activity state. It is likely that carbon deposition also originates at the undesired Pt sites, which showed a decrease at the beginning of reaction and after regeneration. Once these undesired Pt sites are covered with carbon deposits, the catalytic conversion showed consistent stability possibly due to the remaining Pt sites, which are resistant to carbon deposition.

The different adsorption energies of small molecules on the low-coordinated sites versus high-coordinated sites have been demonstrated especially for late transition metals such as Co, Ni, Cu, Rh, Pd, Ag, Ir, Pt, and Au in many theoretical works.[41,46-50] C_2 hydrocarbon species were found to be more strongly adsorbed on the low-coordinated Pt sites (edges and steps) compared with high-coordinated sites (terrace).[41,50] CO, O and OH functional groups also adsorb more strongly on these low-coordinated sites on various metals.[47-49] Therefore, it is possibly the undesired Pt sites are low-coordinated sites such as corners, edges and steps, while the remaining sites are high-coordinated sites. It was anticipated that the carbon species from aniline during the Pt PANI XC72R carbonization process likewise strongly adsorbed on the carbon-deposits-producing low-coordinated sites. The highly-coordinated sites were still available for reaction, thus showing a stable catalytic activity time on stream. During reaction, the carbon species likely from reactant or product also strongly adsorbed on the low-coordinated sites and deactivated these sites, while the high-coordinated sites still showing a stable activity after the rapid deactivation.

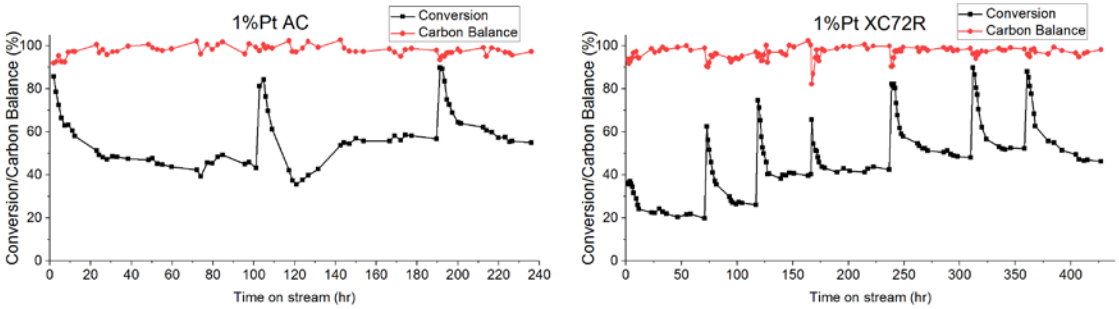

Figure 4.4. Catalytic conversion of 2-pentanone to 2-pentanol at 200 °C, 750 psi and 20 mL/min H_2, 20 mg of catalyst, and 0.08 mL/min 2-pentanone solution flow rate on 1% Pt AC (4a) and 1% Pt XC72R (4b).

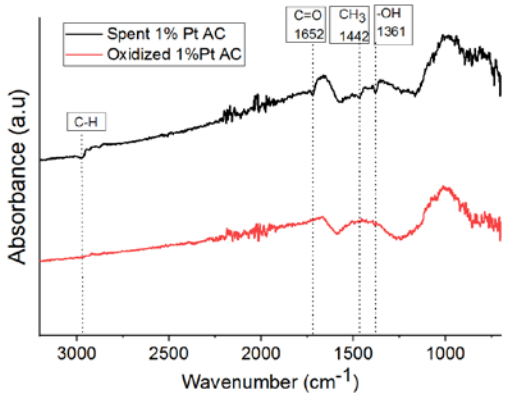

Figure 4.5. ATR-FTIR spectra of spent 1% Pt AC before and after oxidization in air at 200 °C for 30 min. Fresh 1% Pt AC was used as background and subtracted from both spectra.

Figure 4.5 showed the ATR-FTIR spectra of spent 1% Pt AC before and after oxidation in air. There are some chemical species deposited on the spent catalyst before oxidation, suggested by C=O and –OH functional groups on catalyst surface. These signals disappeared after oxidation in air at 200 °C for 30 min. This again confirmed carbon deposition forming on the catalyst and that mild regeneration in air can remove the carbonaceous species deposited on the catalyst surface. It also confirmed that the species of carbon deposits on catalyst are not coke (polyaromatic carbon), which are commonly observed in high-temperature gas phase hydrocarbon reactions.

The BET surface area of the three carbon supported Pt catalysts all showed small increase after 48 hr of hydrothermal treatment shown in Figure 4.6. The physisoption isotherms of the catalysts before and after hydrothermal treatment (Figure S4.1) showed similar curves, indicating the relative stability of the support structure under hydrothermal conditions. The small increase in surface area for carbon materials has also been reported in the literature under similar hydrothermal treatment conditions.[51] There was a small increase in the surface area both after oxidation and after hydrothermal treatment in Figure 4.7. The carbon structure was still maintained as evidenced by the minimum change in surface area and physisorption isotherms (Figure S4.2 and S4.3). This demonstrated that carbon materials are stable under extended hydrothermal conditions, and mild regeneration or oxidation didn't change the carbon structure significantly. While it was previously demonstrated that metal oxides like silica, alumina and zeolite lost surface area dramatically even after a shorter hydrothermal treatment, carbon materials are relatively stable under hydrothermal and mild regeneration conditions.

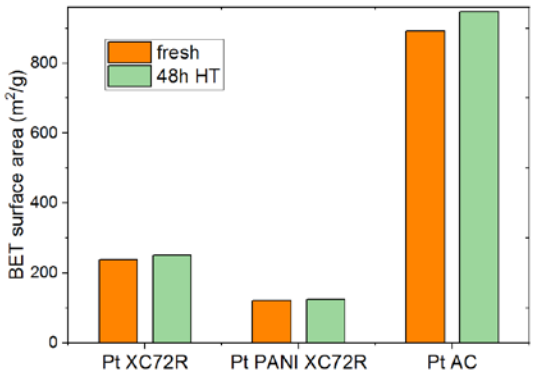

Figure 4.6. BET surface areas of 1% Pt XC72R, 1% Pt PANI XC72R, and 1% Pt AC before and after 48 hr of hydrothermal treatment in water at 170 °C.

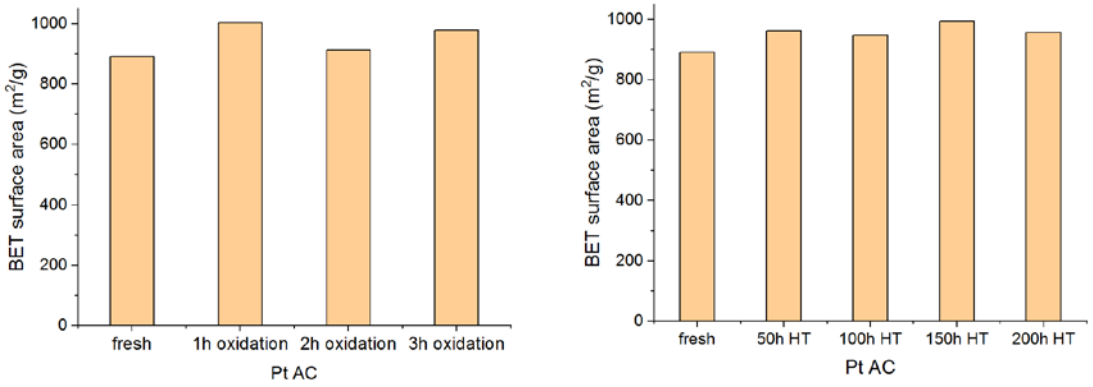

Figure 4.7. BET surface areas of 1% Pt AC after ex-situ oxidation in air at 200 °C for 1 , 2 , and 3 hr(left); and after hydrothermal treatment at 200 °C for 50 , 100 , 150 , and 200 hr (right).

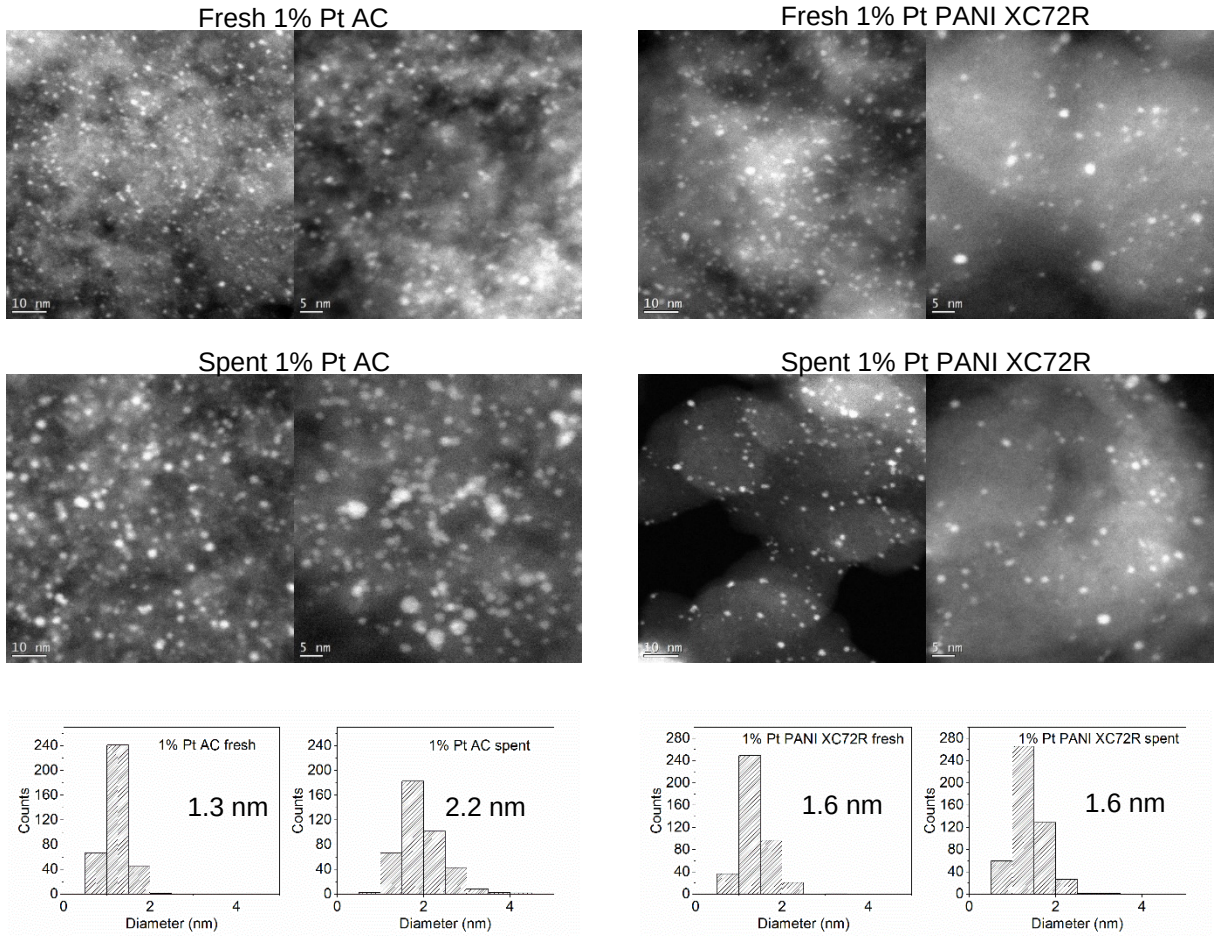

Figure 4.8. HAADF-STEM images and Pt particle size distribution of fresh and spent 1% Pt AC (left) and 1% Pt PANI XC72R (right) after 240 hr of aqueous phase hydrogenation of 2-pentanone described in Figure 4.2 and 4.4. The insert number is surface average particle size of Pt.

The surface averaged Pt particle size from STEM analysis on fresh and spent 1 % Pt AC and 1% Pt XC72R showed Pt particles sintered from 1.3 nm to 2.2 nm and 1.3 nm to 1.5 nm respectively (Figure 4.8 and S4.6). The similar particle sizes should have similar activity for the 2-pentanon hydrogenation reaction; however, the initial activity for 1% Pt XC72R is much lower than that for 1% Pt AC. It is possibly that Pt nanoparticles were initially decorated with carbon in Pt XC72R, and that only by oxidation in air was the decorative carbon removed and better activity was observed after each regeneration. This observation has been reported in Regalbuto et al. work, where the decorative carbon was found on the carbon supported Pd catalyst and oxidation was able to remove the decorative carbon on the Pd surface.[52] When the decorative carbon was removed, the Pt AC and Pt XC72R catalysts showed similar peak (90%) and stabilized (55%) conversions at the end of the run. The decorative carbon is, however, different than the carbon deposition occurring during the reaction in the form of coking. The carbon deposition appears to only occur at the undesired Pt sites while the decorative carbon occurs on the both Pt sites since both stabilizing and peak conversion were improved after regeneration.

Table 4.1. CO chemisorption data of fresh and hydrothermally treated 1% Pt AC, 1% Pt XC72R, and 1% Pt PANI XC72R. HT refers to hydrothermal treatment in water at 170 °C for 48 hr.

Sample name	Fresh			48 hr HT		
	CO uptake/ umol/g	Dispersion/ %	Particle size/nm	CO uptake/ umol/g	Dispersion/ %	Particle size/nm
Pt AC	22.4	44	2.6	15.7	31	3.7
Pt XC72R	16.7	32	3.5	10.9	21	5.3
Pt PANI XC72R	2.6	5	22.0	5.1	10	11.4

HAADF-STEM analysis of the Pt AC catalyst after 240 hr of hydrothermal reaction revealed Pt particles sintered slightly from 1.3 nm to 2.3 nm, as measured from the STEM images shown in Figure 4.8. However, Pt particle size remained the same at 1.6 nm on PANI XC72R in Figure 4.2, in accordance with a stable catalytic activity in Figures 4.2 and 4.3. The

stable Pt particles on PANI XC72R were likely due to the embedded Pt particles into the coating, which can be used as a method to synthesize sinter-resistant supported metal catalyst. This is also confirmed from CO uptake data in Table 4.1, where Pt particles on Pt AC and Pt XC72R sintered to form larger particles. In contrast, CO uptake for Pt PANI XC72R increased after hydrothermal treatment. This is in agreement with the increased activity since the start of the reaction, as shown in Figures. 4.2 and 4.3a. To determine the change in dispersion over the longer reaction run, CO chemisorption was performed on the Pt AC catalyst after successive hydrothermal treatment at 200 °C for up to 200 hr in Table 4.2. The dispersion decreased further during hydrothermal treatment.

Redispersing Pt or Pd nanoparticles in O_2 or Cl_2 gas atmosphere has been reported on zeolite or alumina supported metal catalysts for reforming or oxidation reactions.[53-57] Since the regeneration was performed in air, it is possibly that Pt may have been redispersed during the regeneration steps. To verify this, the sintered Pt AC catalyst after 200 hr of hydrothermal treatment was oxidized in-situ in 10% O_2 in He for 30 min at 200 °C followed by H_2 reduction and CO pulse chemisorption. Table 4.2 shows that after the 1st oxidation, CO uptake increased with some redispersion of the Pt nanoparticles. However, dispersion did not further improve after the 3rd oxidation. Besides, the dispersion was not fully recovered compared to the fresh Pt AC sample. It is possibly that steam generated from residual water inside the reactor during the regeneration helped to further redisperse the Pt nanoparticles, but will require future studies to elucidate this mechanism.

Table 4.2. CO chemisorption data of fresh and hydrothermally treated 1% Pt AC after 50, 100, 150, and 200 hr. HT refers to hydrothermal treatment in water at 170 °C for 48 hr.

Sample name	CO uptake/umol/g	Dispersion/%	Particle size/nm
Pt AC	22.4	44	2.6
Pt AC 50 hr HT	15.6	31	3.7
Pt AC 100 hr HT	13.0	25	4.5
Pt AC 150 hr HT	12.9	25	4.5
Pt AC 200 hr HT	10.2	20	5.7
Pt AC 200 hr HT 1st oxidation	13.6	26	4.3
Pt AC 200 hr HT 2nd oxidation	14.3	28	4.1
Pt AC 200 hr HT 3rd oxidation	14.0	27	4.2

As both carbon deposition and sintering were identified as the deactivation mechanisms in our work, it is hard to distinguish what percentage each mechanism plays. Usually, recovered catalytic activity after catalyst regeneration will be accounted as carbon deposition. However, the regeneration may also redisperse Pt catalyst to some extent, and therefore, we cannot ascribe the deactivation exclusively to carbon deposition. It has been reported in the literature that carbon deposition is relatively fast while metal sintering is slow.[55] The rapid decrease in activity at the beginning of the reaction followed by a stable activity suggest that carbon deposition is the main deactivation mechanism for the Pt AC and Pt XC72R catalysts. However, future studies are necessary to confirm this.

4.3.2 Unique Behavior of Pt PANI XC72R

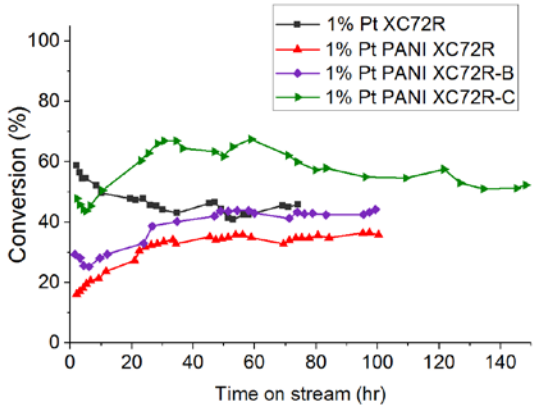

Figure 4.9. Catalytic conversion of aqueous phase hydrogenation of 2-pentanone at 180 °C, 750 psi and 20 mL/min H_2, 40 mg of catalyst, and 0.08 mL/min 2-pentanone solution flow rate on carbon material with different PANI loadings. The XC72R and PANI coating weight ratio is 1% PANI XC72R (XC72R:PANI=4:1), 1% PANI XC72R-B (XC72R:PANI=8:1), 1% PANI XC72R-C (XC72R:PANI=16:1).

The influence of PANI loading was studied in Figure 4.9. With different amounts of PANI, the catalytic conversion of the catalysts showed similar behavior, where an activation period was observed in the beginning and conversion remained the same over longer time on stream. The catalytic stability improved with decreasing amounts of PANI, which was likely due to better Pt dispersion resulting from a larger support surface area of the PANI coated materials in Figure S4.5. The catalytic activity of 1%Pt XC72R in Figure 4.9 at 180 °C is different from the Pt PANI XC72R materials, showing a similar decrease in the beginning and stabilizing over longer time on stream at 200 °C, as shown in Figure 4.2.

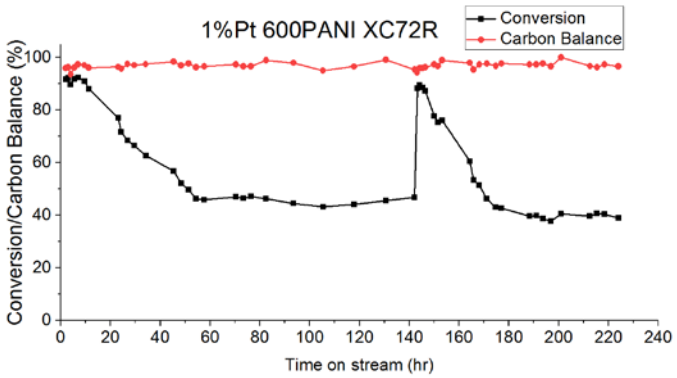

Figure 4.10. Catalytic conversion of aqueous phase hydrogenation of 2-pentanone at 180 °C, 750 psi and 20 mL/min H_2, 40 mg of catalyst, and 0.08 mL/min 2-pentanone solution flow rate on 1% Pt 600PANI XC72R.

To investigate the effects of carbonization, 1% Pt 600PANI XC72R was synthesized, in which PANI XC72R was first carbonized at 600 °C followed by impregnation of Pt precursor and reduction. It was shown that 1% 600PANI XC72R deactivated in a similar manner to 1% Pt XC72R (Figure 4.10). This confirmed the hypothesis that during the synthesis of Pt PANI XC72R, carbon species from PANI coating can deposit selectively onto the Pt sites that are more prone to carbon deposition. If the PANI XC72R support is already carbonized and the carbon coating has a rigid structure, then the carbon coating will not migrate over to the Pt sites during the impregnation of the metal precursor, thus showing a deactivation and stabilization pattern similar to the Pt XC72R and Pt AC catalysts. In this case, we have shown that carbon deposition occurs on Pt AC and Pt XC72R, but with the PANI coating, the Pt PANI XC72R catalyst showed stable conversions due to the selective carbon deposition during the synthesis procedure. To compare with Pt PANI XC72R, a similar Pt C XC72R was synthesized with glucose as the carbon source, and the coated XC72R was synthesized in a similar manner. Figure 4.11 showed a similar activation period in the beginning as the conversion increased from 3% to around 10% and stabilized around 10%. This is about one third conversion of 1% Pt PANI XC72R in Figure 4.3a. It was only after regeneration the catalytic conversion stabilized around 30%. Subsequent

regenerations showed that the conversion was also stable around 30%. It is hypothesized that relatively mobile carbon species from glucose will interact more with the Pt precursor during the pyrolysis and may cover some of Pt metal nanoparticles, while PANI polymer has a relatively more rigid structure and may have more Pt exposed during pyrolysis. This results in a much lower conversion of Pt C XC72R compared with Pt PANI XC72R. However, the carbon coating from glucose can be easily oxidized during the regeneration step, thus exposing more active sites as evidenced by the increase in activity after regeneration. This also confirmed that the rigid carbon structure from PANI helps to stabilize but not completely bury the Pt nanoparticles into the PANI coating.

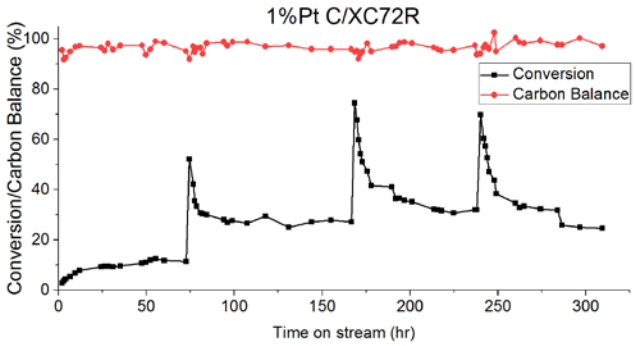

Figure 4.11. Catalytic conversion of aqueous phase hydrogenation of 2-pentanone at 180 °C, 750 psi and 20 mL/min H_2, 40 mg of catalyst, and 0.08 mL/min 2-pentanone solution flow rate on 1% Pt C XC72R.

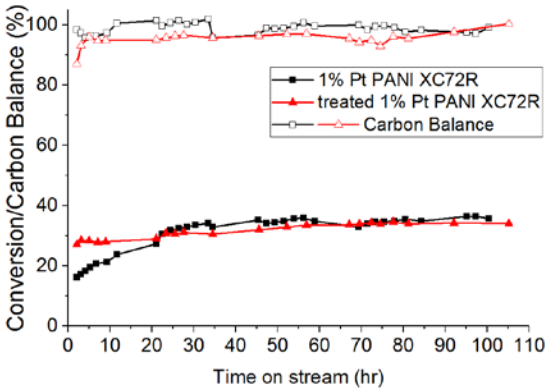

Figure 4.12. Catalytic conversion of aqueous phase hydrogenation of 2-pentanone to 2-pentanol at 180 °C, 750 psi and 20 mL/min H_2, 40 mg of catalyst, and 0.08 mL/min 2-pentanone solution flow rate on 1% Pt PANI XC72R with and without in-situ water treatment at 180 °C for 24 hr.

As can be seen from the figures above, the Pt PANI XC72R and Pt C XC72R catalysts all showed an activation or induction period at the beginning of the continuous flow reactions. After 24 hr of in-situ hydrothermal treatment performed on the catalyst, we were able to get rid of the induction period in Figure 4.12. We hypothesize that it is due to the some of the decorative carbons present on the stable Pt sites, which are then easily washed away by water at high temperatures.

4.3.3 Regeneration of Carbon Supported Ru Catalysts

As Ru is the most used metal for 2-pentanone and levulinic acid hydrogenation reactions, Ru catalysts were synthesized and tested in a similar manner.[58,59] 1% Ru XC72R showed complete conversion at 150 °C, but quickly deactivated to almost 10% conversion in 70 hr (Figure 4.13). After regeneration twice, we were able to recover the activity, but it deactivated even faster after regeneration. Around 120 hr, only in-situ H_2 reduction at 180 °C was used to regenerate the catalyst. However, the conversion only increased from 30% before regeneration to 40% after regeneration. Another regeneration including oxidation and reduction around 140 hr recovered the full activity of the catalyst, revealing that oxidation is required to fully regenerate the catalyst. A similar behavior was found at 100 °C, in which the deactivation of the catalyst was slower. Regeneration resulted in recovery of the catalyst activity, but only a small partial activity was recovered when only H_2 reduction was used to regenerate the catalyst. Further investigation of the catalytic activity at 50 °C revealed a further decrease in both activity and deactivation rate.

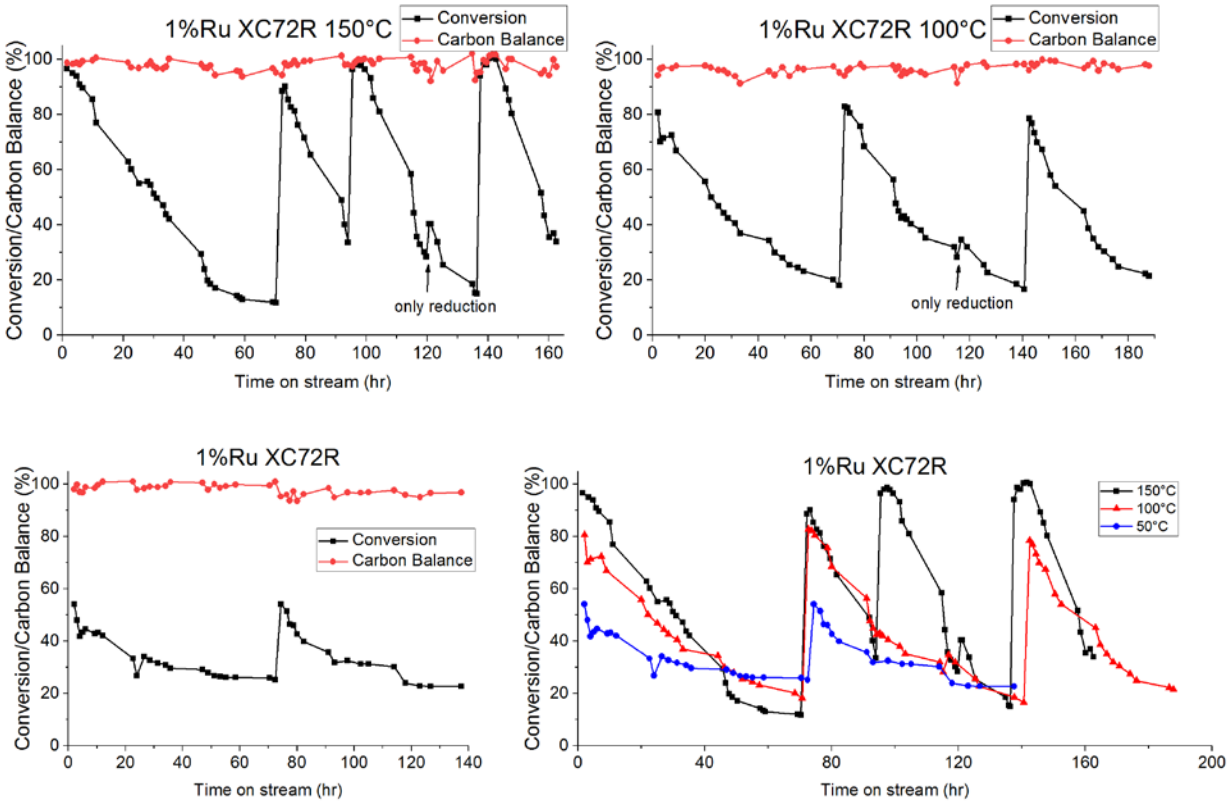

Figure 4.13. Catalytic conversion of aqueous phase hydrogenation of 2-pentanone to 2-pentanol at 750 psi and 20 mL/min H_2, 40 mg of catalyst, and 0.12 mL/min 2-pentanone solution flow rate on 1% Ru XC72R at 150 (a), 100 (b), and 50 °C (c).

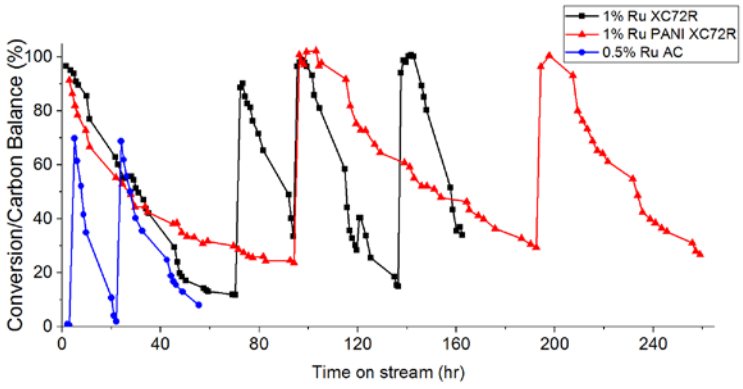

Figure 4.14. Catalytic conversion of aqueous phase hydrogenation of 2-pentanone to 2-pentanol at 150 °C, 750 psi and 20 mL/min H_2, 40 mg of catalyst, and 0.12 mL/min 2-pentanone solution flow rate on 1% Ru XC72R, 0.5% Ru AC, and 1% Ru PANI XC72R.

1% Ru PANI XC72R at 150 °C showed a slower deactivation rate than 1% Ru XC72R in

Figure 4.14. The different behavior of Ru and Pt on PANI XC72R is likely due to the different

electrostatic interaction of cationic Ru precursor compared with anionic Pt precursor with PANI coating. Similar deactivation rate was found on the catalyst after each regeneration. To compare with a standard catalyst, commercial 0.5% Ru AC was used to test the activity. Less than 2% conversion was found on the catalyst. A duplicate reaction with another fresh catalyst showed the same inactivity. Following regeneration the catalyst showed a jump to 70% conversion, which then deactivate quickly to 3% in about 20 hr. Another regeneration followed the same trend, further showing the importance of in-situ regeneration to recover the activity of the catalyst.

4.4 Discussion

Table 4.3. Comparison of petroleum process and biomass conversion

	Petroleum process	Biomass conversion
Feedstock	Low oxygen, low water content	Highly oxygenated, high water content
Operating conditions	250-900°C, usually gas phase, or organic phase	<250°C, liquid phase, water or organic solution
Common catalyst	Metal oxides (zeolite, alumina, silica, titania, zirconia, mixed metal oxide)	Some metal oxide (titania), carbon
Deactivation	Sintering, leaching, coke, poisoning	Sintering, leaching, structural change, poisoning, carbon deposition
Carbon deposition	Coke (low oxygen content, highly aromatic or graphitic)	Carbon deposition (high oxygen content, less condensed)
Regeneration	High temperature (400-600 °C) treatment (oxidation, reduction)	Low temperature (200-300 °C) treatment (oxidation, reduction)

Partly due to the different oxygen and water contents in the feedstock, the petroleum process is usually performed in gas phase at high temperatures, while biomass conversion is usually performed in aqueous phase at relatively low temperatures, as shown in Table 4.3. As a

result, common catalysts used for petroleum are usually metal oxides or oxide supported metal catalysts, which have a good thermal stability. While most metal oxides are not stable under hydrothermal conditions, carbon materials showed the promise for application as hydrothermally stable catalyst supports. Besides, the common deactivation mechanisms may be different under hydrothermal conditions as the interaction of water will also participate in the deactivation compared with petroleum process in the gas phase. Coke forming on the catalyst for hydrocarbon reactions are usually aromatic or polyaromatic partly because of the low oxygen content in the feedstock and high temperature conditions.[60] On the other hand, the highly oxygenated biomass feedstock are usually very reactive, and therefore, carbon deposition may occur. However, these carbon deposits are less condensed and still contain high oxygen content compared with coke formed in the petroleum process. As a result, these thermally stable metal oxides are usually regenerated under high temperature oxidation (400-600°C) to burn off coke for gas phase reactions such as alkane dehydrogenation and methane reforming (dry reforming with CO_2 or wet reforming with steam).[61,62] Similarly, high temperature (350 °C) oxidation was also used to regenerate carbon supported metal catalyst.[63] However, for carbon deposits under hydrothermal conditions, this harsh regeneration condition will not only burn off some carbon support itself, but also result in the sintering of the supported metal phase. In our work, we have shown that low temperature (200 °C) oxidation and reduction was able to remove the carbon deposits for hydrothermal reactions while only H_2 reduction cannot fully regenerate the catalyst. In Bond. et al work on Ru AC in aqueous phase hydrogenation of levulinic acid to γ-valerolactone at 50 °C, a partial recovery of activity was observed after regeneration of only H_2 reduction at 400 °C.[58,59] It is likely the H_2 reduction did not remove all the carbon deposits on the catalyst surface. Besides, the observed sintering of Ru particles is likely a result of high temperature regeneration

instead of reaction at 50 °C, as Regalbuto et al. observed Pd sintering during the reduction at 350 °C compared to 200 °C reduction.[52]

The regeneration method in this work may be applicable to other hydrothermal reactions. Performing stability studies in a continuous flow reactor is preferred as it allows monitoring of catalytic behavior with time on stream. In-situ regeneration can also be performed on the catalyst by purging the reactor system and switching to different gases compared to batch reactors for hydrothermal reactions.

Deactivation and regeneration of catalyst have been studied extensively for gas phase hydrocarbon reactions.[55,64] For hydrothermal biomass conversion reactions, more research is needed for the deactivation and regeneration processes. Detailed mechanistic studies are also needed to further investigate the deactivation mechanism and the amount, chemical composition and location of the carbon deposition, which require advanced in-situ or ex-situ characterizations to accomplish this. Also, bimetallic catalysts may be of interest for future studies to reduce carbon deposition under hydrothermal conditions.

4.5 Conclusion

Carbon deposition and sintering was identified as the main deactivating mechanism on the carbon supported Pt catalysts. Two different active sites were found on Pt catalyst. The undesired type is more prone to carbon deposition while the other type is not prone to carbon deposition under reaction conditions. Pt PANI XC72R showed a stable activity under hydrothermal reactions, which is a result of carbon depositing on the undesired Pt sites during carbonization in the synthesis process. While only H_2 regeneration was not able to fully regenerate the catalyst, a mild regeneration including air oxidation and H_2 reduction led to full

recovery of the catalyst activity on both carbon supported Pt and Ru catalysts. Regeneration is likely to remove the carbon deposits and redisperse the nanoparticles. This mild regeneration is suggested in biomass conversion reactions to study the deactivation mechanism. More extensive studies are needed to elucidate catalyst stability and deactivating mechanisms under hydrothermal conditions.

4.6 Acknowledgement

This work is supported by the Center for Biorenewable Chemicals funded by NSF grant EEC-0813570. We would like to thank Dr. Le Xin for the discussion about using PANI coating on carbon material, Zhanyi Yao for his help in experiment, Professor Andrew Hillier, Russell Mahmood, and Zhiqi Yao for their help with ATR-FTIR analysis. We also thank Professor Jean-Philippe Tessonnier for helpful discussions.

4.7 References

1. Alonso, D. M.; Bond, J. Q.; Dumesic, J. A. *Green Chem.* **2010,** *12* (9), 1493-1513.

2. Luterbacher, J. S.; Alonso, D. M.; Dumesic, J. A. *Green Chem.* **2014,** *16* (12), 4816-4838.

3. Huber, G. W.; Dumesic, J. A. *Catal. Today* **2006,** *111* (1-2), 119-132.

4. Huber, G. W.; Iborra, S.; Corma, A. *Chem. Rev.* **2006,** *106* (9), 4044-4098.

5. Huber, G. W.; Shabaker, J. W.; Evans, S. T.; Dumesic, J. A. *Appl. Catal. B* **2006,** *62* (3-4), 226-235.

6. Kim, Y. T.; Dumesic, J. A.; Huber, G. W. *J. Catal.* **2013,** *304*, 72-85.

7. Lee, J.; Kim, Y. T.; Huber, G. W. *Green Chem.* **2014,** *16* (2), 708-718.

8. Vardon, D. R.; Settle, A. E.; Vorotnikov, V.; Menart, M. J.; Eaton, T. R.; Unocic, K. A.; Steirer, K. X.; Wood, K. N.; Cleveland, N. S.; Moyer, K. E.; Michener, W. E.; Beckham, G. T. *ACS Catal.* **2017,** *7* (9), 6207-6219.

9. Davis, S. E.; Ide, M. S.; Davis, R. J. *Green Chem.* **2013,** *15* (1), 17-45.

10. Sheldon, R. A. *Green Chem.* **2005,** *7* (5), 267-278.

11. Sheldon, R. A. *Chem. Soc. Rev.* **2012,** *41* (4), 1437-1451.

12. Xiong, H.; Pham, H. N.; Datye, A. K. *Green Chem.* **2014,** *16* (11), 4627-4643.

13. Lange, J.-P. *Angew. Chem. Int. Ed.* **2015,** *54* (45), 13186-13197.

14. Schwartz, T. J.; O'Neill, B. J.; Shanks, B. H.; Dumesic, J. A. *ACS Catal.* **2014,** *4* (6), 2060-2069.

15. Pham, H. N.; Anderson, A. E.; Johnson, R. L.; Schmidt-Rohr, K.; Datye, A. K. *Angew. Chem. Int. Ed.* **2012,** *51* (52), 13163-13167.

16. Gardner, D. W.; Huo, J.; Hoff, T. C.; Johnson, R. L.; Shanks, B. H.; Tessonnier, J.-P. *ACS Catal.* **2015,** *5* (7), 4418-4422.

17. Duan, J. Z.; Kim, Y. T.; Lou, H.; Huber, G. W. *Catal. Today* **2014,** *234*, 66-74.

18. Xie, J. H.; Duan, P.; Kaylor, N.; Yin, K. H.; Huang, B.; Schmidt-Rohr, K.; Davis, R. J. *ACS Catal.* **2017,** *7* (10), 6745-6756.

19. Pham, H. N.; Anderson, A. E.; Johnson, R. L.; Schwartz, T. J.; O'Neill, B. J.; Duan, P.; Schmidt-Rohr, K.; Dumesic, J. A.; Datye, A. K. *ACS Catal.* **2015,** *5* (8), 4546-4555.

20. Vardon, D. R.; Sharma, B. K.; Jaramillo, H.; Kim, D.; Choe, J. K.; Ciesielski, P. N.; Strathmann, T. J. *Green Chem.* **2014,** *16* (3), 1507-1520.

21. Piskun, A. S.; de Haan, J. E.; Wilbers, E.; de Bovenkamp, H. H. V.; Tang, Z.; Heeres, H. J. *ACS Sustainable Chem. Eng.* **2016,** *4* (6), 2939-2950.

22. Schwartz, T. J.; Brentzel, Z. J.; Dumesic, J. A. *Catal. Lett.* **2015,** *145* (1), 15-22.

23. Maris, E. P.; Ketchie, W. C.; Oleshko, V.; Davis, R. J. *J. Phys. Chem. B* **2006,** *110* (15), 7869-7876.

24. Xie, J. H.; Falcone, D. D.; Davis, R. J. *J. Catal.* **2015,** *332*, 38-50.

25. Moulijn, J. A.; van Diepen, A. E.; Kapteijn, F. *Appl. Catal. A* **2001,** *212* (1-2), 3-16.

26. Xiong, H.; Schwartz, T. J.; Andersen, N. I.; Dumesic, J. A.; Datye, A. K. *Angew. Chem. Int. Ed.* **2015,** *54* (27), 7939-7943.

27. Lee, J. C.; Jackson, D. H. K.; Li, T.; Winans, R. E.; Dumesic, J. A.; Kuech, T. F.; Huber, G. W. *Energy Environ. Sci.* **2014,** *7* (5), 1657-1660.

28. Lee, J.; Burt, S. P.; Carrero, C. A.; Alba-Rubio, A. C.; Ro, I.; O'Neill, B. J.; Kim, H. J.; Jackson, D. H. K.; Kuech, T. F.; Hermans, I.; Dumesic, J. A.; Huber, G. W. *J. Catal.* **2015,** *330*, 19-27.

29. O'Neill, B. J.; Jackson, D. H. K.; Crisci, A. J.; Farberow, C. A.; Shi, F.; Alba-Rubio, A. C.; Lu, J.; Dietrich, P. J.; Gu, X.; Marshall, C. L.; Stair, P. C.; Elam, J. W.; Miller, J. T.; Ribeiro, F. H.; Voyles, P. M.; Greeley, J.; Mavrikakis, M.; Scott, S. L.; Kuech, T. F.; Dumesic, J. A. *Angew. Chem. Int. Ed.* **2013,** *52* (51), 13808-13812.

30. Liu, F.; Okolie, C.; Ravenelle, R. M.; Crittenden, J. C.; Sievers, C.; Bruijnincx, P. C. A.; Weckhuysen, B. M. *Appl. Catal. A* **2018,** *551*, 13-22.

31. Van Cleve, T.; Underhill, D.; Rodrigues, M. V.; Sievers, C.; Medlin, J. W. *Langmuir* **2018,** *34* (12), 3619-3625.

32. Cao, A.; Lu, R.; Veser, G. *Phys. Chem. Chem. Phys.* **2010,** *12* (41), 13499-13510.

33. Huo, J. J.; Duan, P.; Pham, H. N.; Chan, Y. J.; Datye, A. K.; Schmidt-Rohr, K.; Shanks, B. H. *Catal. Sci. Technol.* **2018,** *8* (14), 3548-3561.

34. Huo, J.; Johnson, R. L.; Duan, P.; Pham, H. N.; Mendivelso-Perez, D.; Smith, E. A.; Datye, A. K.; Schmidt-Rohr, K.; Shanks, B. H. *Catal. Sci. Technol.* **2018,** *8* (4), 1151-1160.

35. Mehrabadi, B. A. T.; Eskandari, S.; Khan, U.; White, R. D.; Regalbuto, J. R. *Adv. Catal., Vol 61* **2017,** *61*, 1-35.

36. Regalbuto, J. *Catalyst Preparation: Science and Engineering*. CRC Press: 2007.

37. Munnik, P.; de Jongh, P. E.; de Jong, K. P. *Chem. Rev.* **2015,** *115* (14), 6687-6718.

38. Pham, H. N.; Pagan-Torres, Y. J.; Serrano-Ruiz, J. C.; Wang, D.; Dumesic, J. A.; Datye, A. K. *Appl. Catal. A.* **2011,** *397* (1-2), 153-162.

39. Lu, J. L.; Fu, B. S.; Kung, M. C.; Xiao, G. M.; Elam, J. W.; Kung, H. H.; Stair, P. C. *Science* **2012,** *335* (6073), 1205-1208.

40. Feng, H.; Lu, J. L.; Stair, P. C.; Elam, J. W. *Catal. Lett.* **2011,** *141* (4), 512-517.

41. Peng, G. W.; Gerceker, D.; Kumbhalkar, M.; Dumesic, J. A.; Mavrikakis, M. *Catal. Sci. Technol.* **2018,** *8* (8), 2159-2174.

42. Chen, S. G.; Wei, Z. D.; Qi, X. Q.; Dong, L. C.; Guo, Y. G.; Wan, L. J.; Shao, Z. G.; Li, L. *JACS* **2012,** *134* (32), 13252-13255.

43. Guo, L.; Jiang, W. J.; Zhang, Y.; Hu, J. S.; Wei, Z. D.; Wan, L. J. *ACS Catal.* **2015,** *5* (5), 2903-2909.

44. Chung, H. T.; Cullen, D. A.; Higgins, D.; Sneed, B. T.; Holby, E. F.; More, K. L.; Zelenay, P. *Science* **2017,** *357* (6350), 479-483.

45. Wu, G.; More, K. L.; Johnston, C. M.; Zelenay, P. *Science* **2011,** *332* (6028), 443-447.

46. Peterson, A. A.; Grabow, L. C.; Brennan, T. P.; Shong, B. G.; Ooi, C. C.; Wu, D. M.; Li, C. W.; Kushwaha, A.; Medford, A. J.; Mbuga, F.; Li, L.; Norskov, J. K. *Top. Catal.* **2012,** *55* (19-20), 1276-1282.

47. Ma, X. F.; Xin, H. L. *Phys. Rev. Lett.* **2017,** *118* (3).

48. Calle-Vallejo, F.; Martinez, J. I.; Garcia-Lastra, J. M.; Sautet, P.; Loffreda, D. *Angew. Chem. Int. Ed.* **2014,** *53* (32), 8316-8319.

49. Roling, L. T.; Abild-Pedersen, F. *ChemCatChem* **2018,** *10* (7), 1643-1650.

50. Watwe, R. M.; Cortright, R. D.; Norskov, J. K.; Dumesic, J. A. *J. Phys. Chem. B* **2000,** *104* (10), 2299-2310.

51. Van Pelt, A. H.; Simakova, O. A.; Schimming, S. M.; Ewbank, J. L.; Foo, G. S.; Pidko, E. A.; Hensen, E. J. M.; Sievers, C. *Carbon* **2014,** *77*, 143-154.

52. Tengco, J. M. M.; Lugo-Jose, Y. K.; Monnier, J. R.; Regalbuto, J. R. *Catal. Today* **2015,** *246*, 9-14.

53. Bartholomew, C. H. *Studies in surface science and catalysis 1997* **1997,** *111*, 585-592.

54. Ono, L. K.; Yuan, B.; Heinrich, H.; Roldan Cuenya, B. *J. Phys. Chem. C* **2010,** *114* (50), 22119-22133.

55. Argyle, M. D.; Bartholomew, C. H. *Catalysts* **2015,** *5* (1), 145-269.

56. Peterson, E. J.; Delariva, A. T.; Lin, S.; Johnson, R. S.; Guo, H.; Miller, J. T.; Kwak, J. H.; Peden, C. H. F.; Kiefer, B.; Allard, L. F.; Ribeiro, F. H.; Datye, A. K. *Nat. Commun.* **2014,** *5*.

57. Trimm, D. L. *Appl. Catal. A* **2001,** *212* (1-2), 153-160.

58. Abdelrahman, O. A.; Heyden, A.; Bond, J. Q. *ACS Catal.* **2014,** *4* (4), 1171-1181.

59. Abdelrahman, O. A.; Luo, H. Y.; Heyden, A.; Roman-Leshkov, Y.; Bond, J. Q. *J. Catal.* **2015,** *329*, 10-21.

60. Guisnet, M.; Magnoux, P. *Appl. Catal. A* **2001,** *212* (1-2), 83-96.

61. Pham, H. N.; Sattler, J.; Weckhuysen, B. M.; Datye, A. K. *ACS Catal.* **2016,** *6* (4), 2257-2264.

62. Trimm, D. L. *Catal. Today* **1999,** *49* (1-3), 3-10.

63. Lopez-Ruiz, J. A.; Davis, R. J. *Green Chem.* **2014,** *16* (2), 683-694.

64. Bartholomew, C. H. *Appl. Catal. A* **2001,** *212* (1-2), 17-60.

4.8 Supporting Information

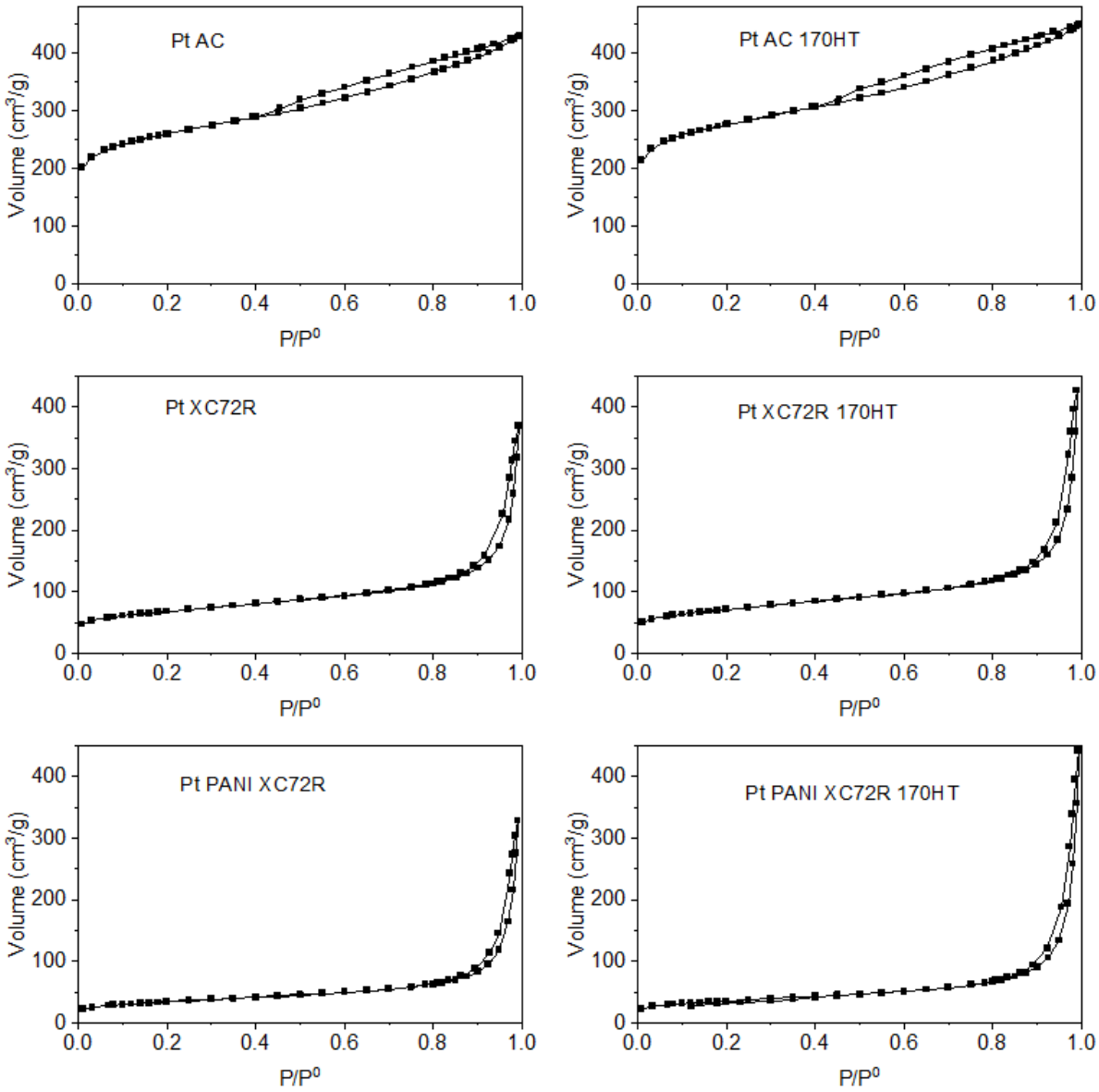

Figure S4.1. Nitrogen physisorption isotherms of Pt AC, Pt XC72R, and Pt PANI XC72R before and after hydrothermal treatment. Hydrothermal treatment was performed in water at 170 °C for 48 h.

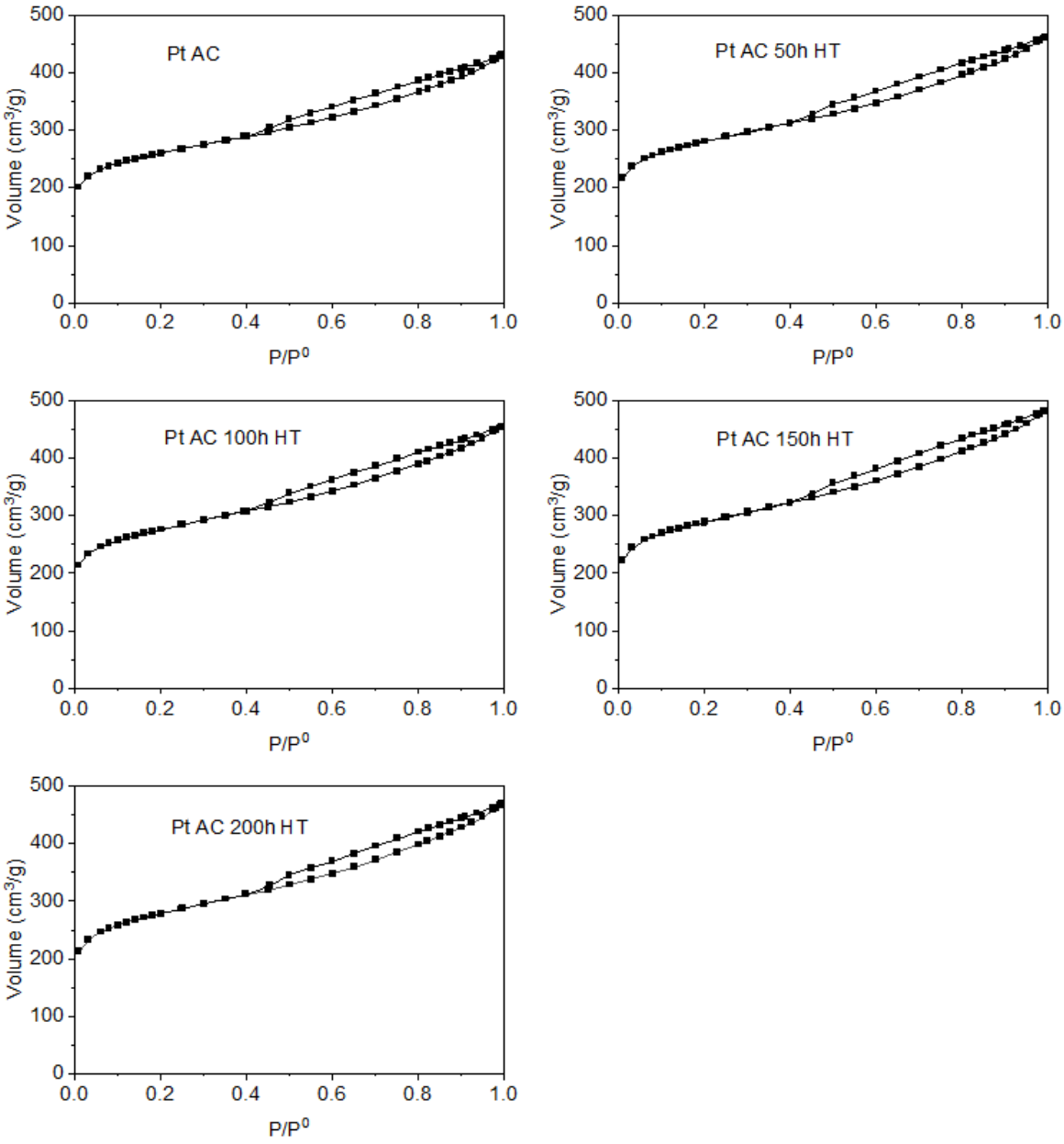

Figure S4.2. Nitrogen physisorption isotherms of Pt AC after 50h, 100h, 150h, and 200h of hydrothermal treatment at 200 °C.

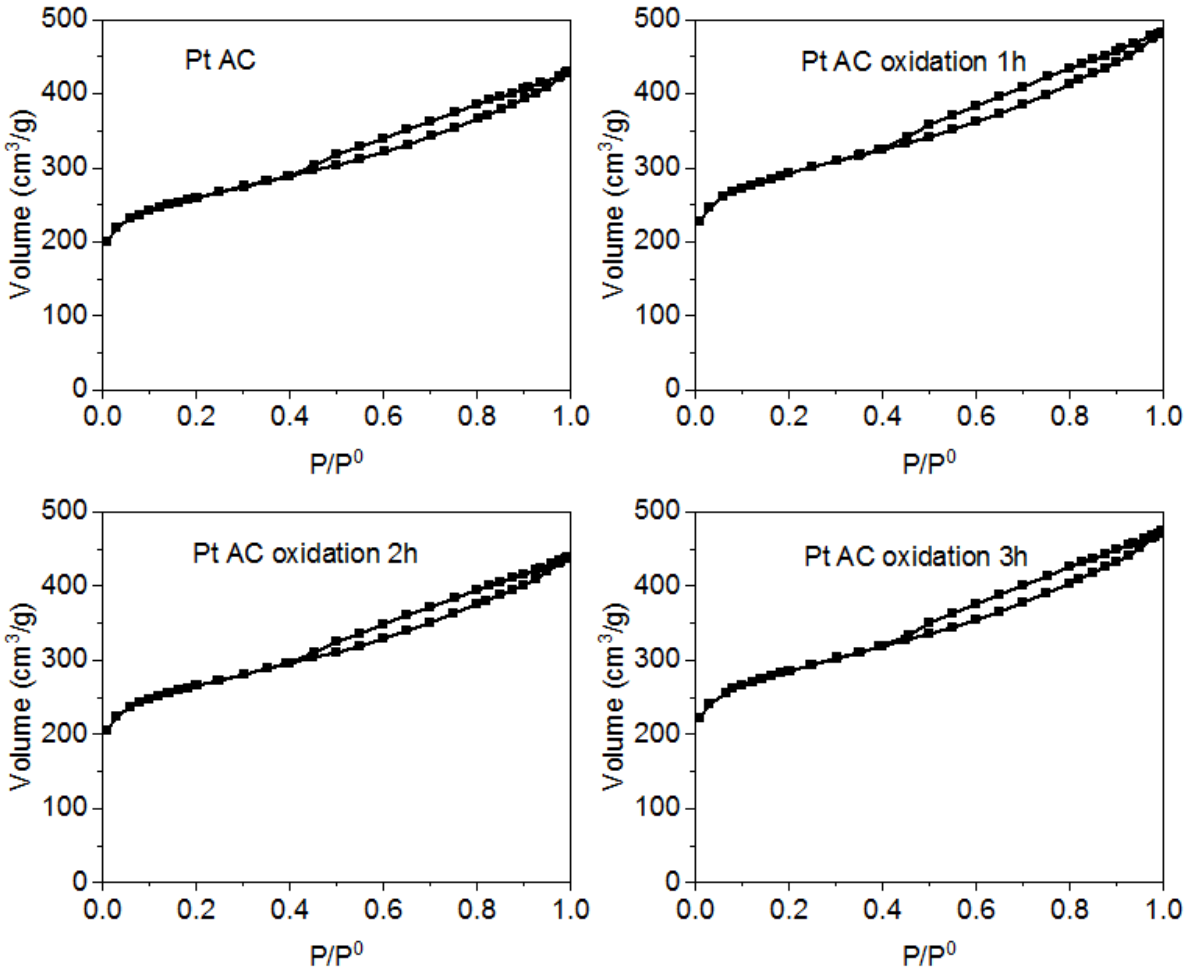

Figure S4.3. Nitrogen physisorption isotherms of Pt AC after 1h, 2h, and 3h of air oxidation at 200 °C.

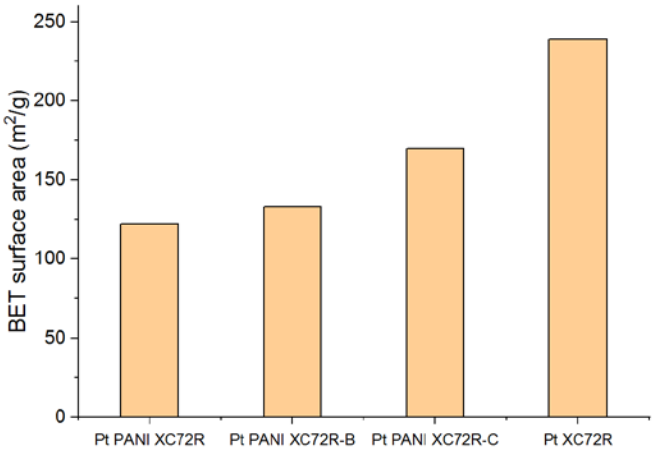

Figure S4.4. BET surface area of Pt PANI XC72R materials with different PANI coating amount. The XC72R and PANI coating weight ratio is 1% PANI XC72R (XC72R:PANI=4:1), 1% PANI XC72R-B (XC72R:PANI=8:1), 1% PANI XC72R-C (XC72R:PANI=16:1).

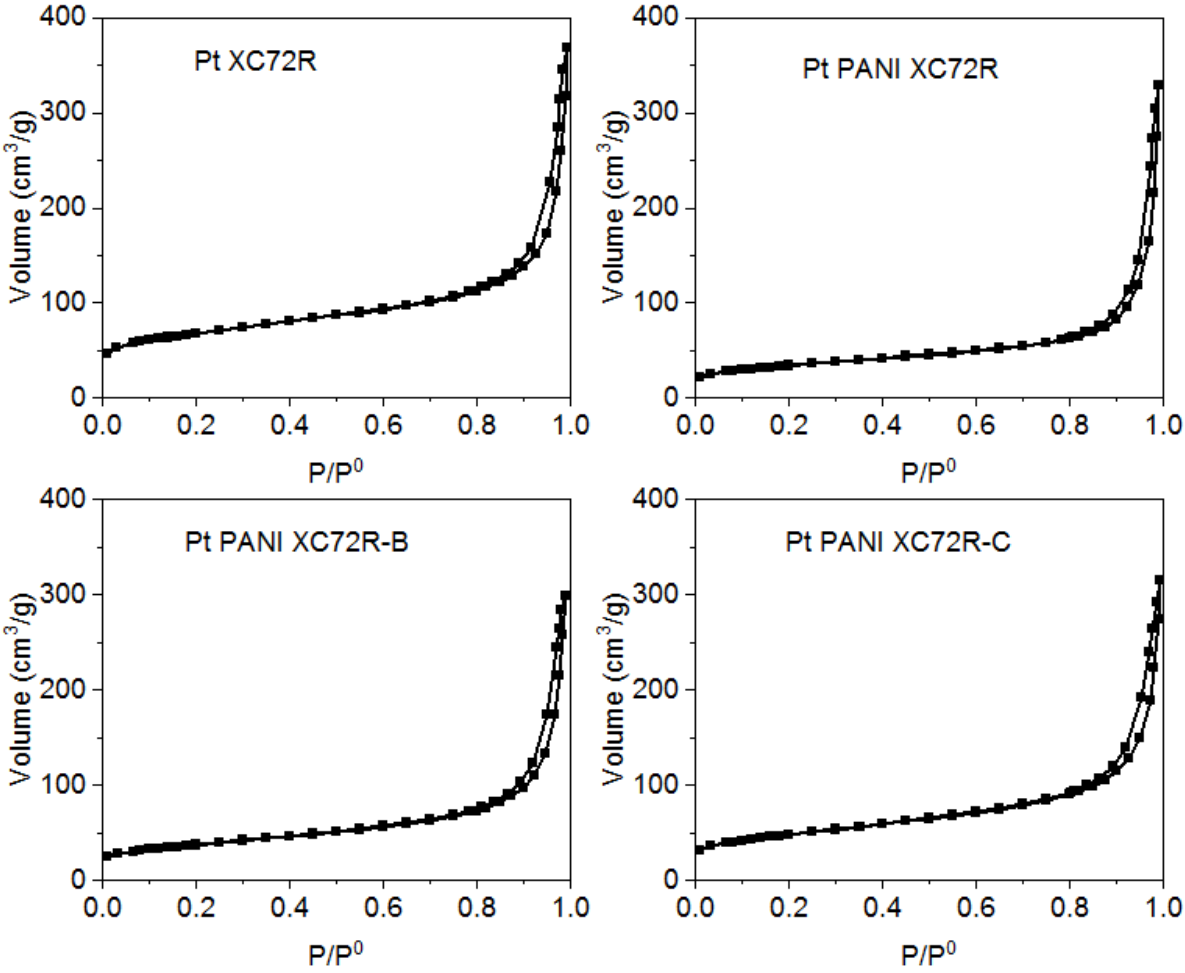

Figure S4.5. Nitrogen physisorption isotherms of Pt XC72R and Pt PANI XC72R with different PANI loading. Pt PANI XC72R (PANI:XC72R=1:4); Pt PANI XC72R-B (PANI:XC72R=1:8); Pt PANI XC72R-C (PANI:XC72R=1:16).

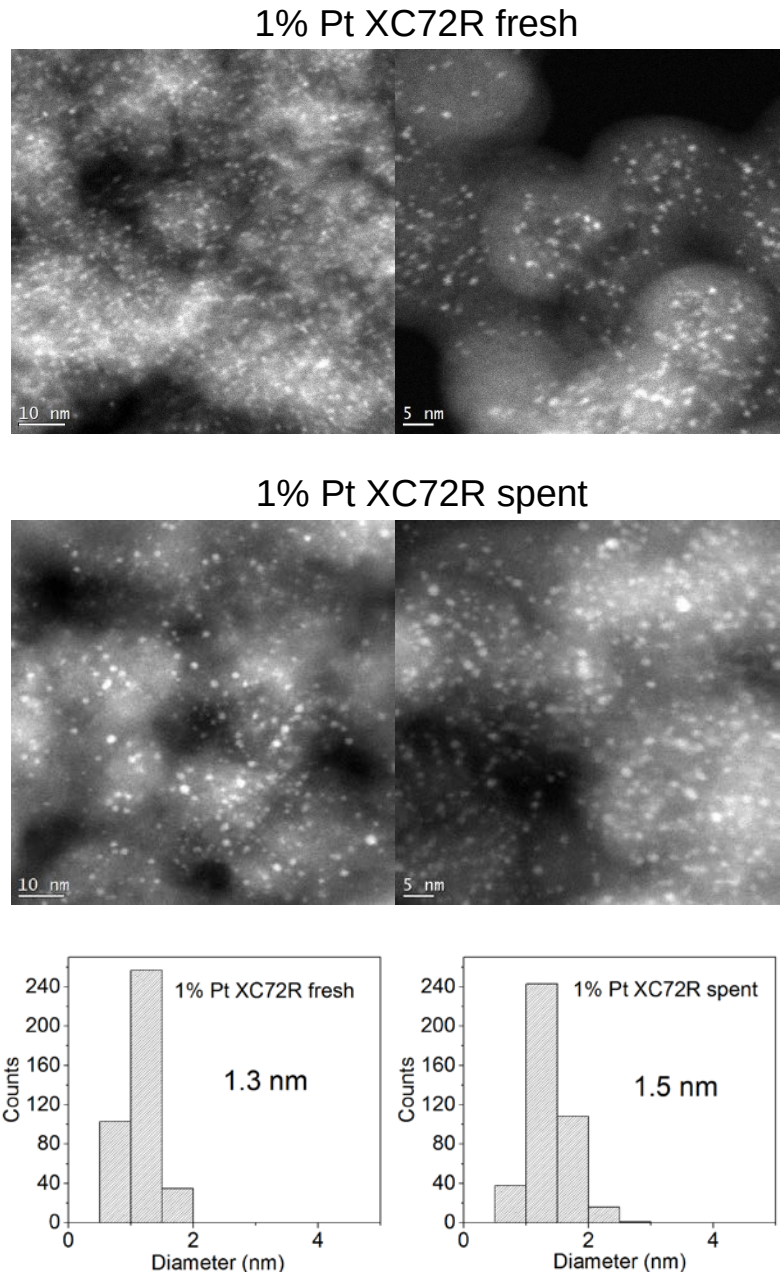

Figure S4.6. HAADF-STEM images and particle size distribution of fresh and spent 1% Pt XC72R after 450 hr of aqueous phase hydrogenation of 2-pentanone described in Figure 4.4. The surface averaged particle size is 1.3 nm for fresh catalyst and 1.5 nm for spent catalyst.

CHAPTER 5. CONCLUSIONS

As environmental and sustainability concerns continue to grow for the fossil carbons, the search for renewable energy, fuels, and chemicals is necessary and urgent. Biomass conversion offers a way to produce renewable fuels and chemicals. However, there are several challenges for the biomass conversion including selective removal of oxygen, hydrothermal stability of catalyst, stability against biogenic impurities, and fundamental understanding of the interaction between reactant in the liquid and solid catalyst. In this research, we focus on improving the hydrothermal stability of supported Pd catalysts.

As carbon materials has shown better hydrothermal stability than other catalyst support, carbon coated SBA-15 material was synthesized as catalyst support at different temperatures. Through detailed XPS and ^{13}C NMR study, the carbon surface chemistry was investigated and compared. The low temperature-pyrolyzed carbon material have more oxygen-functional groups, while the high temperature-pyrolyzed carbon was more graphitic and condensed. The stability of the Pd particles and carbon support was also investigated through hydrothermal treatment and batch aqueous-phase hydrogenation of furfural. It was found that Pd particles were more dispersed and stable on low-temperature pyrolyzed carbon material.

To further improve the stability of Pd particles, nitrogen-doped carbon coated SBA-15 material was synthesized. Through hydrothermal treatment and continuous flow aqueous-phase hydrogenation reactions, a better stability was observed on nitrogen-doped carbon supported Pd catalyst compared with only carbon coated SBA-15 supported Pd catalysts. Besides, low-temperature synthesized nitrogen-doped carbon material better supressed Pd particle sintering under hydrothermal conditions. ^{13}C and ^{15}N NMR revealed the carbon surface chemistry of the

carbon materials synthesized at different temperatures. Optimum nitrogen doping amount was also investigated and tested in continuous flow reactions.

Besides improving the catalyst stability by modifying carbon surface chemistry, a new embedded Pt PANI XC72R catalyst was made with a stable activity over the long hour continuous flow reaction. What's more, a simple regeneration method composed of low temperature oxidation and H_2 reduction was able to recover the catalytic activity. This regeneration method removed the carbon deposits on the metal surface as well as redispersed metal particles. This will help to study the regeneration of supported metal catalysts for biomass conversion related reactions under hydrothermal conditions.

As demonstrated, the carbon surface chemistry are crucial to increase the carbon-metal interaction, thus improving the stability of the catalyst. The strategy of incorporating heteroatoms can be applied to both metal oxides and carbon materials. A stable catalyst from PANI coating and a mild regeneration method was demonstrated as well. This work may give some insights on designing and synthesizing hydrothermally-stable supported metal catalysts for aqueous-phase biomass conversions.

CHAPTER 6. FUTURE DIRECTIONS

While biomass conversion is gaining more and more attention these days, research on hydrothermally-stable catalysts are still in the beginning stage. More research and fundamental understanding are needed to better preserve the catalyst under hydrothermal conditions. While hydrothermally-stable catalyst supports are being explored, how to preserve and improve the stability of the active sites including either metal sites or acid (base) sites remains nontrivial. The design and synthesis of catalyst needs to take account of the whole stability of catalyst including catalyst support and active sites instead of focusing only on catalyst support as demonstrated in the second chapter the high-temperature carbon support was more stable, but have less oxygen-functional groups, thus resulting in lower stability of supported Pd particles.

There need to be more future studies on the deactivation mechanisms. For example, as sintering is the major deactivation mechanism under hydrothermal conditions, how does this process occur? Whether it is by Ostwald ripening or particle migration and agglomeration? Likewise, leaching and carbon deposition mechanism also needs to be explored. As shown in chapter 4, the carbon deposits under hydrothermal conditions may be different from the coke generated during gas phase reactions with different oxygen content and graphitic content. Besides, as carbon materials are hydrothermally stable, understand deactivation on carbon supported metal catalysts is especially important. There are specific challenges for carbon supported metal catalysts. For example, Raman spectroscopy and TGA has been used for coke study on metal oxide catalysts. However, these techniques may not be useful for carbon materials as the signal of carbon deposits may be blurred by the carbon catalyst material. Understanding the fundamental deactivation mechanisms can help to direct future catalyst synthesis. This understanding may need in-situ characterization under hydrothermal conditions, which is non-

trivial as the water may generate signal and interact with the reactant and catalyst. Besides, the influence of temperature, pH of aqueous phase, reactant concentration, and many other factors commonly encountered in biomass conversions need to be considered.

The synthesis of new hydrothermally-stable catalyst materials is another focus for the research. In this dissertation, we have shown that carbon surface chemistry such as oxygen and nitrogen heteroatoms can help to anchor the metal particles thus stabilizing metal particles. Further embedding metal particles help to make a stable carbon supported metal catalysts. These techniques can be further applied to other materials. Other novel catalyst materials should be emphasized as well.